Magnetic Properties of $Mn_{2-x}Fe_xSb_{1-y}Sn_y$ ($0.05 \leq x \leq 0.15$, $0.05 \leq y \leq 0.1$)

by

Adline Ngozi Nwodo

Department of Materials Science and Production Engineering,

Graduate School of Science and Engineering,

Kagoshima University

March 2018

The doctoral thesis of Adline Ngozi Nwodo is approved, and it is acceptable in quality and form for publication:

Promoter: Prof. Keiichi Koyama _____

Co- promoters: Prof. Masahiko Hiroi _____

Associate Prof. Yoshifuru Mitsui _____

Graduate School of Science and Engineering

Kagoshima University

March, 2018

DECLARATTION

This doctoral thesis is submitted by the undersigned for examination for the degree of Doctor of Engineering at the Kagoshima University. It has not been submitted to an exercise for a degree at any other University.

This doctoral thesis, apart from the device, assistance and joint effort mention in the acknowledgment and in the text, is entirely my own work.

I agree that the Library may lend or copy this thesis freely on request.

Adline Ngozi Nwodo

March, 2018

ABSTRACT

The magnetic and the structural properties of $Mn_{2-x}Fe_xSb_{1-y}Sn_y$ ($0.05 \leq x \leq 0.15$, $0.05 \leq y \leq 0.1$) with tetragonal structure were studied by magnetization, differential scanning calorimetry and high field X-ray measurements in $10 \leq T \leq 360$ K and in magnetic fields $\mu_0 H$ up to 5 T, in order to clarify the magnetic and structural properties and to estimate the potential for application.

X-ray diffraction study of $Mn_{2-x}Fe_xSb_{1-y}Sn_y$ ($0.05 \leq x \leq 0.15$, $0.05 \leq y \leq 0.1$) indicates a Cu_2Sb-type tetragonal structure (space group P4/nmm). The lattice parameters a and c of $Mn_{1.9}Fe_{0.1}Sb_{0.9}Sn_{0.1}$ were estimated to be 0.4068 nm and 0.6549 nm, respectively, at 285 K. The temperature dependence of a and c of $Mn_{1.9}Fe_{0.1}Sb_{0.9}Sn_{0.1}$ showed a normal thermal contraction without discontinuous changes due to a structural transformation. The thermal expansion coefficients of a and c of $Mn_{1.9}Fe_{0.1}Sb_{0.9}Sn_{0.1}$ were estimated to be 1.3×10^{-5} K^{-1} and 1.3×10^{-5} K^{-1} in $275 \leq T \leq 325$ K, respectively.

The substitution of Fe for Mn in $Mn_2Sb_{0.9}Sn_{0.1}$ resulted in suppression of the AFM state. The saturation magnetization of $Mn_{1.9}Fe_{0.1}Sb_{0.9}Sn_{0.1}$ at 10 K was determined to be 39.1 Am^2/kg (39.1 emu/g), which was slightly smaller than the value (39.2 Am^2/kg) at 70 K for $Mn_{1.9}Fe_{0.1}Sb_{0.9}Sn_{0.1}$. $Mn_{2-x}Fe_xSb_{1-y}Sn_y$ ($0.05 \leq x \leq 0.15$, $0.05 \leq y \leq 0.1$) did not show a magnetic transition from ferrimagnetic (FRI) to antiferromagnetic (AFM) at low temperature but the first-order magnetic transition (FOMT) from FRI to paramagnetic (PM)-like state with a thermal hysteresis in the vicinity of 310-380 K respectively.

With increasing Fe contents in $Mn_{2-x}Fe_xSb_{1-y}Sn_y$ ($0.05 \leq x \leq 0.15$, $0.05 \leq y \leq 0.1$), the magnetic moment of 10 K decreases but the FOMT temperature increase. Obtained results indicate that the substitution of Fe for Mn in $Mn_2Sb_{1-y}Sn_y$ suppresses the AFM interaction and induces the FRI interaction. The results are discussed on the basis of the AFM-FR transitions and spin reorientation.

ACKNOWLEDGMENTS

I would like to express my sincere gratitude to all the people who became involved with this research. I am especially thankful to my supervisor, Prof. Keiichi Koyama for his support, his active interest and constant guidance throughout the course of this work. I admire his dedication to Science and profound knowledge in Physics. It has been a great honour for me to have worked under his supervision.

I am grateful to Associate Prof. Yoshifuru Mitsui and Prof. Masahiko Hiroi for the exciting and productive time I spent at Kagoshima University (Magnetophysics Laboratory), and also at Materials Research Institute (IMR), Tohoku University and the Institute for Solid State Physics (ISSP), the University of Tokyo. I am thankful to Prof. Yoshiya Uwatoko and Dr. Kohki Takahashi of the Institute for Solid State Physics (ISSP), the University of Tokyo and Materials Research Institute (IMR), Tohoku University respectively.

This research was made possible due to the able assistance of Prof. Keiichi Koyama, Associate Prof. Yoshifuru Mitsui in the lab, and my colleague, Mr. Y. Matsumoto, Mr. K. Ozono, Mr. Ryouta Kobayashi, Mr.

Taoto Wakamori, who collaborated with me in the sample preparation and direct measurement experiments at the Kagoshima University (Magnetophysics Laboratory). I would like to thank the people working at Tohoku University and the University of Tokyo for their supports.

I would also like to thank my committee members for their many constructive discussions. Finally, I am grateful to all the graduate students in the Kagoshima University Laboratory group for their help in the experiments and discussions.

Finally, I owe most of my thanks to my parents, siblings and Prof. Johnson O. Urama of the University of Nigeria, Nsukka, who have constantly encouraged me in my work.

CONTENTS

Chapter 5 Conclusion and Suggestion for Future Work

Chapter 1

Introduction

1.1 A Brief History of Magnetism and Permanent Magnetic Materials

The history of permanent magnets goes back to ancient times. Records from early Greek, Roman and Chinese civilisations make reference to rare and mysterious stones called lodestones. These lodestones could attract each other and also small pieces of iron. In 1088 Shen Kuo described the magnetic needle compass, which could be used for navigation in his Dream Pool Essays [Enz, 1982]. The first recorded use was documented by Zheng He of the Yunnan province. Between the years 1405 and 1433, Zheng He recorded his voyages across seven oceans. A series of major contributions was made to different aspects of magnetism since the early nineteenth century by H.C Orstead, A.M Ampere, M. Faraday, W. Weber, P.Curier, P. Langevin, P. Weiss, W. Heisenberg, E.C. Stoner and L. N*é*el etc. Modern magnetism is based on these contribution [Enz, 1982]. Modern research into

magnetism is heading in many different directions involving a vast array of materials, however at this time there are only four types of permanent magnets that are commonly used throughout the world. They are Alnico, Ferrite, Samarium Cobalt and the most recently invented, Neodymium or "Rare Earth magnets". Today magnets play a role almost every technologically advanced device we use, including computers, automobiles, industrial sorter and seperators, power generators, speakers, cell phones etc. Permanent magnets are essential to modern life as components of wide variety of electromechanical and electronic devices [Enz, 1982].

The growth of applications for permanent magnets results in large part from the improvements in magnetic properties, which allow the engineer to design smaller, lighter and more efficient devices. The properties of most significant interest are remanence, coercivity and maximum energy product [Livingstone, 1990]. Figure 1.1.1 (a) shows the history of $(BH)_m$ values achieved since 1880. Here, H is the magnetic field, and B is the magnetic flux density. The points labeled 1-3 are steels, 4-8 are alnicos and 9-12 are rare-earth magnets. From 1 to 9, increases resulted primarily from increases in coercivity. Since then, increases have resulted from increases in

remanence, while maintaining coercivity. Figure 1.1.1 (b) shows schematic representation of resulting change in magnet size required for a specific application. The numbers correspond to the numbers in (a) [Livingstone, 1990; Buschow, 1988].

In 1966 the first rare earth magnets were developed from Samarium-Cobalt ($SmCo_5$) producing a high energy product of 18 MGOe. In 1972 further developments were made using Samarium-Cobalt (Sm_2Co_{17}) to produce a higher energy magnet product of 30 MGOe. Moreover, this was the basis for the use of rare earth transition intermetallic compounds as potential high energy products. The hexagonal RCo_5 (R = rare earth) compound have $CaCu_5$ –type structure. They have extremely large magnetocrystalline anisotropy which originate from the contribution of the R atoms [Strnat et al., 1966]. Samarium Cobalt magnets have several features that made them far superior to any magnet available during the time. They have a magnetic strength that is several times greater than either Alnico or Ferrite magnets, while at the same time they offer a very high temperature stability. Temperatures of 300^0C can be easily withstood by Samarium Cobalt magnets and in addition to this they also demonstrate excellent

corrosion resistance. However, samarium cobalt does have its disadvantages two of which are that they are very brittle and therefore extremely fragile and they are a very expensive magnet to produce.

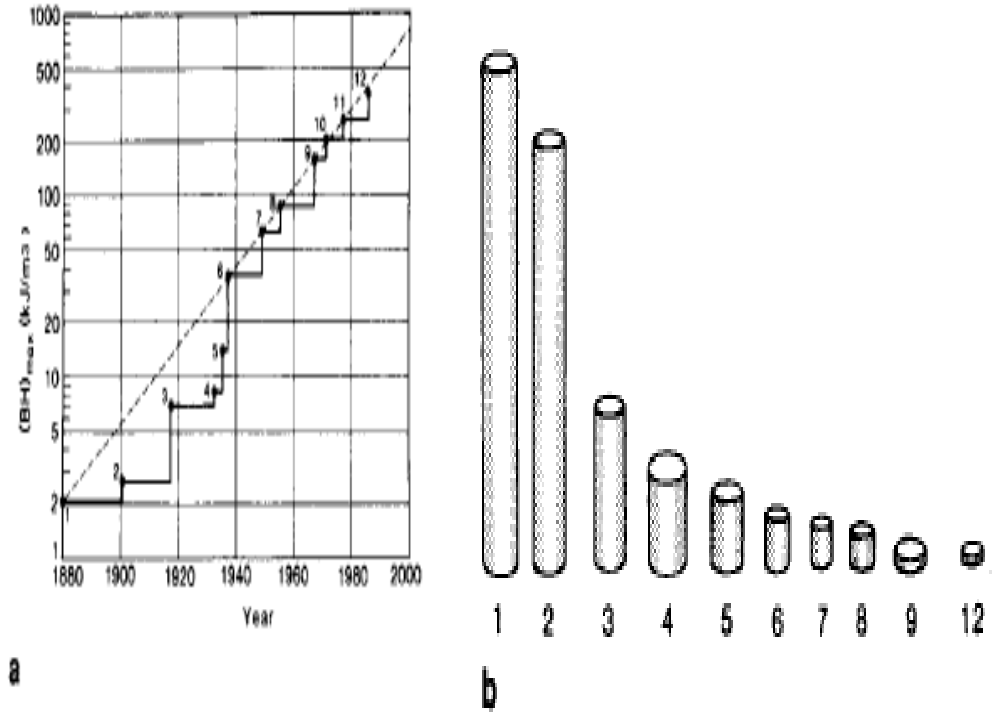

Figure 1.1.1 (a) History of $(BH)_m$ values achieved since 1880. The points labeled 1-3 are steels, 4-8 are alnicos and 9-12 are rare-earth magnets. (b) Schematic representation of resulting change in magnet size required for a specific application. The numbers correspond to the numbers in (a) [Livingstone, 1990; Buschow, 1988].

A novel type of permanent magnetic material was announced in 1984. It was on a ternary intermetallic compound obtained by combining Nd, Fe and B. It has a tetragonal structure (Space group $P4_2/mnm$) with the composition formula corresponding to $Nd_2Fe_{14}B$ [Sagawa et al 1984]. Rare earth magnets offer high magnetic energy and good stability and very cost effective. Neodymium Iron Boron Magnets, or "Rare Earth" magnets are the strongest type of permanent magnet available on today's market. Unfortunately, Rare Earth magnets do have two disadvantages. They have poor corrosion resistance and they are more temperature sensitive than other magnets. Today magnets play a role almost every electronics and engineering projects [Sagawa et al 1984, Croat et al. 1984].

Researchers are searching for other ternary and higher order compound, whether with a completely new structure like $Nd_2Fe_{14}B$, or with sufficiently high values of magnetization, anisotropy and Curie temperature to be useful as permanent magnets. These dictate that its main component be alloy systems containing iron, cobalt and rare earths, often with one or more additional elements. The magnetocrystalline anisotropy, which is necessary

for sufficiently high magnetic hardness, can be obtained by including a component consisting of rare earth elements. Its content has to be low, both for price consideration and corrosion resistance. Current understanding suggests the possibility of somebody achieving energy products up to 800 KJ/m^3, but much higher values appear very unlikely [Livingston, 1987].

One very successful approach has been the search for ternary phases, whether with a completely new structure like $Nd_2Fe_{14}B$, or with structure derived from an existing binary structure type by preferential substitution like $Sm(Fe_{11}Ti)$ and $Sm(Fe_{10}V_2)$ ($ThMn_{12}$-type structure). The production of a higher energy product via higher magnetization, finding high-coercivity materials with higher Currier temperature or lower cost than Nd-Fe-B would also be of great importance. A coercivity material with energy products substantially lower than rare earth magnets would be particularly helpfully in expanding permanent magnet applications.

Past progress in permanent magnet materials has been to seek metastable phases like $SmFe_7$ ($TbCu_7$-type structure) by melt spinning or mechanical alloying, or to make interstitial compounds like $R_2Fe_{17}C_x$ from melt which are related to known binaries [Katter et al., 1991 and Zhong et

al., 1990]. However, none of these materials has quite succeeded in matching the intrinsic magnetic properties of $Nd_2Fe_{14}B$. Despite the technological and scientific importance of magnetic materials, few university, industrial or government laboratory have major programs in the area. Although progress will undoubtedly continue, it would be more rapid if more materials scientists focused their attention on this scientifically interesting and technologically important field.

1.2 Ferromagnetism

The term ferromagnetism is used to characterize strongly magnetic behaviour, such as strong attraction of a material to a permanent magnet. The origin of this strong magnetism is the presence of a spontaneous magnetization produced by a parallel alignment of spins. Instead of a parallel alignment of spins, there can be an anti-parallel alignment of unequal spins. This results in a spontaneous magnetization, which we call ferrimagnetism [Chikazumi, 2009]. Ferromagnetism has spontaneous magnetic moments even in zero applied magnetic field. The existence of a spontaneous moment suggests that electron spins and magnetic moments are arranged in a regular

manner as shown in Fig. 1.2.1 [Kittle, 1996]. Ferromagnetism (including ferrimagnetism) is the strongest type: it is the only one that typically creates forces strong enough to be felt, and is responsible for the common phenomena of magnetism in magnets encountered in everyday life [Chikazumi, 2009]. Substances respond weakly to magnetic fields with three other types of magnetism, paramagnetism, diamagnetism, and antiferromagnetism, but the forces are usually so weak that they can only be detected by sensitive instruments in a laboratory. These will be discussed in the subsequent sections. An everyday example of ferromagnetism is a refrigerator magnet used to hold notes on a refrigerator door. The attraction between a magnet and ferromagnetic material is "the quality of magnetism first apparent to the ancient world, and to us today" [Bozorth and Richard, 1951].

Examples of ferromagnetism includes; iron, nickel, cobalt and most of their alloys, and a few naturally occurring minerals, including some varieties of lodestone (magnetite is considered ferrimagnetic, rather than ferromagnetic), Heusler alloys, stainless steel, composed almost exclusively of ferromagnetic metals. Ferromagnetism is a relatively rare property among

the elements occurring only in the transition metals Fe, Ni, and Co, and in the lanthanides (REEs) [Jackson and Mike, 2000].

Ferromagnetism is very important in industry and modern technology, and is the basis for many electrical and electromechanical devices such as electromagnets, electric motors, generators, transformers, and magnetic storage such as tape recorders, and hard disks, and nondestructive testing of ferrous materials.

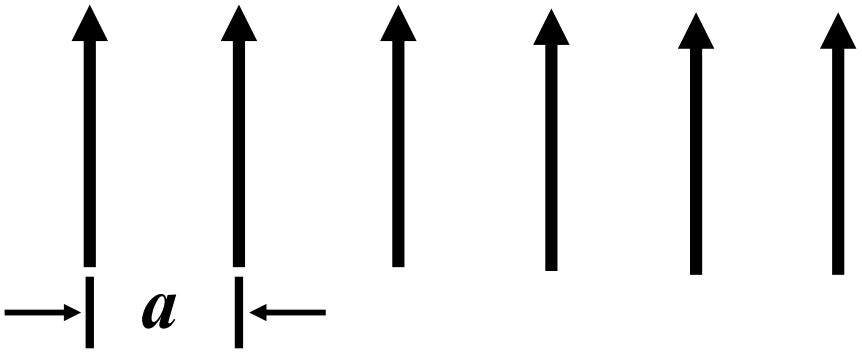

Fig 1.2.1 Classical picture of the ground state of a simple ferromagnet, all spins are parallel [Kittle, 1996].

1.3 Ferrimagnetism

In ferrimagnets, the A- and B-sublattice are occupied by different magnetic atoms and sometimes by different numbers of atoms, so that the antiferromagnetic spin arrangement results in an uncompensated spontaneous magnetization as shown in Fig. 1.3.1. Such magnetism is called ferrimagnetism and was first treated by Néel [Néel, 1948]. This happens when the populations consist of different materials or ions (such as Fe^{2+} and Fe^{3+}).

For simplicity, let us assume that only one kind of magnetic atom, with magnetic moment *M*, contributes to ferrimagnetism. The total number, 2 N, of magnetic atoms is distributed on the A- and B-sites in the ratio λ : μ, where

$$\lambda + \mu = 1 \qquad 1.3.1$$

If all the magnetic moments are completely ordered, the sublattice magnetization are given by

$$\left.\begin{aligned} I_A &= 2N\lambda M \\ I_B &= 2N\mu M \end{aligned}\right\}, \qquad 1.3.2$$

So that the spontaneous magnetization is

$$I = I_A + I_B = 2NM(\lambda - \mu). \qquad 1.3.3$$

At any temperature above absolute zero, the sublattice magnetization are thermally disturbed; and even at 0 K, sometimes complete order may not be realized [Chikazumi, 1997].

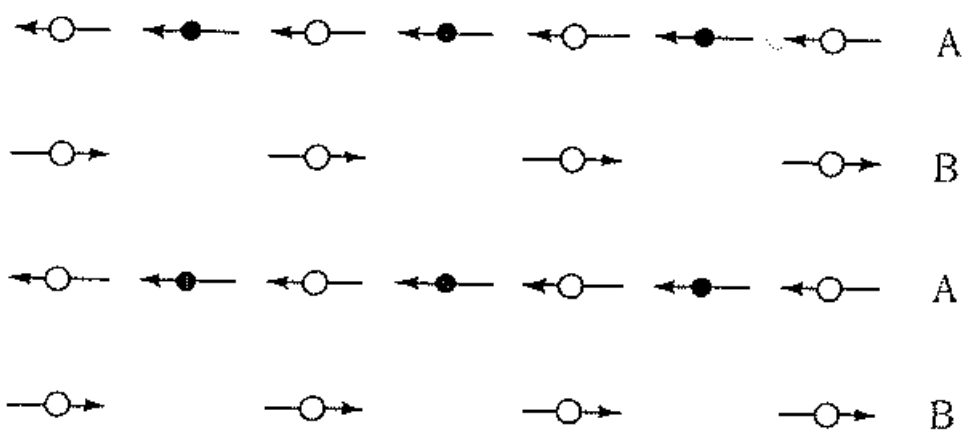

Fig 1.3.1. Spin structure of ferrimagnet. [Chikazumi, 1997].

Ferrimagnetism is exhibited by ferrites and magnetic garnets. The oldest known magnetic substance, magnetite (iron (II, III) oxide; Fe_3O_4), is a ferrimagnet; it was originally classified as a ferromagnet before Néel's discovery of ferrimagnetism and antiferromagnetism in 1948 [Néel, 1948].

Known ferrimagnetic materials include YIG (yttrium iron garnet), cubic ferrites composed of iron oxides and other elements such as aluminum, cobalt, nickel, manganese and zinc, hexagonal ferrites such as $PbFe_{12}O_{19}$ and $BaFe_{12}O_{19}$, and pyrrhotite, $Fe_{1-x}S$ [Klein, 2007]. Some ferrimagnetic materials are like ferromagnets in that they hold a spontaneous magnetization below the Curie temperature, and show no magnetic order (are paramagnetic) above this temperature. However, there is sometimes a temperature below the Curie temperature at which the two opposing moments are equal, resulting in a net magnetic moment of zero; this is called the magnetization compensation point. [Stanciu, 2006]. Some ferrimagnetic materials have high resistivity and have anisotropic properties [Sessoli, 1993]. The anisotropy is actually induced by an external applied field. When this applied field aligns with the magnetic dipoles it causes a net magnetic dipole moment and causes the magnetic dipoles to precess at a frequency controlled by the applied field, called Larmor or precession frequency. Ferrimagnetism can also occur in molecular magnets [Sessoli, 1993].

1.4 Paramagnetism

Paramagnetism describes a feeble magnetism which exhibits a positive suscepitibility of the order $\chi = 10^{-5} - 10^{-2}$. This magnetic behavour is found in materials that contain magnetic atoms or ions that are widely separated so that they exhibit no appreciable interaction with one another [Soshin 1997]. In paramagnetism, certain materials are weakly attracted by an externally applied magnetic field, and form internal, induced magnetic fields in the direction of the applied magnetic field. In contrast with this behavior, diamagnetic materials are repelled by magnetic fields and form induced magnetic fields in the direction opposite to that of the applied magnetic field [Miessler, 2010]. Paramagnetic materials include most chemical elements and some compounds. Paramagnetic materials include oxygen and ions of various metals like Fe (iron), Mg (magnesium), and Gd (gadolinium). These ions have unpaired electrons, resulting in a positive magnetic susceptibility and it is just the permeability minus 1 [Nave, 2008]. The magnitude of this susceptibility is less than one one-thousandths of that of ferromagnetic materials [Horowitz, 1989].

The magnetic moment induced by the applied field is linear in the field strength and rather weak. Most elements, and some compounds, are paramagnetic i.e., their constituent atoms, or molecules, possess a permanent magnetic moment due to the presence of one or more unpaired electrons. Strong paramagnetism (not to be confused with the ferromagnetism of the elements iron, cobalt, nickel, and other alloys) is exhibited by compounds containing iron, palladium, platinum, and the rare-earth elements. In such compounds atoms of these elements have some inner electron shells that are incomplete, causing their unpaired electrons to spin like tops and orbit like satellites, thus making the atoms a permanent magnet tending to align with and hence strengthen an applied magnetic field [Jensen, 1991]. Strong paramagnetism decreases with rising temperature because of the de-alignment produced by the greater random motion of the atomic magnets.

Weak paramagnetism, independent of temperature, is found in many metallic elements in the solid state, such as sodium and the other alkali metals, because an applied magnetic field affects the spin of some of the loosely bound conduction electrons [Jensen, 1991].

Unlike ferromagnets, paramagnets do not retain any magnetization in the absence of an externally applied magnetic field because thermal motion randomizes the spin orientations. (Some paramagnetic materials retain spin disorder even at absolute zero, meaning they are paramagnetic in the ground state, i.e. in the absence of thermal motion.) Thus, the total magnetization drops to zero when the applied field is removed. Even in the presence of the field there is only a small induced magnetization because only a small fraction of the spins will be oriented by the field. Materials that are called "paramagnets" are most often those that exhibit, at least over an appreciable temperature range, magnetic susceptibilities that adhere to the Curie or Curie–Weiss laws. In addition, the lanthanide elements with incompletely filled 4f-orbitals are paramagnetic or magnetically ordered [Jensen, 1991].

1.5 Curie's law and Curie-Weiss law

In a paramagnetic material the magnetization of the material is (approximately) directly proportional to an applied magnetic field. However, if the material is heated, this proportionality is reduced: for a fixed value of

the field, the magnetization is (approximately) inversely proportional to temperature. This fact is encapsulated by Curie's law. This law indicates that the susceptibility, χ, of paramagnetic materials is inversely proportional to their temperature, i.e. that materials become more magnetic at lower temperatures. The mathematical expression is:

$$M = \chi H = \frac{C}{T} H, \qquad 1.5.1$$

where, M is the resulting magnetization, χ is the magnetic susceptibility, H is the auxiliary magnetic field, measured in amperes/meter, T is absolute temperature, measured in kelvins, and C is a material-specific Curie constant.

Curie's law only holds for high temperatures, or weak magnetic fields. When the dipoles are aligned, increasing the external field will not increase the total magnetization since there can be no further alignment.

For a paramagnetic ion with noninteracting magnetic moments with angular momentum J, the Curie constant is related the individual ions' magnetic moments,

$$\mathrm{C} = \frac{N_A}{3K_B} \mu_{eff}^2, \qquad 1.5.2$$

where $\mu_{eff} = gJ\mu_B\sqrt{J(J+1)}$.

Where J is the total angular momentum quantum number, g is the spin's g-factor (such that $\mu = gJ\mu_B$ is the magnetic moment), and μ_{eff} is the effective magnetic moment per paramagnetic ion. If one uses a classical treatment with molecular magnetic moments represented as discrete magnetic dipoles, μ, a Curie Law expression of the same form will emerge with μ appearing in place of μ_{eff} [Nave, 2008].

When orbital angular momentum contributions to the magnetic moment are small, as occurs for most organic radicals or for octahedral transition metal complexes with d^3 or high-spin d^5 configurations, the effective magnetic moment takes the form ($g_e = 2.0023... \approx 2$),

$$\mu_{eff} \cong 2\sqrt{S(S+1)}\mu_B = \sqrt{n(n+2)}\mu_B, \qquad 1.5.3$$

where n is the number of unpaired electrons. In other transition metal complexes this yields a useful, if somewhat cruder, estimate [Nave, 2008].

The word paramagnet now merely refers to the linear response of the system to an applied field, the temperature dependence of which requires an amended version of Curie's law, known as the Curie–Weiss law. The Curie–

Weiss law describes the magnetic susceptibility χ of a ferromagnet in the paramagnetic region above the Curie point. This relationship is expressed by:

$$M = \frac{C}{T-\theta} H, \qquad 1.5.4$$

where, T is absolute temperature, measured in kelvins, and C is a material-specific Curie constant and θ describes the exchange interaction that is present albeit overcome by thermal motion. The sign of θ depends on whether ferro- or antiferromagnetic interactions dominate and it is seldom exactly zero, except in the dilute, isolated cases.

1.6 Diamagnetism

The period of 10 years following Michael Faraday's discovery of diamagnetism in the late 1845 was critical one for development of the understanding of magnetism and for Faraday's emerging field theory. The phenomena of diamagnetism is complex and very weak compared to paramagnetism or ferromagnetism requiring powerful magnets and sensitive, and expensive, apparatus [Jackson, 2015]. Diamagnetism means a feeble

magnetism, which occurs in a material containing no atomic magnetic moments. The susceptibilty of such material is negative and small, typically $\overline{\chi} = 10^{-5}$. [Van, 1932; Chikazumi, 1997].

Diamagnetic materials are repelled by a magnetic field, an applied magnetic field creates an induced magnetic field in them in the opposite direction, causing a repulsive force. Pyrolytic carbon has one of the largest diamagnetic constants of any room temperature material. In contrast, paramagnetic and ferromagnetic materials are attracted by a magnetic field. Diamagnetism is a quantum mechanical effect that occurs in all materials; when it is the only contribution to the magnetism the material is called diamagnetic. In paramagnetic and ferromagnetic substances, the weak diamagnetic force is overcome by the attractive force of magnetic dipoles in the material. The magnetic permeability of diamagnetic materials is less than μ_0, the permeability of vacuum. In most materials diamagnetism is a weak effect which can only be detected by sensitive laboratory instruments, but a superconductor acts as a strong diamagnet because it repels a magnetic field entirely from its interior. Electronic paramagmnetism (positive contribution to χ) is found in:

1. Atoms, molecules and lattice defects opposing an odd number of electrons, as here the total spin cannot be zero. Examples; free sodium atoms; gaseous nitric oxide (NO); organic free radicals such as triphenylmethyl, $C(C_6H_5)_3$; F center in alkali halides.
2. Free atoms and ions with partially filled inner shell: transition elements ions isoelectronic with transition elements; rare earth and actinide elements. Examples; Mn^{2+}, Gd^{3+}, U^{4+}, Paramagnetism is exhibited by many of these ions even when incorporated into solids, but not invariably.
3. A few compounds with an even number of electrons, including molecular oxygen and organic biradicals
4. Metals [Kittle, 1996].

Materials called diamagnetic are those that laymen generally think of as *non-magnetic*, and include water, wood, most organic compounds such as petroleum and some plastics, and many metals including copper, particularly the heavy ones with many core electrons, such as mercury, gold and bismuth. The magnetic susceptibility values of various molecular fragments are called Pascal's constants.

Diamagnetic objects are by magnetic fields. If the fields are strong enough, this repulsion can balance gravity, and object levitated in this way can be held in stable equilibrium, apparently violating Earnshaw's theorem. In fact, Earnshaw's theorem does not apply induced magnetism, and it is possible for total energy (gravitational + magnetic) to possess a minimum [Berry and Geim, 1997]. It is fascinating to see objects floating without material support or suspension. In the 1980's, this be a familiar sight when the pellets of the new high- temperature type II superconductors were levitated above permanent magnets, and vice versa (Brandt, 1980).

Researchers at the High Field Magnet Laboratory at Radboud University in Nijmegen and Tohoku University, Japan, have now shown that this effect can be used to grow a pure crystal of the protein lysozyme. One of the few scientific success stories of the International Space Station has been its use to grow large, pure crystals in microgravity [Kleiner, 2007].

Diamagnetic materials, like water, or water-based materials, have a relative magnetic permeability that is less than or equal to 1, and therefore a magnetic susceptibility less than or equal to 0, since susceptibility is defined

as $\chi_v = \mu_v - 1$. This means that diamagnetic materials are repelled by magnetic fields. The magnetic susceptibility is then zero if the material does not respond with any magnetization. So, both quantities give the same information, and both are dimensionless quantities [Nave and Carl, 2008]. The magnetization is defined as the magnetic moment per unit volume. The magnetic susceptibility is per unit volume is defined as

$$\text{(CGS)}\ \chi = \frac{\mathrm{M}}{\mathrm{B}}\ , \qquad \text{(SI)}\ \chi = \frac{\mu_0 \mathrm{M}}{\mathrm{B}}\ , \qquad 1.6.1$$

where B is the macroscopic magnetic field intensity. In both system of units χ is dimensionless.

However, since diamagnetism is such a weak property, its effects are not observable in everyday life. For example, all conductors exhibit an effective diamagnetism when they experience a changing magnetic field. The Bohr–van Leeuwen theorem proves that there cannot be any diamagnetism or paramagnetism in a purely classical system. However, the classical theory for Langevin diamagnetism gives the same prediction as the quantum theory [Kittle, 1986]. The classical theory is given below.

1.6.1 Langevin Diamagnetism Equation

Diamagnetism is associated with the tendency of electrical charges partially to shield the interior of a body before an applied magnetic field. In electromagnetism we are familiar with Lenz law: When the flux through an electrical circuit is changed, an induced current is set up in such a direction as to oppose the flux change [Kittle, 1996]. The Langevin theory of diamagnetism applies to materials containing atoms with closed shells. A field with intensity B, applied to an electron with charge e and mass m, gives rise to Larmor precession with frequency $\omega = eB / 2m$. The number of revolutions per unit time is $\omega / 2\pi$, so the current for an atom with Z electrons is (in SI units) [Kittle, 1996]

$$\mathrm{I} = (\text{charge})(\text{revelution per unit time}) = \frac{Ze^2}{4\pi m} \quad . \qquad 1.6.2$$

The magnetic moment μ of a current loop = (current) $\times$ (area of the loop). Suppose the field is aligned with the z axis. The average loop area can be given as $\pi\langle\rho\rangle^2$, where $\langle\rho\rangle^2$ is the mean square distance of the electrons perpendicular to the z axis. The magnetic moment is therefore

(SI) $\mu = \frac{Ze^2B}{4m}\langle\rho\rangle^2$ (CGS), $\mu = \frac{Ze^2B}{4mc^2}\langle\rho\rangle^2$. 1.6.3

If the distribution of charge is spherically symmetric, we can suppose that the distribution of *x,y,z* coordinates are independent and identically distributed. Then, $\langle x^2\rangle = \langle y^2\rangle = \langle z^2\rangle = \frac{1}{3}\langle r^2\rangle$ where $\langle r^2\rangle$ is the mean square distance of the electrons from the nucleus.

Therefore, $\langle\rho^2\rangle = \langle x^2\rangle + \langle y^2\rangle = \frac{2}{3}\langle r^2\rangle$.

From eq.1.6.3 the diamagnetic susceptibility per unit volume is, if N is the number of atoms per unit volume,

(CGS) $\chi = \frac{\mu_0 N\mu}{B} = \frac{\mu_0 NZe^2}{6m}\langle r^2\rangle$, 1.6.4

(SI) $\chi = \frac{\mu_0 N\mu}{B} = \frac{\mu_0 NZe^2}{6m}\langle r^2\rangle$. 1.6.5

This is the classical Langevian result.

The problem of calculating the diamagnetic susceptibility of an isolated atom is reduced to the calculation of $\langle r^2\rangle$ for electron distribution within the atom. The distribution can be calculated by quantum mechanics [Kittle, 1996].

This relationship holds fairly well for materials containing atoms or ions with closed shells [Myers, 1952; Chikazumi, 2009]. Diamagnetism is also exhibited by inorganic compounds. For instance, benzene rings, in which π electron are circulating just like orbital electrons, act as closed shells. They exhibit fairly strong diamagnetism when the field is applied perpendicular to the rings, but not when the field is parallel to the plane of the ring. In the case of diamagnetic metals, conduction electrons play an important role in producing diamagnetism, which is influenced by the band structure. Generally speaking, diamagnetic susceptibility is not strong temperature dependent [Pauling, 1936; Chikazumi, 2009].

The Langevin theory does not apply to metals because they have non-localized electrons. The theory for the diamagnetism of a free electron gas is called Landau diamagnetism [Landau, 1930] the bulk case of a 3D system and low magnetic fields it can be calculated using Landau quantization:

$$\chi = \frac{e^2}{12\pi^2 mh}\sqrt{2mE_F} \ , \qquad 1.6.6$$

where E_F is the Fermi energy. This is equivalent to $-1/3\mu_B^2 g(E_F)$ exactly minus a third of Pauli paramagnetic susceptibility, where $\mu_B = \frac{eh}{(2m)}$ is the Bohr magneton and g (E) in the density of states [Landau, 1930].

1.7 Antiferromagnetism

A property possessed by some metals, alloys, and salts of transition elements in which the atomic magnetic moments, at sufficiently low temperatures, vanishing at and above a certain temperature, the Néel temperature, form an ordered array which alternates or spirals so as to give no net total moment in zero applied magnetic field. The most direct way of detecting such arrangements is by means of neutron diffraction [Kirenski, 1967].

This is, like ferromagnetism and ferrimagnetism, a manifestation of ordered magnetism [Néel, 1948]. The transition temperature below which the spontaneous antiparallel magnetic ordering takes place is called the Néel temperature. Above the Néel temperature, the material is typically

paramagnetic [Néel, 1948]. The susceptibility of an antiferromagnet is not finite at $T = T_N$ but weak cusp, as in Fig 1. 7.1 [Kittle, 1996]

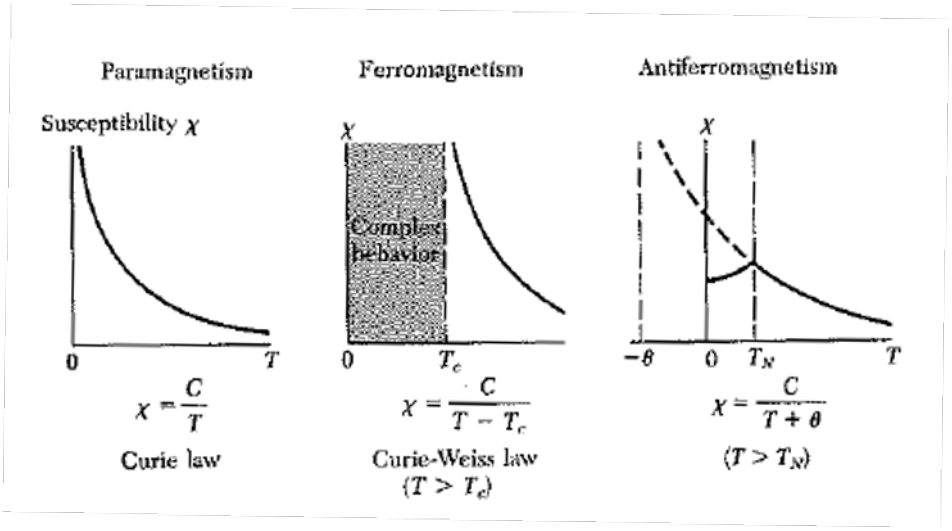

Fig 1.7.1 Temperature dependence of the magnetic susceptibility in paramagnets, ferromagnets, and antiferromagnets. Below the Neel temperature of an antiferromagnet the spin have antiparallel orientations; the susceptibility attains its maximum value at T_N *where there is a well-defined kink in the curve of* χ versus T. *The transition is also marked by peaks in the heat capacity and the thermal expansion coefficient [Kittle, 1996].*

In antiferromagnetism the elementary (atomic) magnets of adjacent particles are oriented opposite to one another (antiparallel), so that the magnetization of the body as a whole is very small as shown in Fig. 1.7.2. In ferromagnetism, orientation of the elementary magnets in the same direction results in high magnetization of the body.

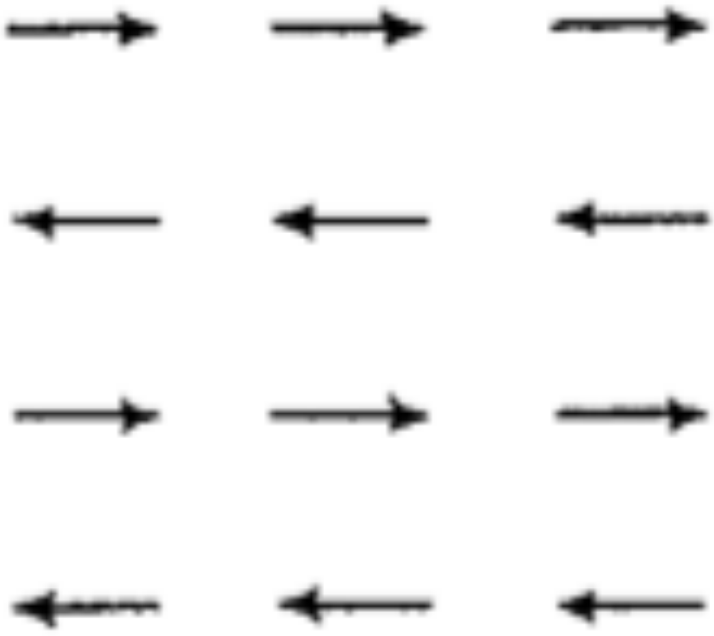

Fig 1.7.2 Antiferromagnetic spin structure [Chikazumi, 1997]

When no external field is applied, the antiferromagnetic structure corresponds to a vanishing total magnetization. In an external magnetic field, a kind of ferrimagnetic behavior may be displayed in the antiferromagnetic phase, with the absolute value of one of the sublattice magnetizations differing from that of the other sublattice, resulting in a nonzero net magnetization. Although the net magnetization should be zero at a temperature of absolute zero, the effect of spin canting often causes a small net magnetization to develop, as seen for example in hematite [Néel,1948]. A classical example of magnetic structure determination by neutron is shown in Fig. 1.7.3 for MnO, which has the NaCl structure [Kittle,1996]. At 80 K there are extra neutron reflections not present at 293K. The reflections at 80 K may be classified in terms in terms of a cubic unit cell of lattice constant 0.885 nm. At 293 K the reflections correspond to an fcc unit cell of lattice constant 0.443 nm [Kittle, 1996].

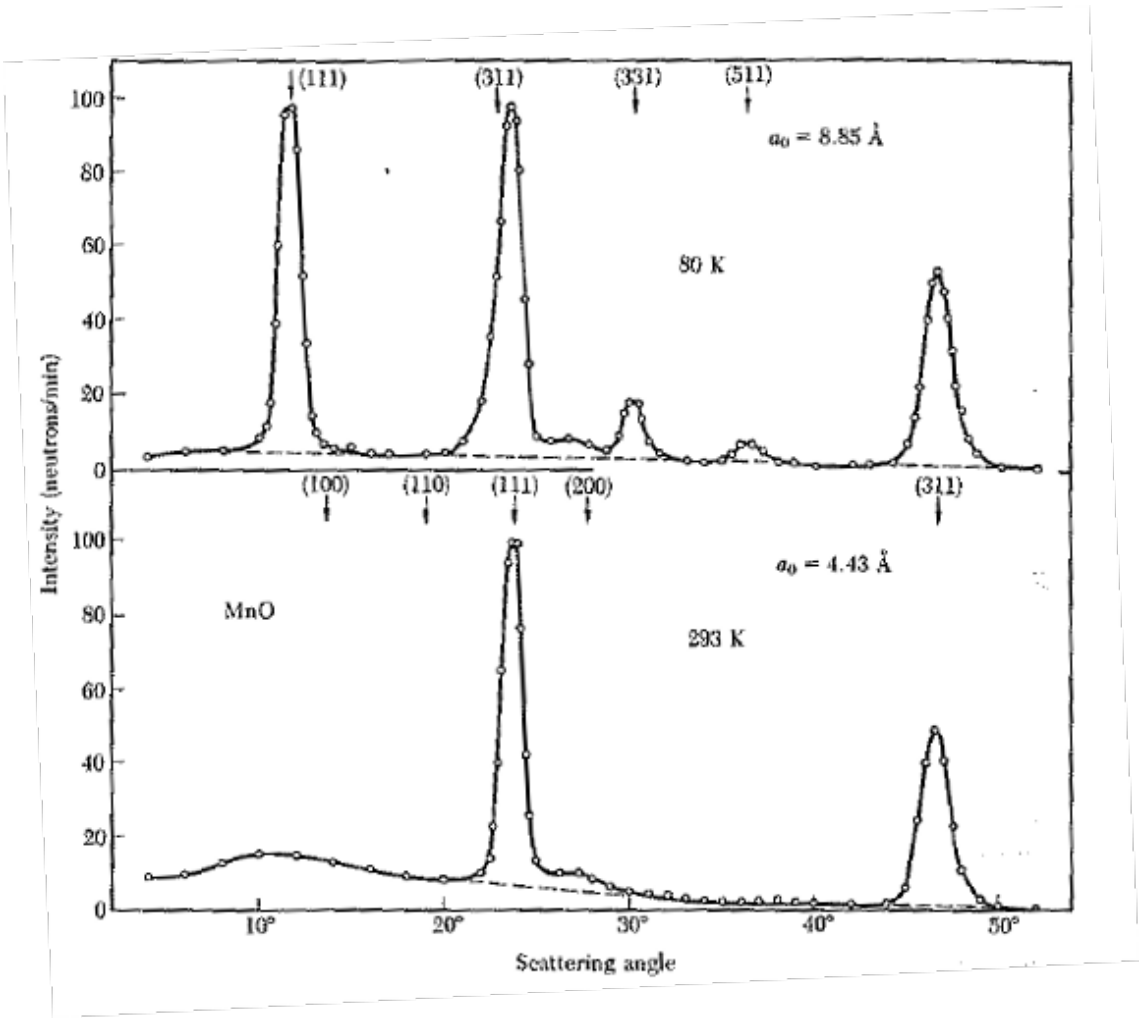

Fig 1.7.3 Neutron diffraction patterns for MnO below and above the spin-ordering temperature of 120 K, after C. G. Shull, W. A Strauser, and E.O Wollan. The reflection indices are based on an 0.885 nm cell at 80 K and on the 0.443 nm cell at 293 K. At the higher temperature the Mn^{2+} *ions are still magnetic, but they are no longer ordered* [Kittle, 1996].

But the lattice constant determined by x-ray reflection is 0.443 nm at both temperatures, 80 K and 293 K. We conclude that the chemical unit cell has the 0.443 nm lattice parameter, but that at 80 K the electronic magnetic moments of the Mn^{2+} ions are ordered in some nonferromagnetic arrangement. If the ordering were ferromagnetic, the chemical and magnetic cells would give the same reflections [Kittle, 1996].

1.8 Magnetic-field-controlled Materials

Magnetic field controlled materials (MFCMs) have been studied all over the world. For instance, giant magneto-resistance (GMR) materials, ferromagnetic shape memory alloys, magnetic refrigerants, etc. The structural, magnetic and electrical properties of these materials are changed by magnetic fields, accompanied by field-induced magnetic phase transition. It is important to clarify the basic properties in magnetic fields. Recently, Mn_2Sb system attracted attention as one of MFCMs. These compounds have received a growing interest due to the effect of magnetic field along with the tunability of the transition temperature up to and above room temperature [Pallavi et al., 2008].

Studies of the structural, magnetic, and magnetocaloric properties of $Mn_{2-x}Cr_xSb$ compounds have been reported by Caron et al., 2013. In these compounds, a first order magnetic phase transition from the ferromagnetic to the antiferromagnetic state occurs with decreasing temperature, giving rise to giant inverse magnetocaloic effects that can be tuned over a wide temperature interval through changes in substitution concentration. Entropy changes as high as 7.5 J/kg K have been observed, and a composition independent entropy change is obtained for several different concentrations/working temperatures, making these compounds suitable candidates for a composite working material [Caron et al., 2013].

Ullakko et al., 1996 reported what they believe to be the largest magnetic-field-controlled strains observed [Ullakko et al., 1996]. Strains of nearly 0.2% has been induced along [001] in unstressed crystals of Ni_2MnGa with magnetic fields of 8 kOe applied at 265 K. These strain are associated with the superelastic motion of twin boundaries in the martensitic phase that is stable below about 274 K. Numerous candidate materials systems are being explored including Ni_2MnGa, Co_2MnGa, FePt, CoNi [Ullakko et al., 1996].

Sozinov et al., 2002 observed a giant magnetic-field –induced strain of about 9.5% at ambient temperature in a magnetic field of less than 1 T in NiMnGa orthorhombic seven-layered martensitic phase. The strain proved to be caused by magnetic-field-controlled twin boundary motion. According to analysis of x-ray diffraction data, the crystal structure of this phase is nearly orthorhombic, having lattice parameters a = 0.619 nm, b = 0.580 nm, and c = 0.553 nm (in cubic parent phase coordinates) at ambient temperature. Seven-layer shuffling-type modulation along the (110) $[110]_p$ system was recorded. Magnetic shape memory materials are expected to have a high potential in the design of a different kind of actuating devices. Important because the low twinning stress and high energy of magnetic anisotropy are key to obtaining a large magnetic field controlled strain response. The structural and magnetic properties of Mn_2Sb system is shown in Table 1.8.1.

TABLE 1.8.1 Structural and magnetic properties of Mn_2Sb system

Compounds	a (Å)	c (Å)	V (Å^3)	T_c (K)	T_t (K)	M_s(Am^2kg^{-1})	References
$Mn_{1.94}Cr_{0.06}Sb$	4.07952(3)	6.53651(3)	108.784(1)	520	-	36	Caron et al., 2013
$Mn_{1.92}Cr_{0.08}Sb$	4.08075(3)	6.53330(2)	108.796(1)	510	-	33	Caron et al., 2013
$Mn_{1.9}Cr_{0.1}Sb$	4.08708(3)	6.52545(3)	109.003(1)	505	-	29	Caron et al., 2013
$Mn_{1.88}Cr_{0.12}Sb$	4.08859(3)	6.51117(2)	108.844(1)	490	-	27	Caron et al., 2013
$Mn_{1.8}Co_{0.2}Sb$	0.4077	0.6455	0.1053	-	145	49.5	Orihashi et al., 2013
$Mn_2Sb_{0.95}Ge_{0.05}$	0.4051	0.6538	-	-	172	32	Koyama et al., 2013
$Mn_2Sb_{0.9}Sn_{0.1}$	0.4077	0.6568	-	-	190	35	Koyama et al., 2013
$Mn_2Sb_{0.92}Ge_{0.08}$	.40480	0.6538	-	532	-	29	Shimada et al., 2013
$Mn_{1.94}Cu_{0.06}Sb$	0.4078	0.6549	-	517	-	35	Matsumoto et al., 2014

1.9 Structure and Magnetic Properties of Mn_2Sb Compounds

Manganese antimonide is a ferrimagnet with a Curie temperature T_C = 550 K. The single crystal measurement by Guillaud et al. (1949) showed that the ferromagnetic moment was located in the c plane at temperatures below 240 K and along the c axis in the temperature range 240 K < T < 550 K. The magnetic structures proposed by Guillaud et al. is shown in the Fig 1.9.1, and was later verified by Wilkinson et al. (1957) from neutron-scattering experiments. The crystal structure of the Mn_2Sb is tetragonal (space group P4/nmm) and contains Mn atoms at two nonequivalent sites, as shown in Fig. 1.9.1 (b). Mn(I) atoms occupies the 2a position (0 0 0) and (1/2 1/2 0) while Mn(II) atoms whose spin are oppositely directed occupies the 2c positions (0 1/2 μ) and (1/2 0 μ). Sb atoms are located at the 2c positions [Ohashi, 1992]. The Mn(I) and Mn(II) atoms in Mn_2Sb have saturation magnetic moments of 2.1 μ_B and 3.9 μ_B respectively in the ferrimagnetic state [Wilkson, 1957, Nakamura, 1976, Kanomata 1984]. This gives a net ferrrimagnetic moment of 0.87(22) μ_B per Mn atom, in fair agreement with that found by Guillaud et al. (1949). In pure Mn_2Sb the Mn_I moments below

the Curie temperature T_C = 550 K as indicated in Fig. 1.9.1 (a). This results in a net saturation moment of 3.6 μ_B per unit cell. The orientation of the moments changes at the spin flop transition temperature T_t = 240 K from parallel to the crystallographic c-axis at $T > T_t$ to perpendicular to this axis at $T < T_t$ [Blaauw, 1978].

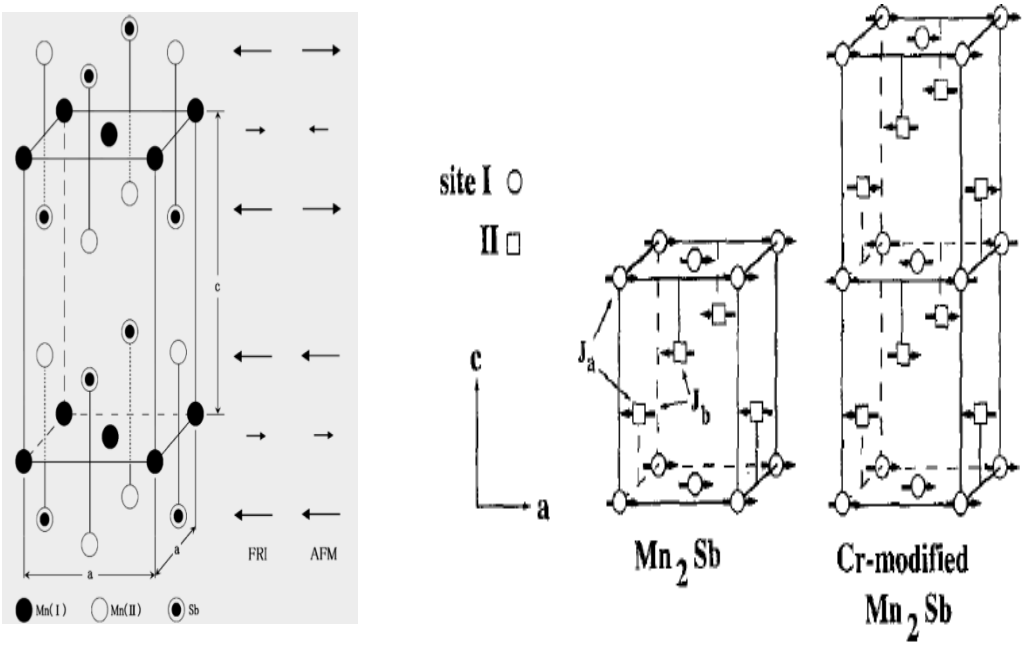

(a) *(b)* *(c)*

Fig 1.9.1 (a) Crystal structure and arrangement of Mn(I) and Mn(II) moments in ferrimagnetic (FRI) and antiferromagnetic (AFM) states in Mn_2Sb based compounds. The length of the arrow represents the magnitude of the magnetic moment of the atom [Kanomata, 1984]. (b) Magnetic structure of Mn_2Sb (after Guillaud et al., 1949, Wilkinson et al., 1957) and (c) the low temperature ferromagnetic structure of Cr-modified Mn_2Sb (after Cloud et al. 1960, 1961). For the temperature dependence of the direction of the easy axis of magnetization, see fig. 1.9.2. The low-temperature magnetic structure of Cr-modified Mn_2Sb is the same as the structure of Mn_2As (see fig. 1.9.2) [Beckman and Lundgren, 1991]

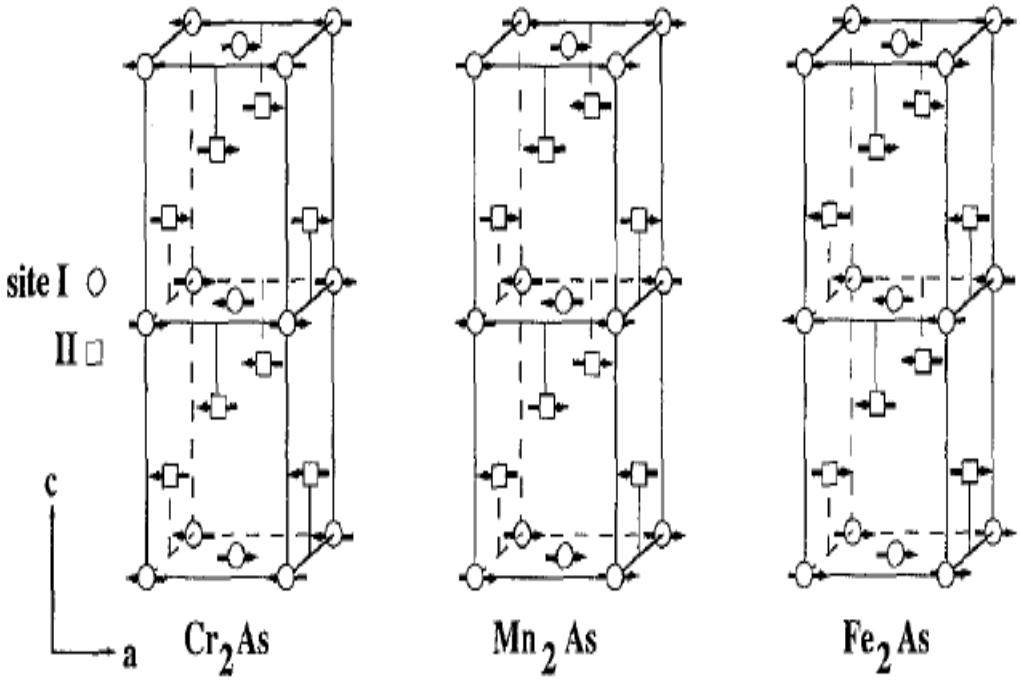

Fig 1.9.2 Magnetic structures of the tetragonal compounds Cr_2As, Mn_2As and Fe_2As [Beckman and Lundgren, 1991]

1.9.1 Substitution Effects

In fact, more investigations on the Mn_2Sb compounds were focused on the magnetic field controlled materials (MFCMs)[Kuswaha et al. 2008].

i) Substitutions by magnetic Mn atom and non-magnetic Sb atom

The Mn_2Sb-based compounds with manganese atoms substituted by a number of elements (chromium, copper, zinc, cobalt and vanadium) and with antimony atoms substituted by arsenic, tin and germanium exhibit first-order magnetic phase transitions from ferrimagnetic (FRI) to the antiferromagnetic (AFM) state at $T = T_t$, as the temperature decreases [Baranov, 1994, Kanomata, 1984]. The magnetic phase diagrams obtained by Kanomata and Ido (1984) and Bither et al. (1962b) are schematically represented in fig. 1.9.1.1 The Cr substitution gives rise to critical situation. The occurrence of an antiferromagnetic state in Cr-modified Mn_2Sb at low temperature was verified by neutron scattering experiments by Cloud et al. (1960, 1961). The magnetic structure is shown in fig. 1.9.1.2. The basic magnetic sublattice of Mn_2Sb is the three-layered set of adjacent Mn(II)-Mn(I)-Mn(II) planes having the ferromagnetic moment $|\mu(Mn_{II}) - \mu(Mn_I)|$. Ferromagnetic ordering of the sublattices gives rise to magnetic structure of Mn_2Sb. Antiferromagnetic ordering of these sublattices gives the low temperature magnetic structure of $Mn_{2-t}Cr_tSb$ which results in a doubling of the magnetic cell along the *c* direction. The torque and the magnetization measurements show that for both the ferri- and antiferromagnetic states a change from

positive to negative uniaxial anisotropy occurs with decreasing temperatures. The direction of easy magnetization depends on the temperature and Cr content as shown in fig. 1.9.1.2.

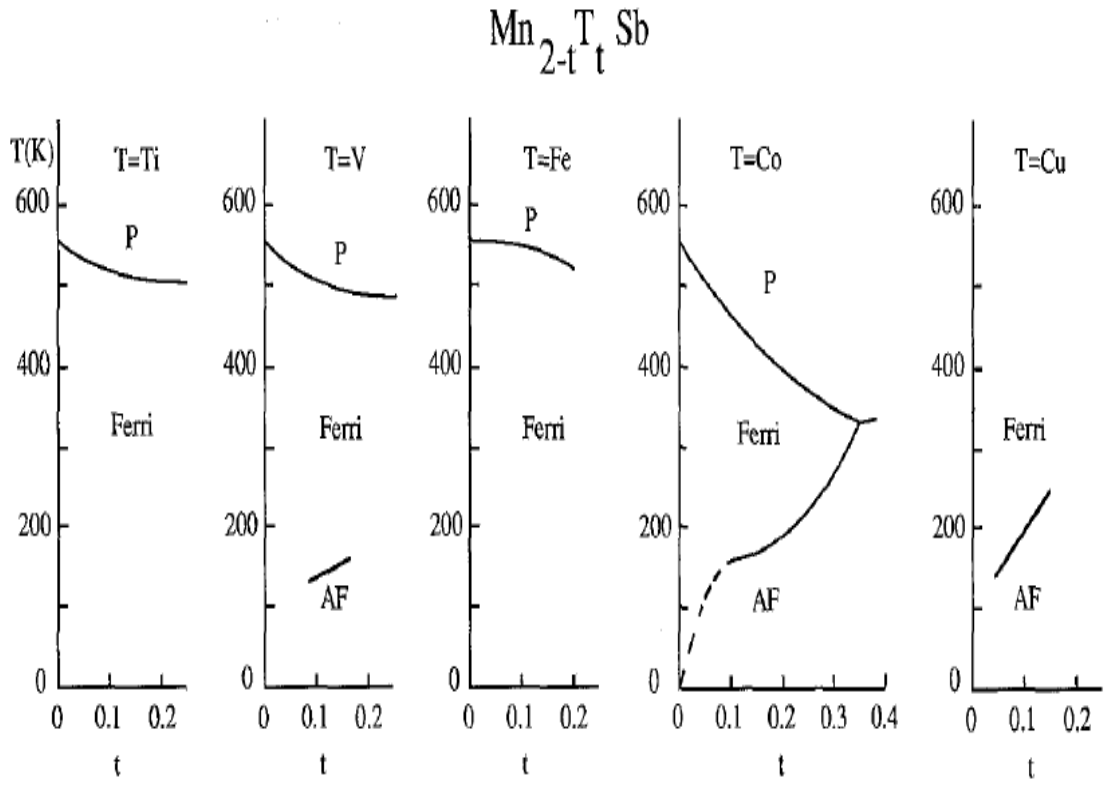

Fig. 1.9.1.1 Magnetic phase diagrams of some $Mn_{2-t}T_tSb$ compounds, T= Ti, V, Fe, Co or Cu (after Kanomata and Ido 1984, Bither et al. 1962b) [Beckman and Lundgren, 1991]

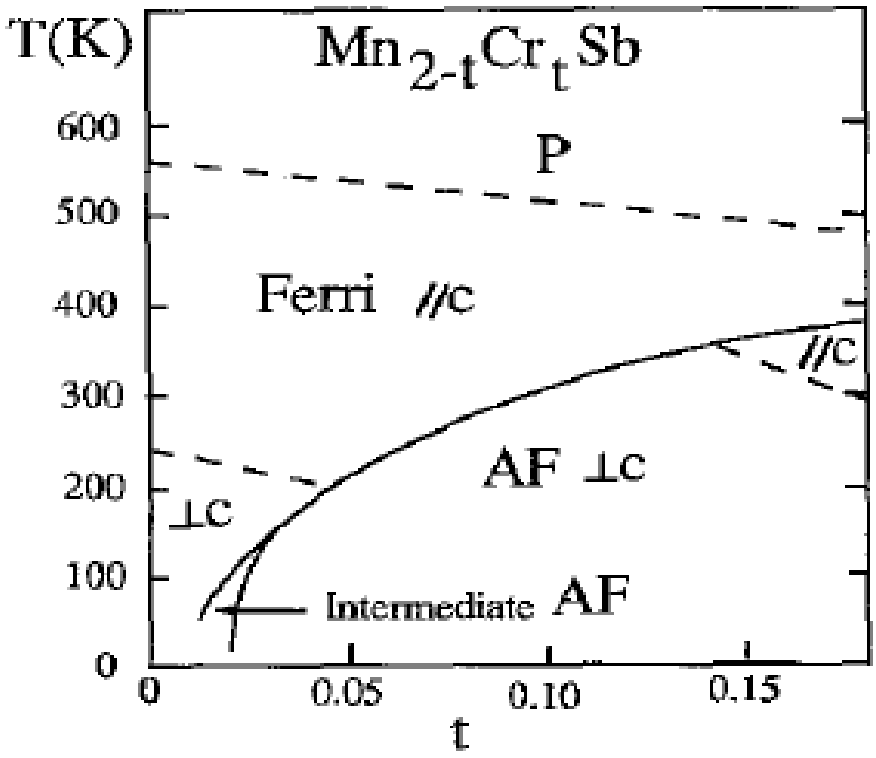

Fig 1.9.1.2 Magnetic phase diagram of $Mn_{2-t}Cr_tSb$ compounds. The direction of the magnetic moments is indicated. The solid lines represent first-order transitions and the dotted lines second-order transitions (after Darnell et al., 1963) [Beckman and Lundgren, 1991].

The magnetic moments of Mn(I) and Mn(II) in the solid solution were determined from the neutron diffraction data at 297 and 78 K by Sirota and Ryzhkovskii (1975). As can be seen in fig. 1.9.1.3(a), both magnetic moments decrease monotonously with increasing Sb concentration in the

range 0.4 $\leq$ x $\leq$ 1. Increasing the As concentration to 15% in the solution based on Mn_2Sb reduces the Mn(II) moment at 297 K from 3 μ_B for Mn_2Sb to 2.7 for $Mn_2As_{0.15}Sb_{0.85}$, and at 78 K from 3.8μ_B to 3.4μ_B, respectively. Simultaneously, the Mn(I) moment initially decreases with increasing As content from 1.7 μ_B for Mn_2Sb to 1.55 μ_B for As content of 5% passes through a minimum, and then increases with a subsequent increase of the As content to 1.9 μ_B for $Mn_2Sb_{0.85}As_{0.15}$ at 297 K.

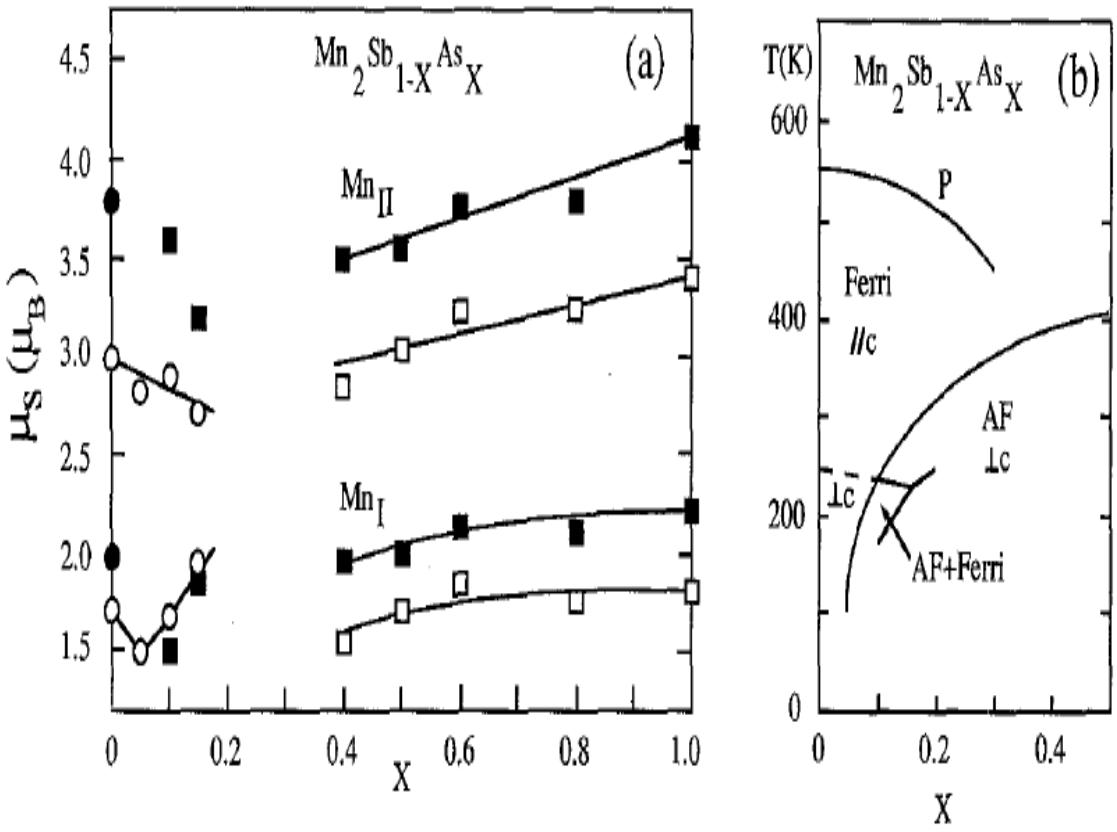

Fig. 1.9.1.3 (a) Magnetic moments (μ,) versus x for $Mn_2Sb_{1-x}As$ compounds. Solid symbols are data at 78 k and open symbols data at 297 K. Circles represent ferromagnetic and squares antiferromagnetic structures (after Sirota and Ryzhkovskii 1975). (b) Magnetic moments is indicated (after Ryzhovskii) [Beckman and Lundgren, 1991]

.

However, $(MnFe)_2Sb_{1-x}Sn_x$ ($0.01 \leq x \leq 0.15$) FRI-PM 1st order phase transition has not been reported. By studying the magnetization of the compound, one may hope to obtain the information about the magnetic properties in high magnetic field. In this work, we present the results of a high magnetic-field magnetization processes of the compound $(MnFe)_2Sb_{1-x}Sn_x$ ($0.01 \leq x \leq 0.15$) up to 5 T in the wide temperature ranging from 10 to 380 K. Preliminary results were reported previously [Nwodo et al., 2018].

1.10 The Aim of This Work

Motivated by the earlier report of the magnetization and electrical resistivity measurements for polycrystalline $Mn_2Sb_{1-x}Ge_x$ ($0.05 \leq x \leq 0.2$) and $Mn_2Sb_{1-x}Sn_x$ ($0.08 \leq x \leq 0.15$) in magnetic fields up to 16 T in the 4.2–600 K temperature range in order to investigate the magnetic and the electrical properties under magnetic fields. A first-order magnetic transition (FOMT) from a ferrimagnetic (FRI) to an antiferromagnetic (AFM) phase in the vicinity of T_t = 172 K and 190 K, were observed for $Mn_2Sb_{0.95}Ge_{0.05}$ and $Mn_2Sb_{0.9}Sn_{0.1}$ respectively, with decreasing temperature in a zero magnetic

field [Koyama et al., 2013]. We began to investigate Mn_2Sb and related compounds, in order to clarify the magnetic and structural properties of the compound and to estimate the potential for application, using high magnetic fields. Many authors [Baranov, 1994, Kanomata, 1984, Bither 1962, Shirakawa 1976, Blaauw 1978, Beckman and Lundgren, 1991, Kushwaha 2008] have reported that the first order magnetic phase transition from a FRI to an AFM with decreasing temperature can be produced by Cr, Zn, Cu, Co, and V substitution for Mn atoms and As and Ge substitution for Sb in Mn_2Sb. Fig. 1.10.1 shows the FRI-AFM transition temperature of $Mn_{2-x}A_xSb$, A = Cr, V, Cu, Co and $Mn_2Sb_{1-x}Z_x$ 、 Z= Ge, As exhibiting a first order phase transition. Below T_t an applied magnetic field induces the first-order AFM-FRI transition when the field reaches the critical value H_c [Baranov, 1994]. However, $Mn_{2-x}Fe_xSb$, FRI-PM exhibiting a first order phase transition has not been reported so far. Therefore, I studied the Fe substituted $Mn_2Sb_{1-y}Sn_y$.

My investigation of the properties using high magnetic fields revealed interesting magnetic properties. Specifically, it has been observed that by substituting a small amount of nonmagnetic Fe, a temperature dependence transition is induced from the ferromagnetic state characteristics of Mn_2Sb_{1-}

$_{y}Sn_{y}$ to a paramagnetic. The transition has been studied most extensively in Fe substituted Mn in $Mn_2Sb_{0.9}Sn_{0.1}$.

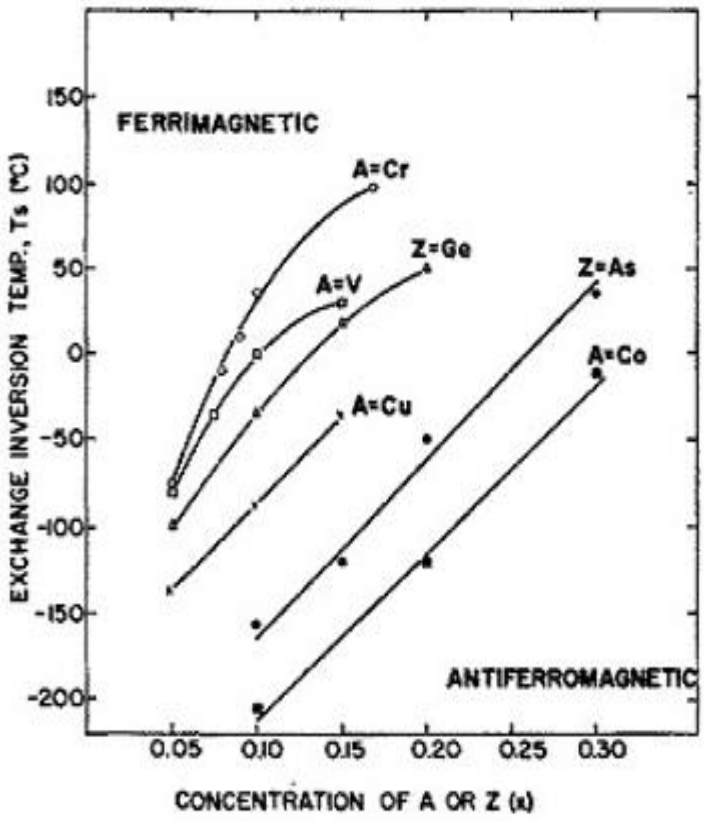

Fig. 1.10.1 Ferrimagnetic-antiferromagnetic transition temperatures of $Mn_{2-x}A_xSb$ and $Mn_2Z_xSb_{1-x}$ compounds (x between 0.05-0.30) [Bither, 1962]

The purpose of this thesis is mainly the following: (1) study the structural properties of $Mn_{2-x}Fe_xSb_{1-y}Sn_y$ compounds in zero magnetic field by room temperature X-ray powder diffraction (XRD) measurements. (2)

Study the structure characteristics of the $Mn_{1.9}Fe_{0.1}Sb_{0.9}Sn_{0.1}$ compound in high field by X-ray powder diffraction (HF-XRD) measurements in order to clarify the structural properties in magnetic fields. (3) Investigate systematically the behavior of the intrinsic magnetic properties of the $Mn_{2-x}Fe_xSb_{1-y}Sn_y$ ($0.05 \leq x \leq 0.15$, $0.05 \leq y \leq 0.1$) compounds across the magnetic field controlled material series, including critical temperature, magnetization, and spin reorientations; interpret the results in terms of molecular field theory. (4) Study the thermal properties of the $Mn_{1.9}Fe_{0.1}Sb_{0.9}Sn_{0.1}$ compound; understand the response of a material to the application of heat. (5) Compare the effects of these properties on the $Mn_{2-x}Fe_xSb_{1-y}Sn_y$ ($0.05 \leq x \leq 0.15$, $0.05 \leq y \leq 0.1$) compounds.

Chapter 2

Experimental Methods

The purpose of this chapter is to present the various important experimental techniques used to prepare and test the samples which are the subject of this thesis. The experimental procedures will be presented later.

2.1 Sample Preparation

The $Mn_{2-x}Fe_xSb_{1-y}Sn_y$ ($0.05 \leq x \leq 0.15$, $0.05 \leq y \leq 0.1$) polycrystalline sample was prepared by arc melting the appropriate pure elements (at least 99.9% purity) under argon atmosphere. To ensure homogeneity, the sample was turned over and remelted 3 or 4 times. In this way, the sample of about 2 grams could be prepared. After that, the ingot was annealed at 923K for 24h in quartz tube with vacuum. The block diagram of the arc furnace is shown in Fig. 2.1.1. Typical working condition of the arc furnace were ~ 50 kPa argon atmosphere and ~ 100 A current.

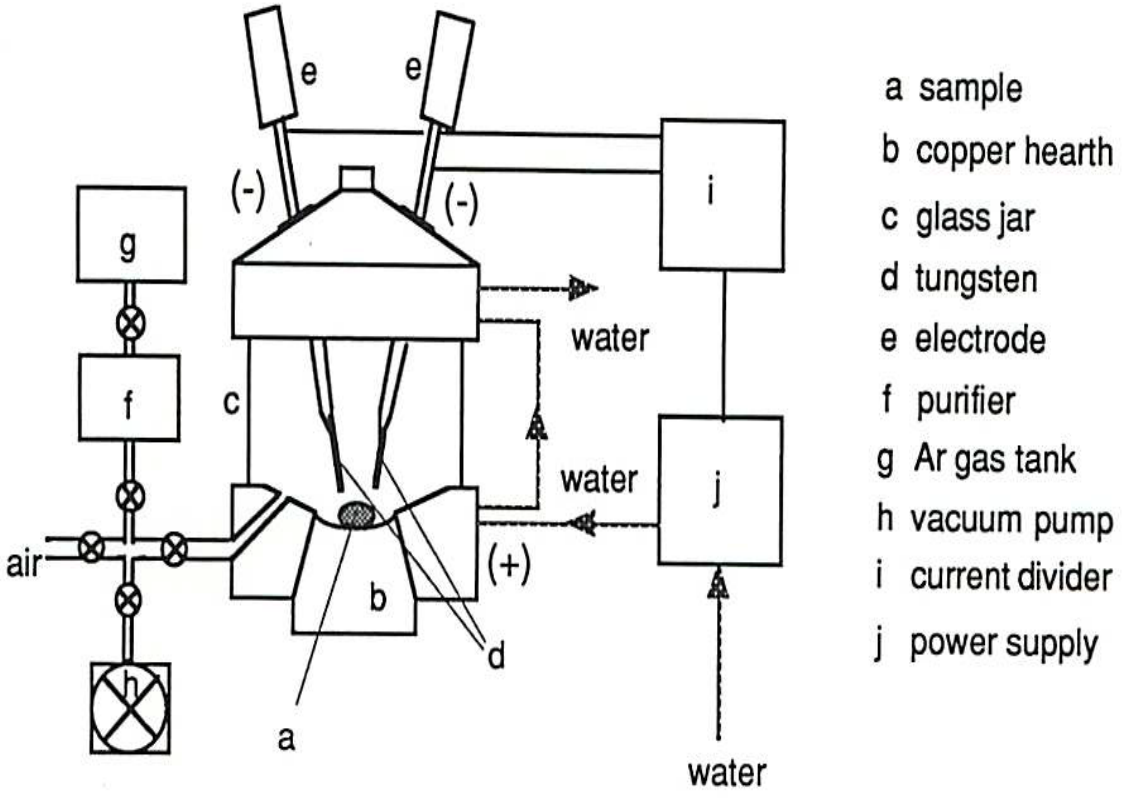

Fig. 2.1.1 Schematic diagram of argon arc furnace [Koyama, 1997]

2.2 Structure Characterization

Standard X-ray diffraction techniques were extensively used to verify the structure and purity of polycrystalline powder and to determine lattice parameters.

2.2.1 X-ray diffraction Measurement under Zero Magnetic field

X-ray diffraction measurements were carried out using Cu Kα radiation at room temperature (RT) to exam the quality of the samples at every stage of the sample preparation process. The sample were confirmed to be almost single phase with the Cu_2Sb-type structure. X-ray diffraction patterns were taken for the powder along the direction parallel to the scattering vector. Cu Kα radiation beam was used. The sample was measured in the 2θ range from 20^0 to 90^0 by using the step scanning techniques with the sweep rate of 0.05 deg./min. and with measuring time of 2 sec/step. The diffractometer was controlled by a Window computer, and the data could be analyzed by RIGAKU software. The beam path of the diffractometer for θ-2θ as the sample is moved to be at angle θ from the incident beam, the detector is moved to 2θ is shown in Fig 2.2.1.1. The lattice parameters were obtained by using fitting square's program to index the X-ray pattern.

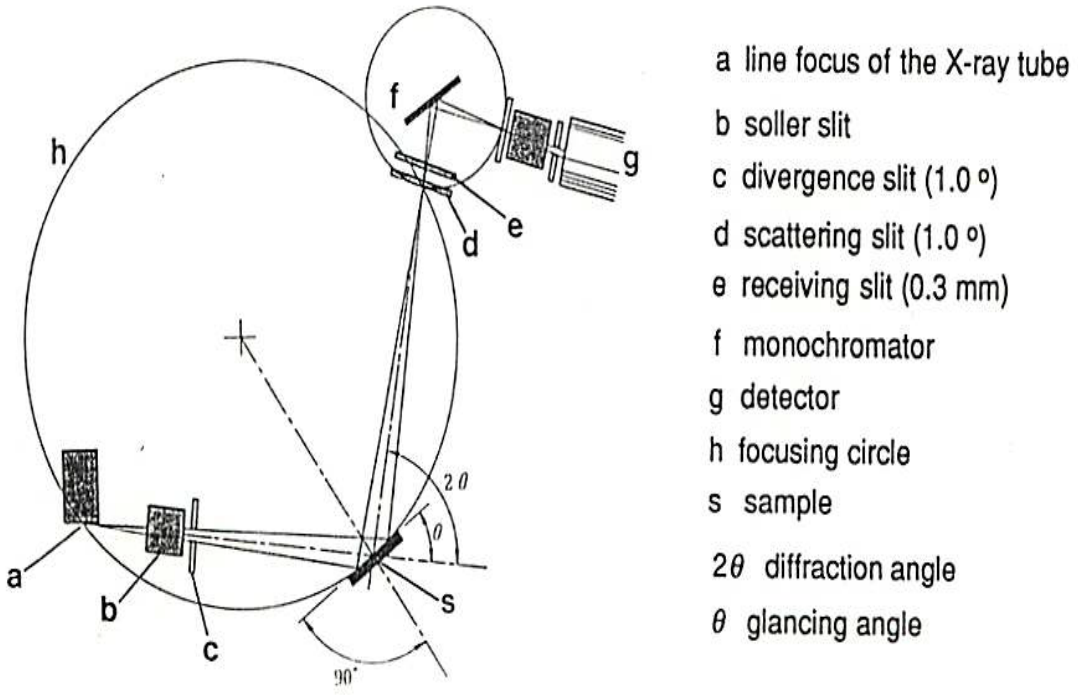

Fig 2.2.1.1 Beam path of diffractometer in case of 2θ/θ position [Koyama, 1997]

2.2.2 X-ray Diffraction Measurements under High Magnetic field up to 5 T

High-field powder x-ray diffraction experiments were carried out using Cu Kα radiation under magnetic field of 5 T at the High Field

Laboratory for Superconducting Materials, Institute for Materials Research, Tohoku University. The apparatus mainly consists of a Gifford-McMahon (GM) type cryocooler (helium gas closed-cycle refrigerator) and for using the magnetic field of 5 T using a cryocooled split-pair NbTi superconducting magnet and a diffractometer [Koyama et al, 2008, Watanabe et al., 1998] as shown in Fig. 2.2.2.1. Fig. 2.2.2.1 is the overall view of the high field low temperature X-ray diffraction system. The inset shows the powder sample fixed with apiezon grease on a copper boat holder that is mounted on the second stage of the cryocooler in the sample cryostat. The cryocooled superconducting magnet generates magnetic fields up to 5 T at the centre of a vertical room temperature bore of 50 mm and a horizontal room temperature gap of 10 mm with the homogeneity of 0.1%. The cryocooled superconducting magnetic was mounted on a θ-2θ gonimeter head, and the sample cryostat with a GM cryocooler also was set into a 50 mm room temperature as shown in Fig. 2.2.2.1. Fig. 2.2.2.2 shows the Schematic diagram of the high field low temperature X-ray diffraction system consisting of a cryocooled superconducting magnet and a cryostat [Watanabe et al., 1998]. The apparatus employs a conventional shield-tube

(3 kW) for an X-ray source. A scintillation detector was used in our apparatus on which passive magnetic field shielding was done using a silicon steel with high permeability. In order to eliminate a Kβ radiation, we applied a graphite-curved monochromator at the front of the scintillation detector. The sample cryostat was also conductively cooled from room temperature down to 8 K using a GM cryocooler. The sample temperature was controlled within ± 0.1 K at temperature ranging from 8 up to 330 K by a heater. A powder sample of $(MnFe)_2Sb_{1-y}Sn_y$ ($0.05 \leq y \leq 0.1$) was fixed with Apiezon grease on a copper boat holder with a size of 14 mm in height and 20 mm in width, as shown in Fig. 2.2.2.3. A copper holder was attached onto a second stage of a GM cryocooler. A sample temperature was controlled by changing a second stage temperature. It was confirmed that all powder samples were not removed by the magnetic force until the measurements. The diffraction data can be taken in the 2θ range from 0◦ to 90◦ with a step size of 0.002◦ and sweep rate of 0.05 deg./min. For determining the X-ray reflection line indices and the crystal structure, the observed diffraction profiles were analyzed by comparison with calculated profiles using a Rietveld program (RIETAN) [Izumi, 1995; Koyama et al., 2006].

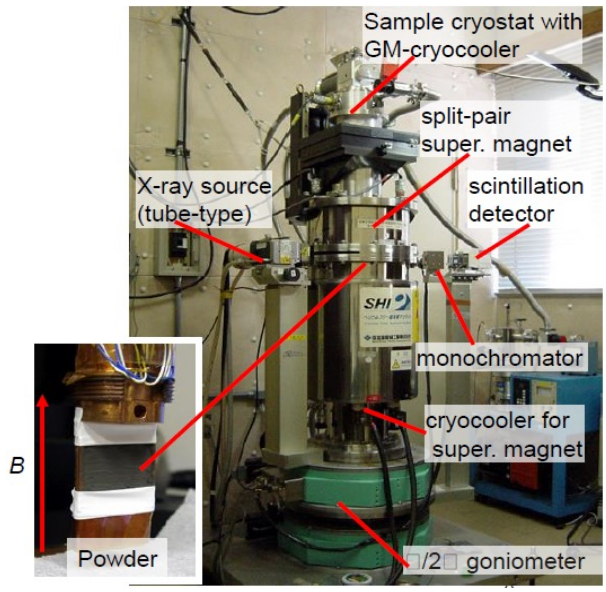

Fig. 2.2.2.1. *Overall view of the high field low temperature X-ray diffraction system. The inset shows the powder sample fixed with apiezon grease on a copper boat holder that is mounted on the second stage of the cryocooler in the sample cryostat.*

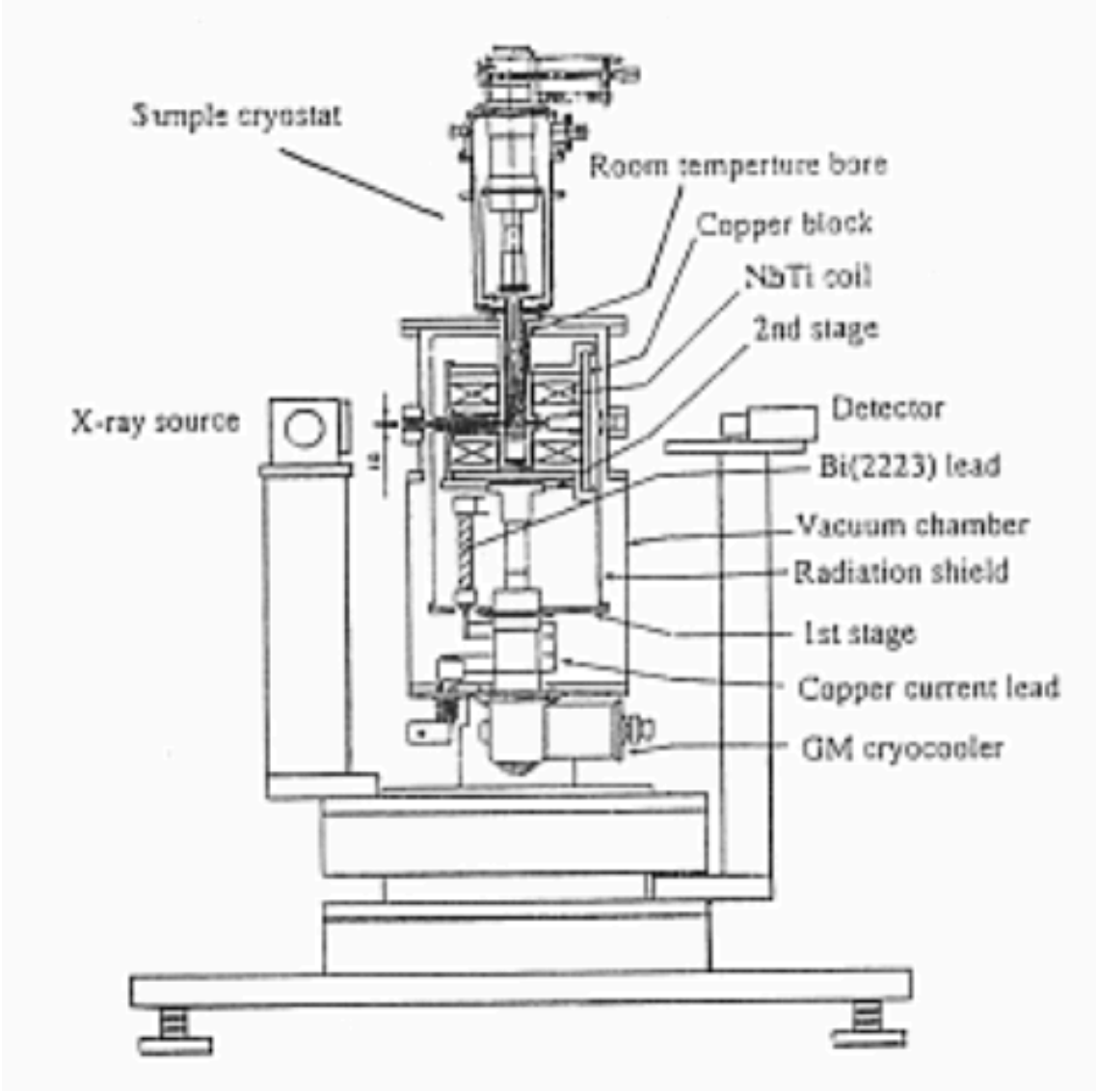

Fig. 2.2.2.2 Schematic diagram of high field low temperature X-ray diffraction system consisting of a cryocooled superconducting magnet and a cryostat [Watanabe et al., 1998].

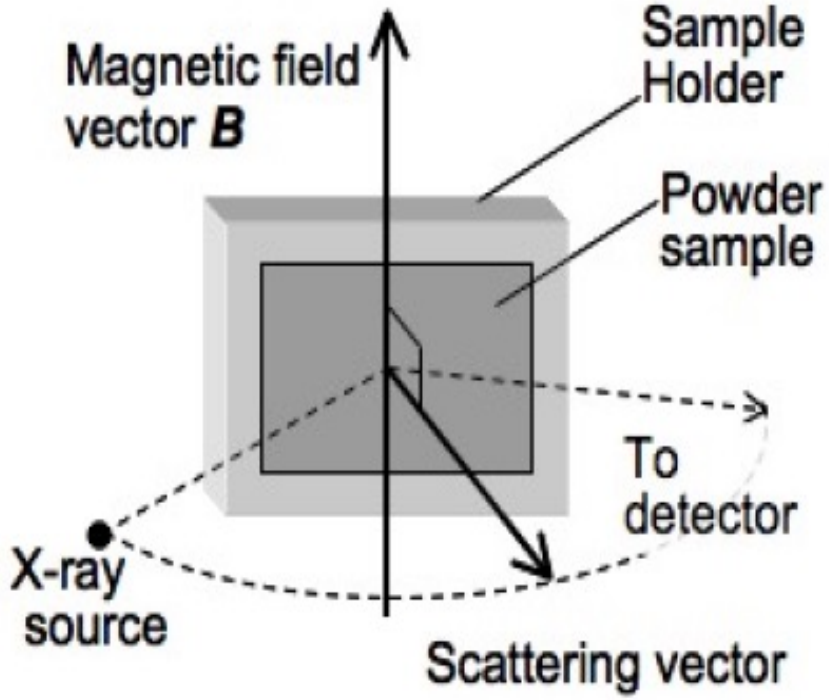

Figure 2.2.2.3. Schematic configuration of the powder sample and the x-ray beam path from the source to the detector. The powder sample was fixed using Apiezon grease on the copper holder in the cryostat. The X-ray scattering vector is perpendicular to the magnetic field vector [Koyama et al., 2008].

2.3.0 Magnetic Measurement

Curie temperature, saturation magnetization, spin reorientation temperature are the essential intrinsic magnetic parameters. These parameters can be determined directly from magnetic measurements.

2.3.1 High-field Magnetic Measurement

The magnetization in high magnetic field at 5 T, and for the temperature *T* range of 10-360 K, was measured using a superconducting quantum interference device (SQUID) magnetometer (Quantum Design MPMS (magnetic properties measurement system)), at the Institute for Solid State Physics, University of Tokyo.

Superconducting quantum interference devices (SQUIDs) have been a key factor in the development and commercialization of ultrasensitive electric and magnetic measurement systems. The most sensitive magnetic flux detector is the superconducting quantum interference device (SQUID). This device, operating at cryogenic temperatures with quantum-limited

sensitivity, has demonstrated field resolution at the 10^{-17} T level [Fagaly, 2006]. Figure 2.3.1.1 shows a schematic of a typical dc SQUID.

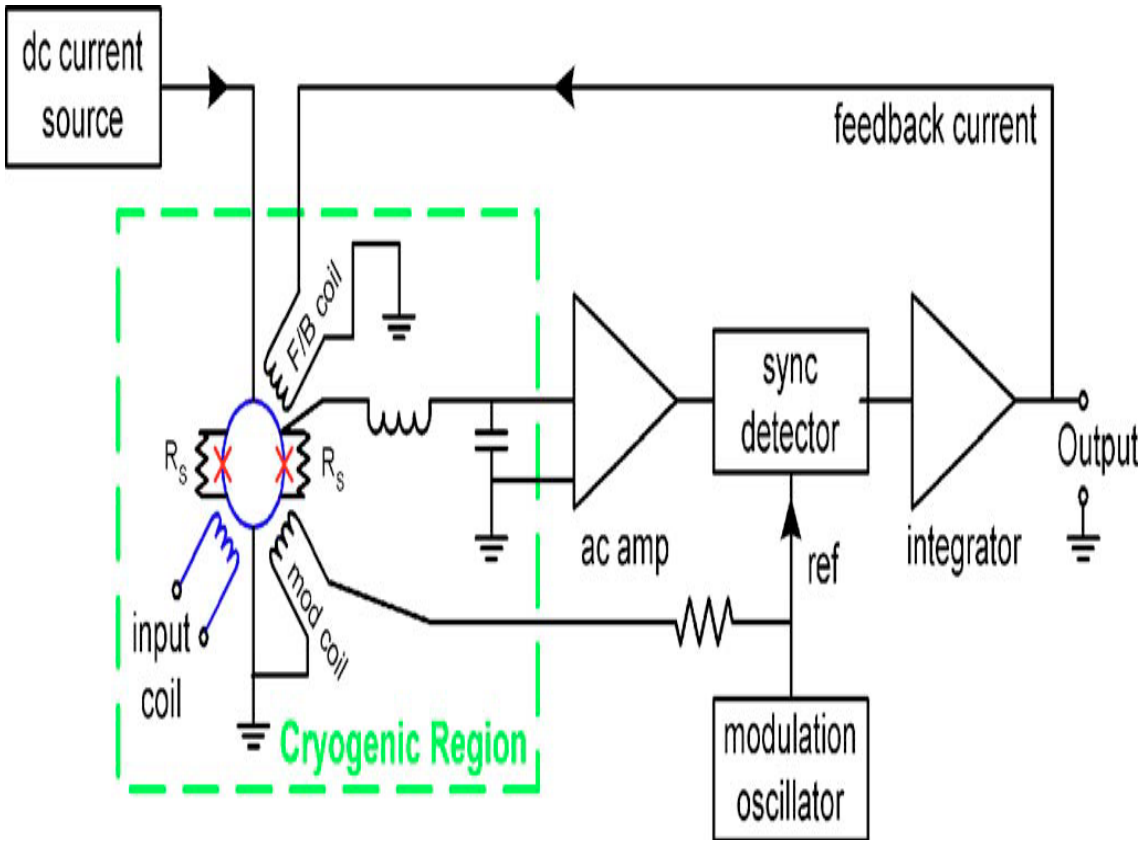

FIG. 2.3.1.1. Block diagram of a typical dc SQUID. The detection coil (connected to the input coil) is omitted for clarity [Fagaly, 2006]

A powder sample of $(MnFe)_2Sb_{1-y}Sn_y$ ($0.05 \leq y \leq 0.1$) was attached using a clear drinking straw as shown in Fig. 2.3.1.2 The straw has minimal magnetic susceptibility and thus a useful means of attaching the sample.

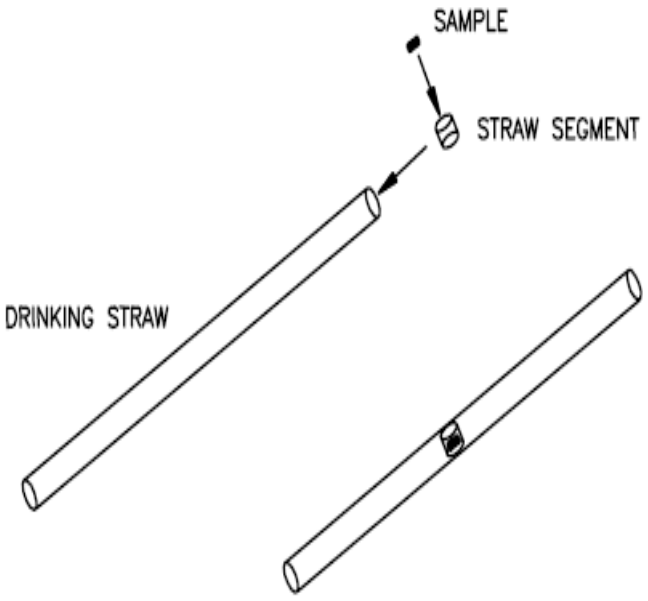

Fig 2.3.1.2 Correctly position sample [MPMS multiVu user's manual, 2004]

The slide seal plug was moved up and down part of the sample rod to verify that the rod was well lubricated. The two slide seal clamps on the

socket block assembly was pushed as shown in Fig. 2.3.1.3 and Fig. 2.3.1.4 so that the handles of the clamps face the front of the MPMS.

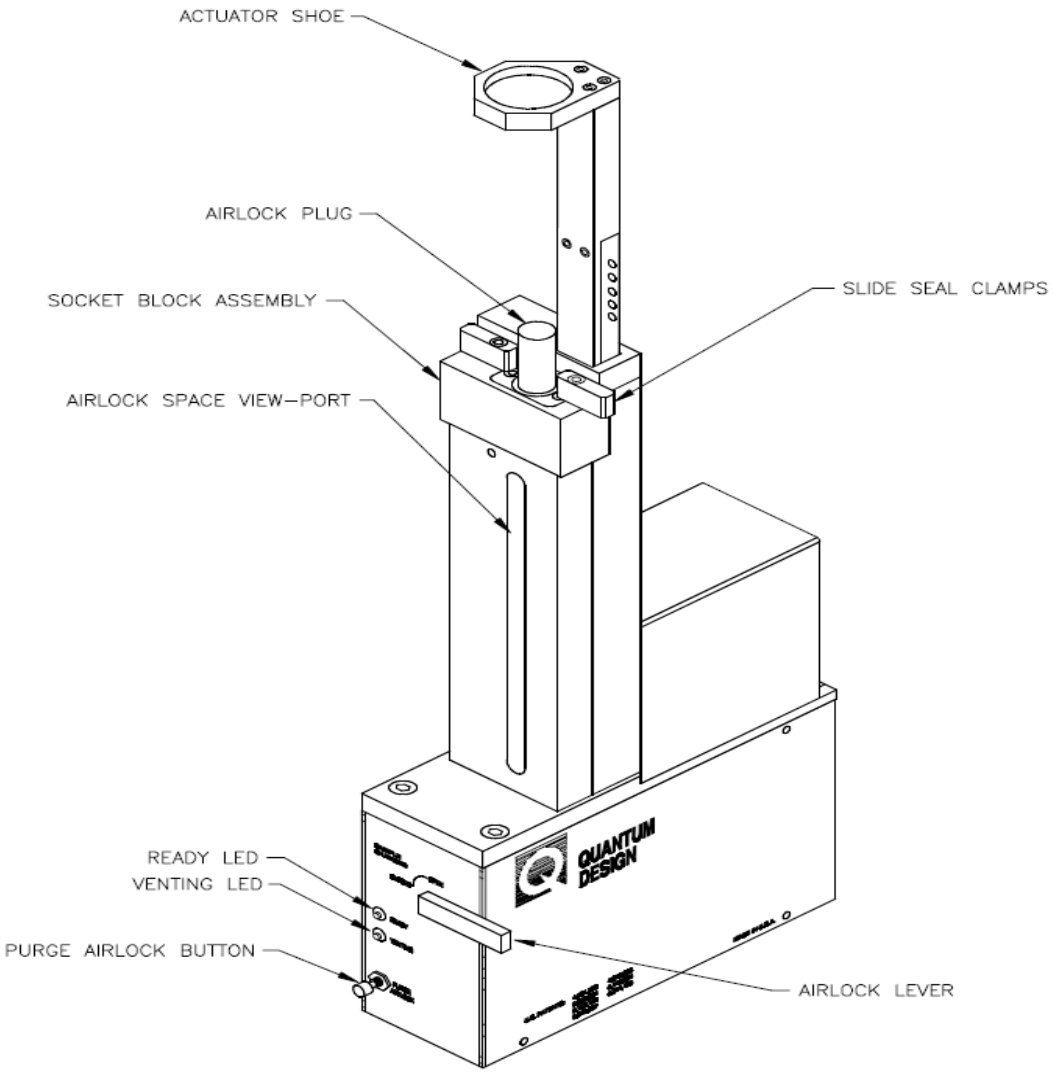

Fig 2.3.1.3. Sample Transport and Electronic Control Assembly [MPMS multiVu user's manual, 2004]

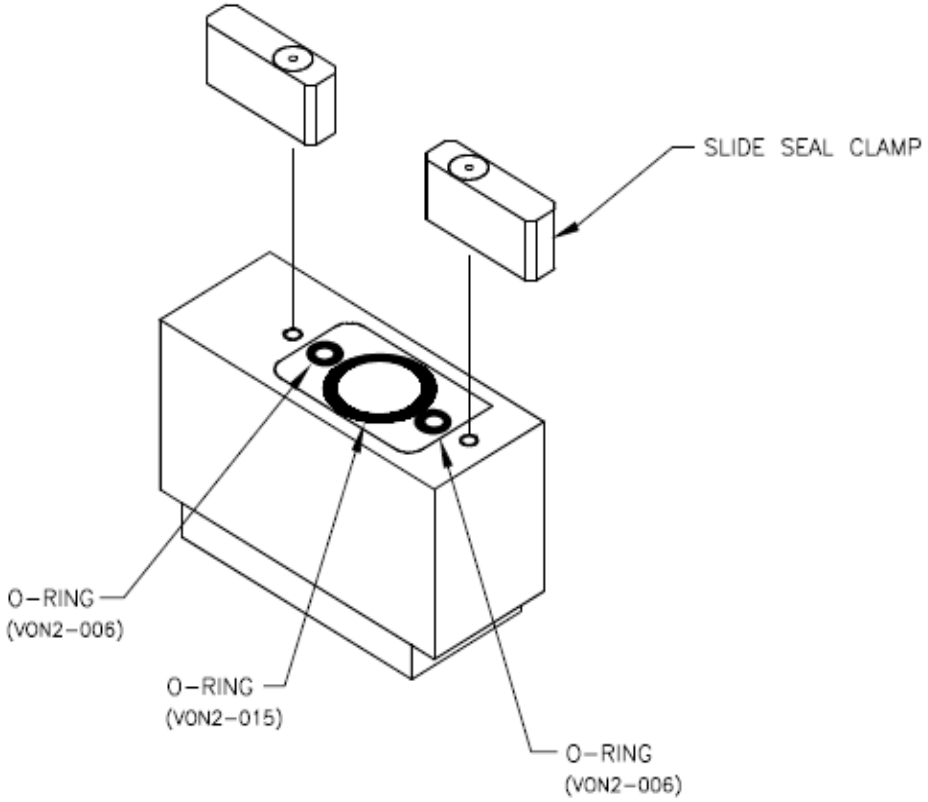

Fig.2.3.1.4 O-Ring on socket Block Assembly [MPMS multiVu user's manual, 2004]

The clip screws were tightened. The clip screws secure the sample rod to the actuator shoe, so the sample transport can move the rod vertically. SQUID employs a superconducting pickup coil in a flux transformer configuration. The pickup coil is coupled inductively to a superconducting quantum interference device (SQUID) acting as a flux-to-voltage sensor

[Jansen, 2003]. The centering measurement was initiated, the sample transport moved upward, carrying the sample through the pickup coils. While the sample moved through the coils, MPMS MultiVu (software) measured the SQUID's response to the magnetic moment of the sample and saved all data from the centering measurement to the centering scan data, or "center.dc.lastscan", file. Sample moments between 10^{-12} and 10^{-13} Am^2 can be determined with an accuracy of 0.1% [Jansen, 2003]. Status messages appearing at the top of the DC Centering dialog box identify the specific task MPMS MultiVu is performing. Figure 2.3.1.5 illustrates the progress of a centering measurement. The plot of the center.dc.lastscan file was examined to determine whether the sample was centered in the SQUID pickup coils. As shown in figure 2.3.1.5. The sample is centered when the peak of the large, middle curve is within 0.05 cm of the half-way point of the scan length. In a 6-cm scan, for example, the sample is centered when the peak of the middle curve is within 0.05 cm of the 3-cm point.

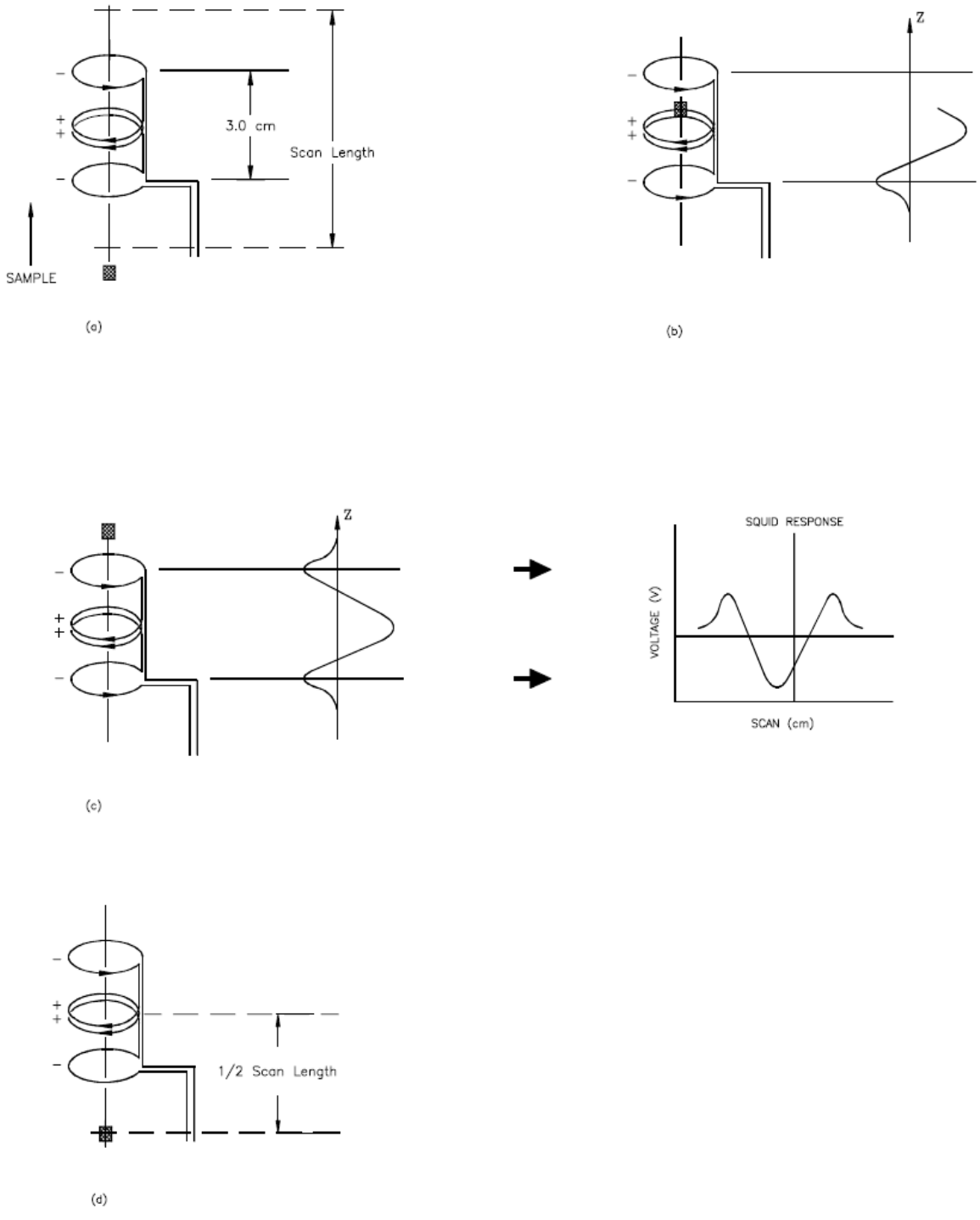

Fig 2.3.1.5. DC Centering Measurement and Measured SQUID Voltage Response [MPMS multiVu user's manual, 2004]

Figure 2.3.1.5(a) illustrates the sample moving upward through the SQUID pickup coils. Figure 2.3.1.5(b) illustrates MPMS MultiVu measuring the SQUID response while the sample moves through the coils. Figure 2.3.1.5(c) plots the SQUID response against the scan length; the output in figure 2.3.1.5(c) indicates that the sample is too high and must be lowered. Figure 2.3.1.5(d) illustrates a centered sample. In figure 2.3.1.5(d), the scan begins one-half scan length below the center coils. The SQUID magnetometer is equipped with horizontal sample rotator that can rotate the sample about the measurement axis, and with both a parallel and a perpendicular detection system [MPMS Application Note, 2000]. The shape of the plot is a function of the geometry of the pickup coils. The coils are wound in a second-derivative configuration in which the single-turn, positively charged upper and lower coils are counterwound with respect to the two-turn, negatively charged center coil. In the plot, the large, middle curve is the reading from the two center coils. The smaller first and third curves are the readings from the first and fourth coils, respectively.

It is noted that, for a precise determination of the magnetic moment perpendicular to the applied field, it should not be too small compared to the

magnetic moment parallel to the applied field [Miller, 1996, MPMS Application Note, 2000], because a magnetization component parallel to the applied field interferes with the response of the perpendicular pickup-coils. However, in the study, the measurement was performed using a SQUID magnetometer that the magnetic moment parallel to the applied field could only be measured.

2.3.2 Vibrating Sample Magnetometer (VSM)

Temperature over room temperature magnetization measurements were performed with Foner-type [Foner, 1959] vibrating sample magnetometer (VSM) (Toei) in the magnetic field of 1 T using an electromagnet. The schematic diagram is shown in the Fig. 2.3.2.1. The sample was vibrated in the active region of a set of pick-up coils. The ‘active region’ is the space in which the sensitivity of the coil system varies slowly with the sample position, making it sensitive to the exact location of the sample. The operating frequency was 80 Hz. The system was calibrated using a standard nickel sample at room temperature in order to derive the relationship between the magnetization and the detected signal. Usually 10 mg sample is

enough for the magnetization measurement. The saturation magnetization of nickel was taken to as 54.39 $JT^{-1}Kg^{-1}$ (emu/g) [National Astronomical Observatory, 1990] at 293 K.

The temperature dependence of magnetization was measured with the same Foner-type VSM using an electromagnet (Toei VSM-3-15 model. In the system, the maximum of the applied field was 1 T and the operating temperature was from 300 to 770 K. The operating frequency was 80 Hz. The system was calibrated at room temperature. The furnace consists of an electrically-heated outer tube assembly with efficient vacuum and reflective thermal insulation.

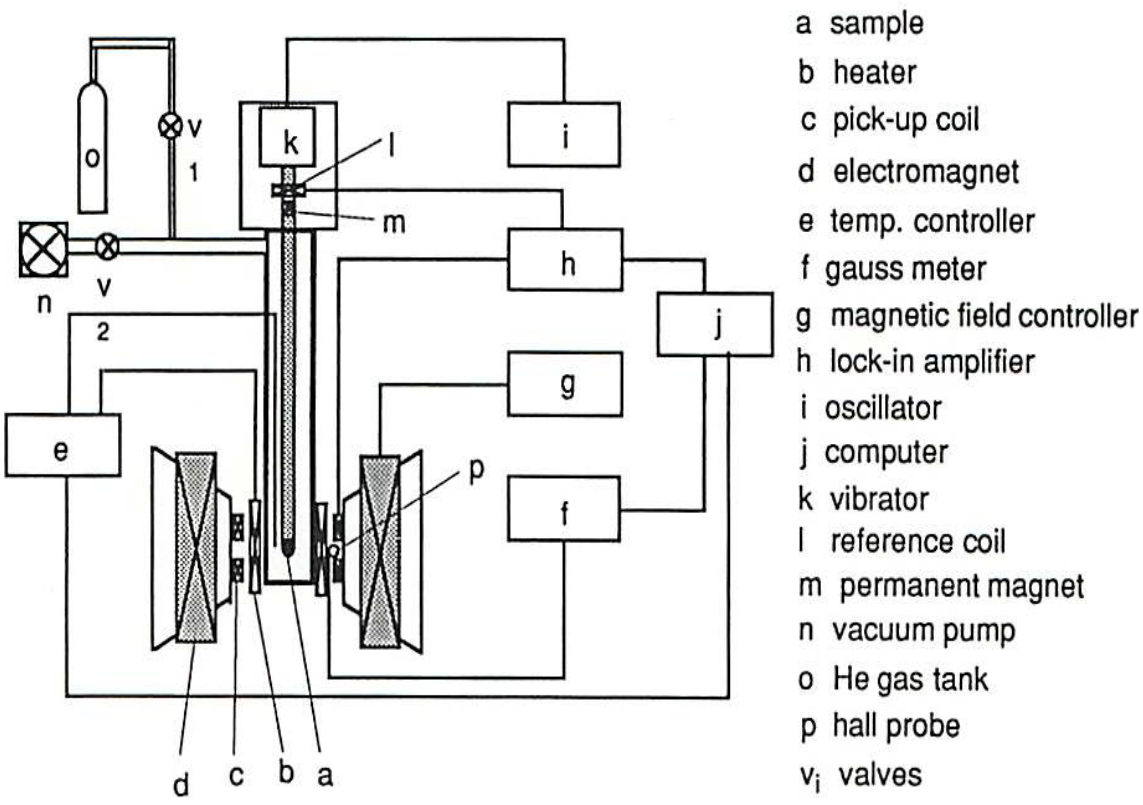

Fig 2.3.2.1. Schematic diagram of the vibrating sample magnetometer (VSM) with the electromagnet [Koyama, 1997]

2.4 Differential Scanning Calorimetry

Differential scanning calorimetry (NETZSCH DSC 200 F3 Maia) was carried out under an N_2 atmosphere in a temperature range of 120-750 K. The heating and cooling rates of the DSC measurements were 10 K/min. $Mn_{1.9}Fe_{0.1}Sb_{0.9}Sn_{0.1}$ was placed inside a crucible which is then placed inside

the measurement cell (furnace) of the DSC system along with a reference pan which is normally empty. By applying a controlled temperature program (iso- thermal, heating or cooling at constant rates), caloric changes can be characterized. The heating wires of the furnace surround the entire sensor plate. They are arranged in such a way that no temperature gradients occur in or above the sensor disk. This arrangement is the basis for a highly homogeneous heat flow to the sample and reference pans from all sides and therefore also for a highly stable baseline and an excellent signal-to-noise ratio. Protective and purge gas inlets are, of course, standard features of the unit.

Fig.2.4.1 shows the schematic diagram of DSC 200 F3 Maia. For improved cooling times and sub- ambient temperature tests, various cooling options such as forced air, intracooler or liquid nitrogen cooling systems, a versatile gas switching and flow control system are available. The DSC 200 *F3 Maia* runs under a 32-bit Windows operating system which includes everything you need to carry out a measurement and evaluate the resulting data.

The DSC 200 F3 Maia has the following features: determination of onset, peak, inflection and end temperatures, automatic peak search, transformation enthalpies: analysis of peak areas (enthalpies) with selectable baseline and partial peak area analysis and consideration of mass changes, comprehensive glass transition analysis, automatic baseline correction, degree of crystallinity, specific heat determination. The DSC correction allows evaluation of exo- and endo- thermal effects under consideration of system time constants and thermal resistances. The technical specifications are listed in Table 2.4.1.

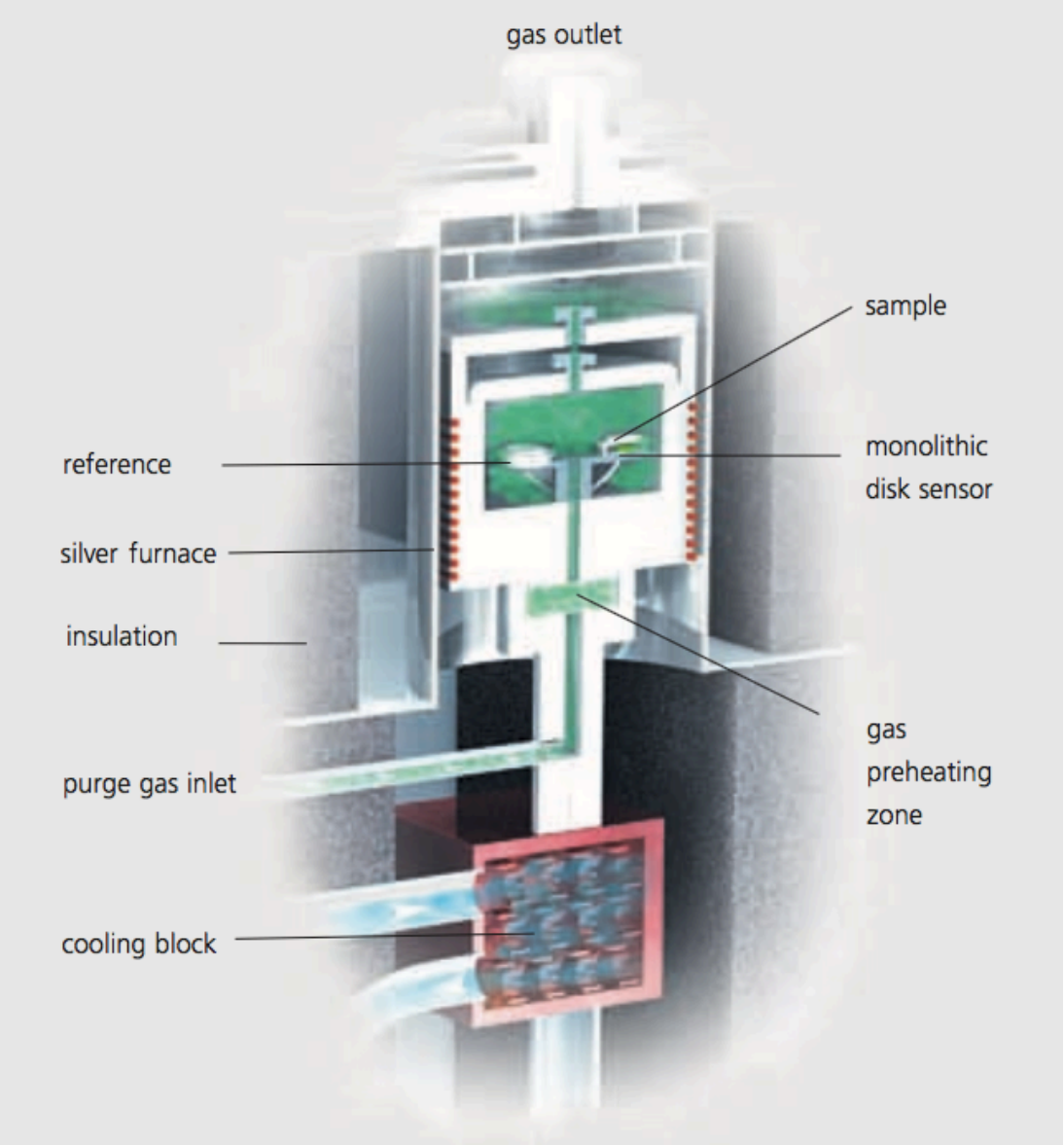

Fig.2.4.2 Schematic diagram of DSC 200 F3 Maia (NETZSCH catalog)

Table 2.4.1. Technical specifications of NETZSCH DSC 200 F3 Maia (NETZSCH catalog).

Temperature Range:	-103 K to 873 K
Heating rates:	0.001K/min to 100 K/min
Cooling rates:	0.001K/min to 100 K/min (depending on temp.)
Sensor:	Heat flux system
Measurement range:	0 mW to +/- 600 mW
Temperature accuracy:	0.1 K
Enthalpy accuracy:	< 1%
Cooling options:	Forced air, LN_2, Intracooler
Atmospheres:	oxid., inert (static, dynamic)

Chapter 3

Results

3.1 Magnetic and Structural Properties of $Mn_{1.9}Fe_{0.1}Sb_{0.9}Sn_{0.1}$ under Magnetic Fields

3.1.1 Sample Characterization by XRD

Figure 3.1.1.1 shows the XRD pattern of $Mn_{1.9}Fe_{0.1}Sb_{0.9}Sn_{0.1}$ at room temperature. The sample was confirmed to be almost a single phase with the Cu_2Sb-type structure for the $Mn_{1.9}Fe_{0.1}Sb_{0.9}Sn_{0.1}$ powder where a = 0.4068 nm and c = 0.6549 nm. The weak reflections marked by X in Figure 3.1.1.1 are attributed to a small amount of second phase, identified as MnSb precipitate, which derived to the ferromagnetic MnSb phase [Wakamori et al. 2017, Caron et al., 2013]. It is reported that T_C of MnSb alloys is 550-586 K [Caron et al., 2013, Tsujimura et al., 1962, Chikazumi, 2009]. Therefore, as described below, the influence of the MnSb impurity phase on the magnetic phase transition in $10 \leq T \leq 360$ K is negligible. It was confirmed that

$Mn_{1.95}Fe_{0.05}Sb_{0.95}Sn_{0.05}$ and $Mn_{1.85}Fe_{0.15}Sb_{0.9}Sn_{0.1}$ were also almost a single phase with the Cu_2Sb-type structure.

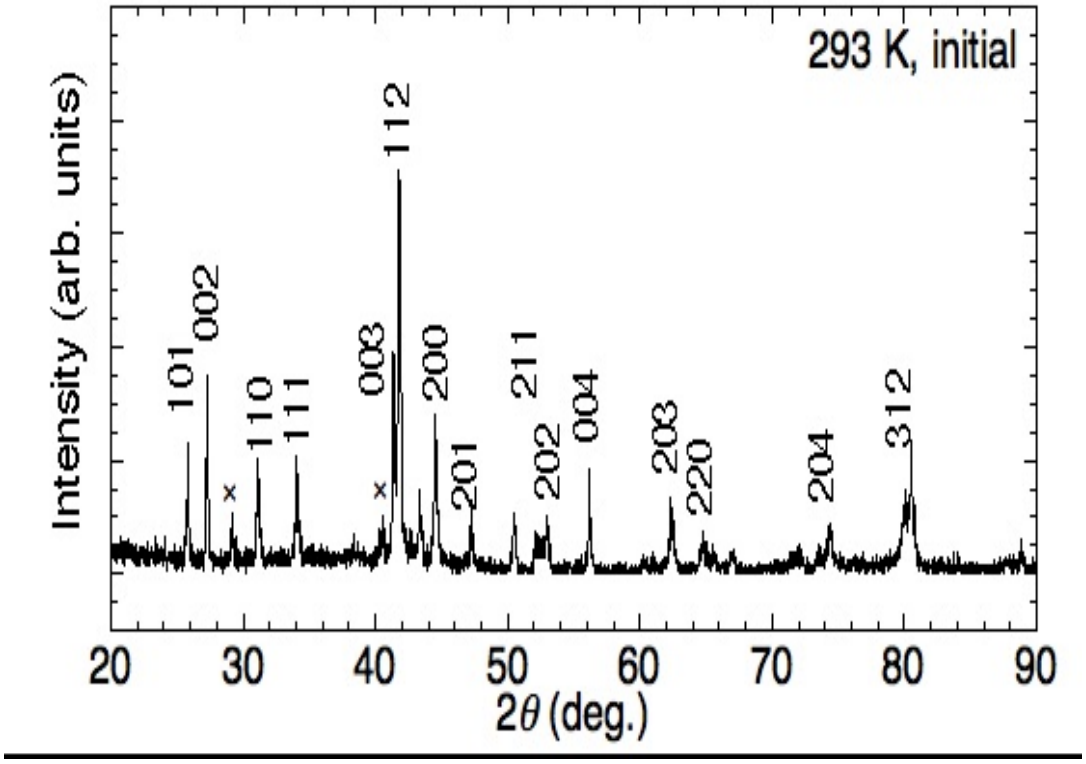

Fig.3.1.1.1 XRD pattern $Mn_{1.9}Fe_{0.1}Sb_{0.9}Sn_{0.1}$ of in a zero field at a room temperature [Nwodo et al, 2018]

3.1.2 Magnetic Properties

Figure 3.1.2.1 (a) shows the temperature dependence of the

magnetization (*M-T*) of $Mn_{1.9}Fe_{0.1}Sb_{0.9}Sn_{0.1}$ for $\mu_0 H$ = 0.1 and 5 T. The reported *M-T* data of $Mn_2Sb_{0.9}Sn_{0.1}$ [Koyama, 2015] are indicated in Fig. 3.1.2.1 (b) to compare the results of $Mn_{1.9}Fe_{0.1}Sb_{0.9}Sn_{0.1}$ with $Mn_2Sb_{0.9}Sn_{0.1}$. Here, the measurements were made in field cooling (FC) and field-cooled warming (FCW). The inset of Fig. 3.1.2.1 (a) shows the *M-T* curves of $Mn_{1.9}Fe_{0.1}Sb_{0.9}Sn_{0.1}$ for $\mu_0 H$ = 5 mT. [Nwodo et al., 2018].

As seen in Fig. 3.1.2.1 (b), $Mn_2Sb_{0.9}Sn_{0.1}$ for $\mu_0 H$ = 0.1 T exhibited a first-order AFM-FRI transition for $120 \leq T \leq 230$ K with a thermal hysteresis. Furthermore, a cusp of the *M-T* curve for $\mu_0 H$ = 0.1 T was observed in the vicinity of 225 K, which also had a thermal hysteresis originated from the spin reorientation (SR) in the FRI phase [Bartashevich et al., 2002, Val'ko et al., 2007, Koyama et al., 2013, Matsumoto et al., 2014, Matsumoto et al., 2016, Kanomata et al., 1991]. The SR temperatures for the FC and FCW processes were determined to be T_{SR1} = 218 K and T_{SR2} = 227 K, respectively. When a field of $\mu_0 H$ = 5 T was applied, the FRI-AFM transition temperature decreased for $80 \leq T \leq 225$ K, and the cusp due to the SR disappeared. The T_C of $Mn_2Sb_{0.9}Sn_{0.1}$ was reported to be 530 K [Koyama, 2013].

As seen in Fig. 3.1.2.1 (a), the magnetic properties of Fe substituted

compound $Mn_{1.9}Fe_{0.1}Sb_{0.9}Sn_{0.1}$ were different from those of $Mn_2Sb_{0.9}Sn_{0.1}$. The AFM state was not clearly observed in $Mn_{1.9}Fe_{0.1}Sb_{0.9}Sn_{0.1}$. In $Mn_{1.9}Fe_{0.1}Sb_{0.9}Sn_{0.1}$, a thermal hysteresis was observed for $70 \leq T \leq 230$ K in $\mu_0 H = 0.1$ T. This hysteresis did not disappear even for $\mu_0 H = 5$ T. According to the previous reports [Kanomata and Ido, 1984 Blaauw et al., 1977], the substitution of Fe for Mn in Mn_2Sb system did not result in the FRI-AFM FOMT. Considering these results, it is supposed that the substitution of Fe for Mn in $Mn_2Sb_{0.9}Sn_{0.1}$ suppresses the AFM interaction and induces the FRI interaction. However, the values of the magnetization at 10 K were slightly smaller than those around 100 K. This result suggests that there was a small fraction of the AFM phase in the FRI phase.

It was confirmed that $Mn_{1.9}Fe_{0.1}Sb_{0.9}Sn_{0.1}$ exhibited the FOMT from a FRI to a PM-like (IM) state with a hysteresis of about 5 K in the vicinity of 310 K (= T_t: the inflection point of the *M-T* curve), as shown in Fig. 3.1.2.1 (a). The inset in Fig. 3.1.2.1 (a) also indicated that the FOMT with the small hysteresis was observed for $\mu_0 H = 5$ mT [Nwodo et al., 2018]. Furthermore, small cusps were observed for the ZFCW (zero-field-cooling warming) and FC processes just below the FOMT, which is similar to Hopkinson effect

[Chikazumi, 2009].

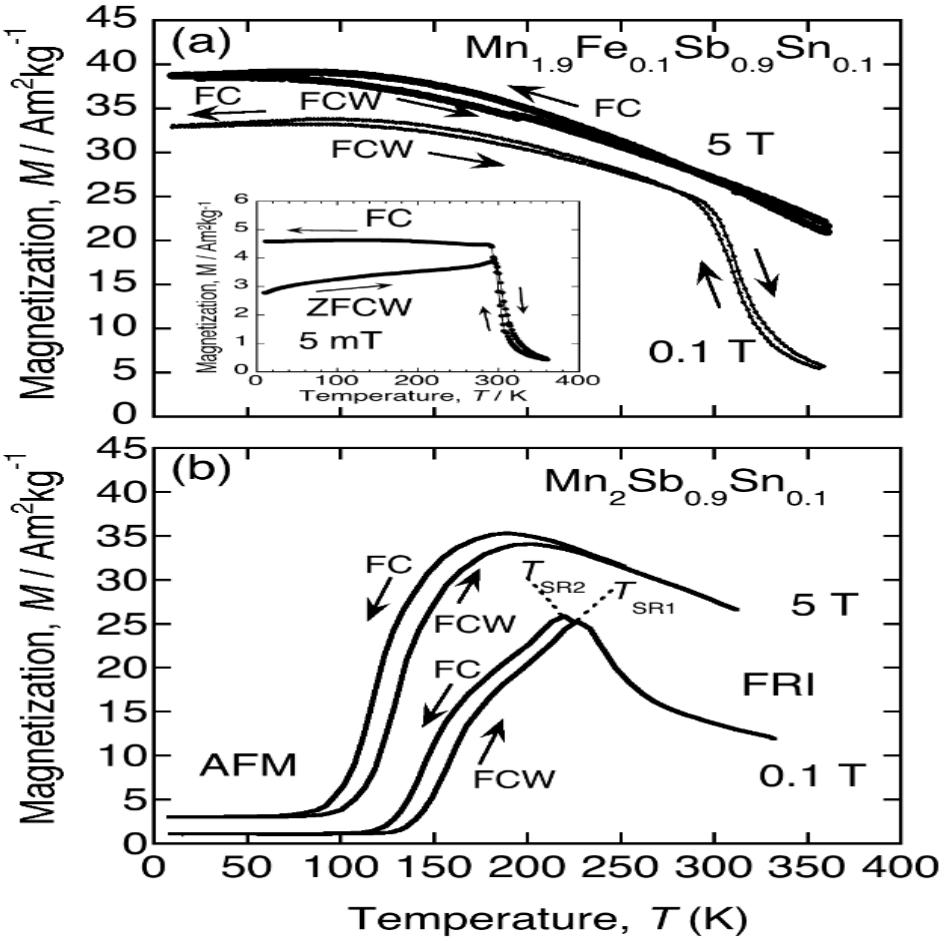

Fig. 3.1.2.1. Temperature dependence of the magnetization of $Mn_{1.9}Fe_{0.1}Sb_{0.9}Sn_{0.1}$ in $10 \leq T \leq 360$ K under $\mu_0 H = 0.1$ and 5 T (a), and $Mn_2Sb_{0.9}Sn_{0.1}$ (b) [Koyama, et al., 2013]. The measurements were made in field cooling (FC) and field cooled warming (FCW). The arrows indicate the measurement process. T_{SR1} and T_{SR2} indicates the spin-reorientation temperatures in the ferrimagnetic phase (FRI). The inset shows the M-T data of $Mn_{1.9}Fe_{0.1}Sb_{0.9}Sn_{0.1}$ for 5 mT [Nwodo et al., 2018].

The detailed *M*-*T* data of $Mn_{1.9}Fe_{0.9}Sb_{0.9}Sn_{0.1}$ under $\mu_0 H = 0.05$, 0.1 0.2, 0.4 and 1 T for $260 \leq T \leq 360$ K are shown in Fig. 3.1.2.2. When the magnetic field increased up to $\mu_0 H = 0.4$ T, T_t between the FRI and IM state increased. For $\mu_0 H = 1$ T, the IM state almost disappeared, and the compound seems to be FRI state for $T \leq 360$ K. Similar FOMT was observed for other $Mn_{2-x}Fe_xSb_{1-y}Sn_y$ ($0.05 \leq x \leq 0.15$, $0.05 \leq y \leq 0.1$), which will be reported in sec. 3.2 and 3.3.

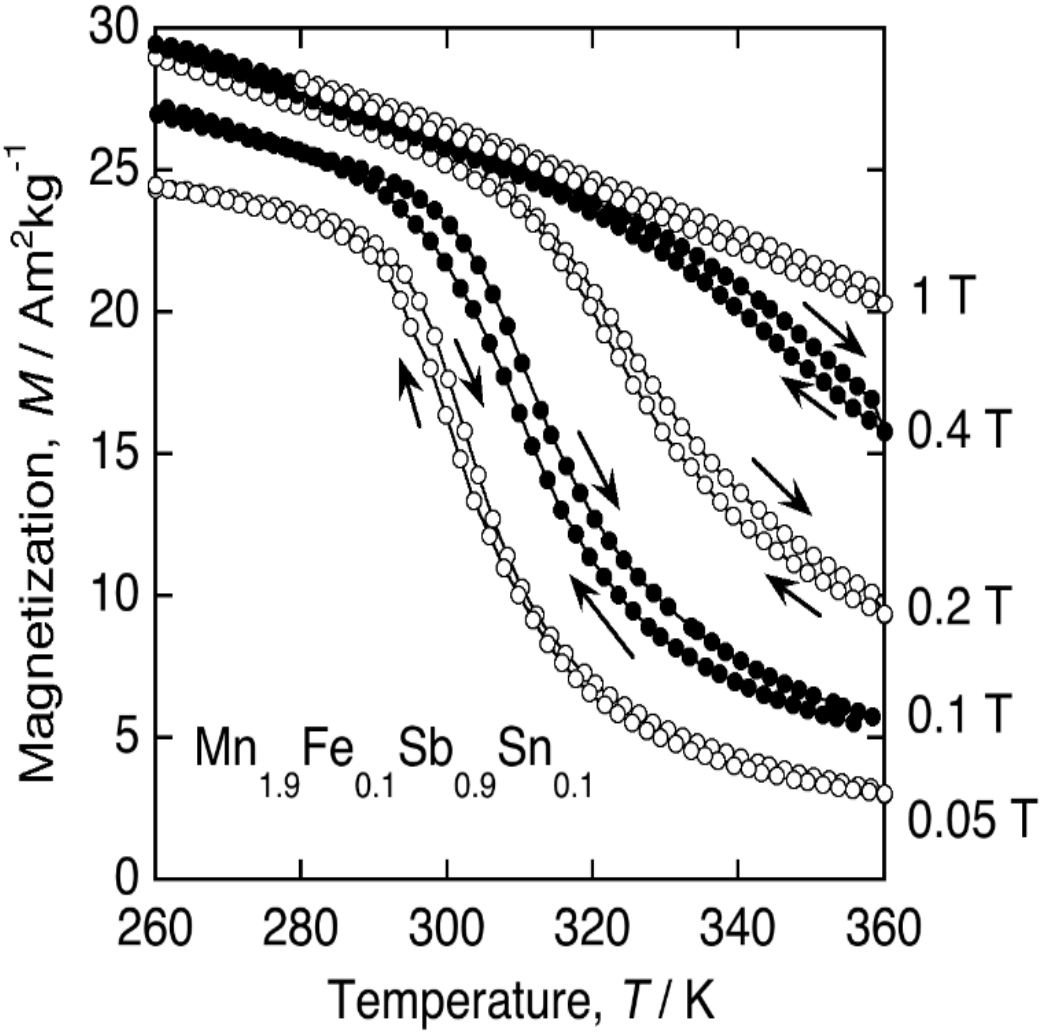

Fig. 3.1.2.2. Temperature dependence of the magnetization of $Mn_{1.9}Fe_{0.1}Sb_{0.9}Sn_{0.1}$ in $260 \leq T \leq 360$ K for 0.05, 0.1, 0.2, 0.4 and 1 T. The arrows indicate the measurement process [Nwodo et al., 2018].

Figure 3.1.2.3 shows the magnetization curves of $Mn_{1.9}Fe_{0.1}Sb_{0.9}Sn_{0.1}$ at several temperatures for $10 \leq T \leq 360$ K. The inset of Fig. 3.1.2.3 shows the enlarged view of the magnetization (*M-H*) curves for $\mu_0 H < 0.6$ T at several temperatures for $290 \leq T \leq 360$ K. These *M-H* curves at $T \geq T_t$ became saturated, which is different from the usual PM *M-H* curve over second-order magnetic transition temperature and the usual metamagnetic *M-H* curve over FOMT temperature.

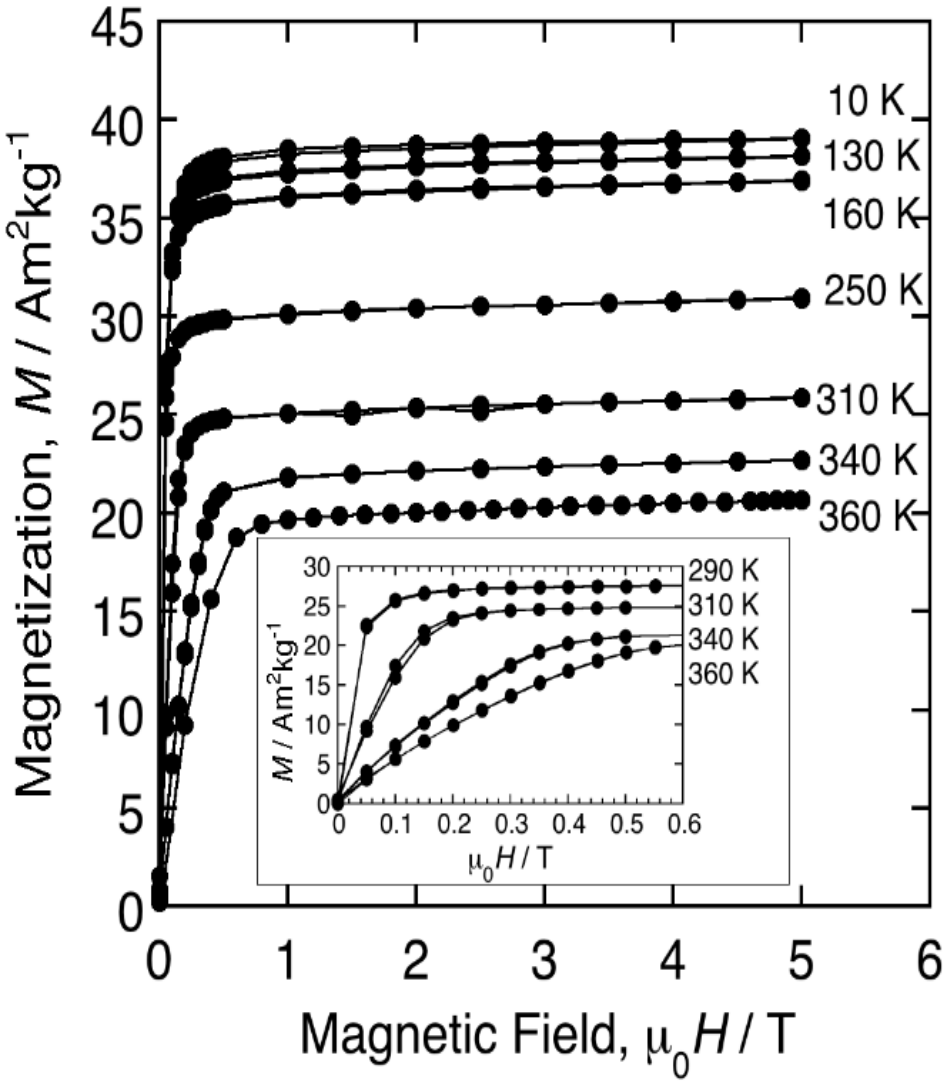

Fig. 3.1.2.3. *Magnetization curves of* $Mn_{1.9}Fe_{0.1}Sb_{0.9}Sn_{0.1}$ *at several temperatures for 10-360 K. The inset shows the enlarged view of the magnetization curves for* $\mu_0 H < 0.6$ *T for 290-360 K [Nwodo et al., 2018].*

Figure 3.1.2.4 gives the enlarged view of the magnetization curves of $Mn_{1.9}Fe_{0.1}Sb_{0.9}Sn_{0.1}$ at 10 K (a), 40 K (b), 70 K (c), 100-160 K (d) and 250 K (e). The magnetization process with the hysteresis was observed in $10 \leq T < 160$ K. This temperature range is consistent with the results of the *M*-*T* measurements, which exhibits the thermal hysteresis (see Fig. 3.1.2.1 (a)). For T = 10 K, the saturation magnetization was determined to be 39.1 Am^2/kg at $\mu_0 H$ = 5 T, which corresponds to 1.63 μ_B/f.u.. This value was slightly smaller than that of 39.2 Am^2/kg for T = 40 K and 70 K at $\mu_0 H$ = 5 T. This result is also consistent with that of the *M*-*T* data.

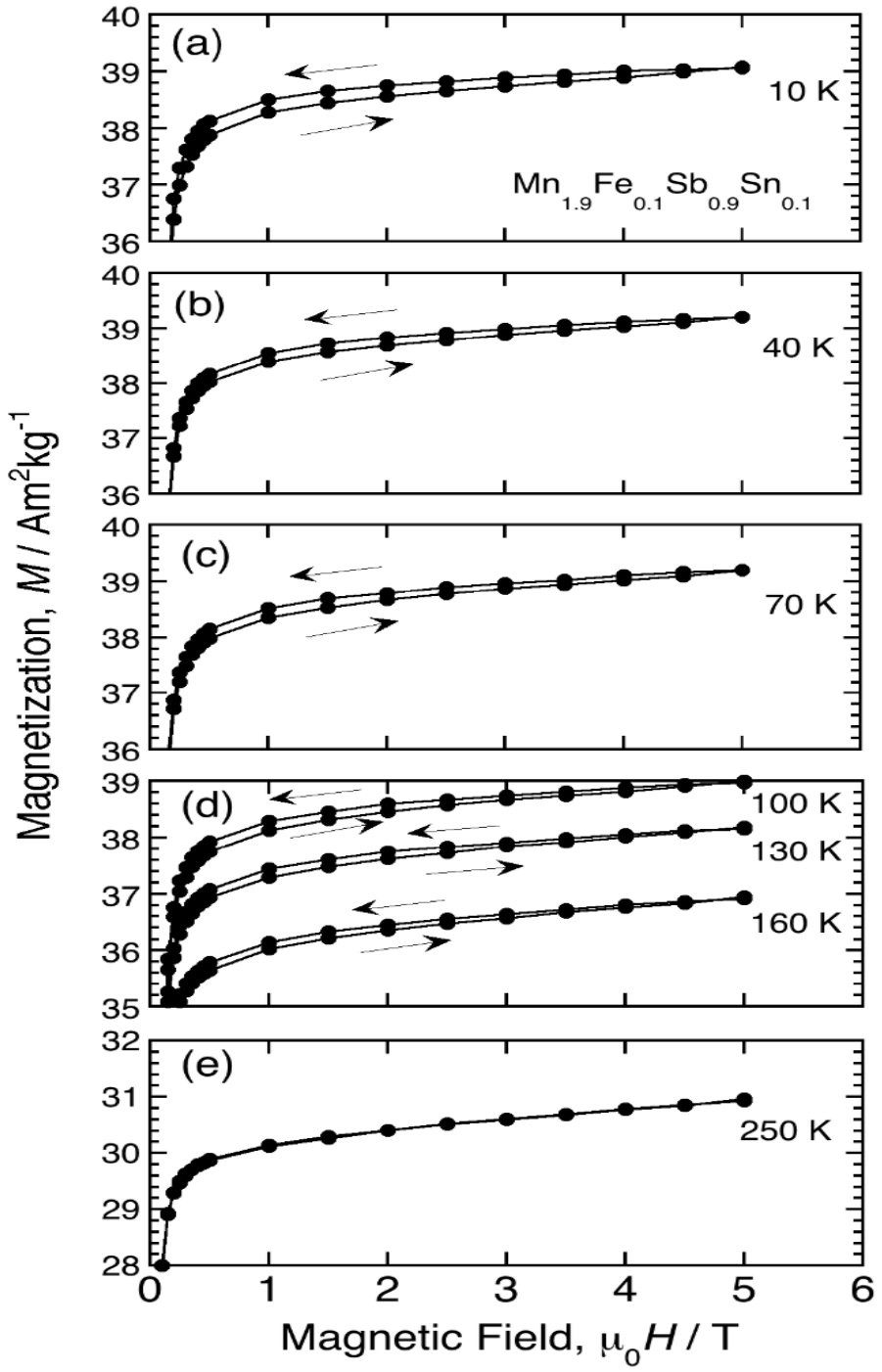

Fig. 3.1.2.4. Magnetization curves of $Mn_{1.9}Fe_{0.1}Sb_{0.9}Sn_{0.1}$ at 10 K (a), 40 K (b), 70 K (c), 100-160 K (d) and 250 K (e), which are enlarged view of Fig. 5 [Nwodo et al., 2018].

3.1.3 Structural Properties

Figure 3.1.3.1 shows the typical XRD profiles of $Mn_{1.9}Fe_{0.1}Sb_{0.9}Sn_{0.1}$ for the 004 (a) and 220 (b) peaks in a zero field cooling process at several temperatures. Here, the diffractions by $K\alpha_1$ and $K\alpha_2$ radiations were observed. The both diffraction peaks shifted to higher 2θ angle side with decreasing temperature, indicating the lattice contraction. According to the XRD data of $Mn_{1.8}Co_{0.2}Sb$ [Orihashi et al., 2013] and $Mn_2Sb_{0.95}Ge_{0.05}$ [Orihashi et al., 2013, Wakamori et al., 2016], the lattice parameter a of the AFM phase is larger than that of the FRI phase, and the lattice parameter c of the AFM phase is smaller than that of the FRI phase. Therefore, when the structural transformation from the FRI to AFM phase occurs, we observe two diffraction peaks due to the FRI and AFM phases [Orihashi et al., 2013, Wakamori et al., 2016]. As seen in Fig. 3.1.3.1, however, any drastic change of the XRD profile was not observed. The diffraction peaks of the FRI phase were only confirmed, and any peak of the AFM phase or the two-phase coexistence of the AFM and FRI phases were not observed in $10 \leq T \leq 325$ K. That is, any structural transformation did not occur in $Mn_{1.9}Fe_{0.1}Sb_{0.9}Sn_{0.1}$ in this temperature range.

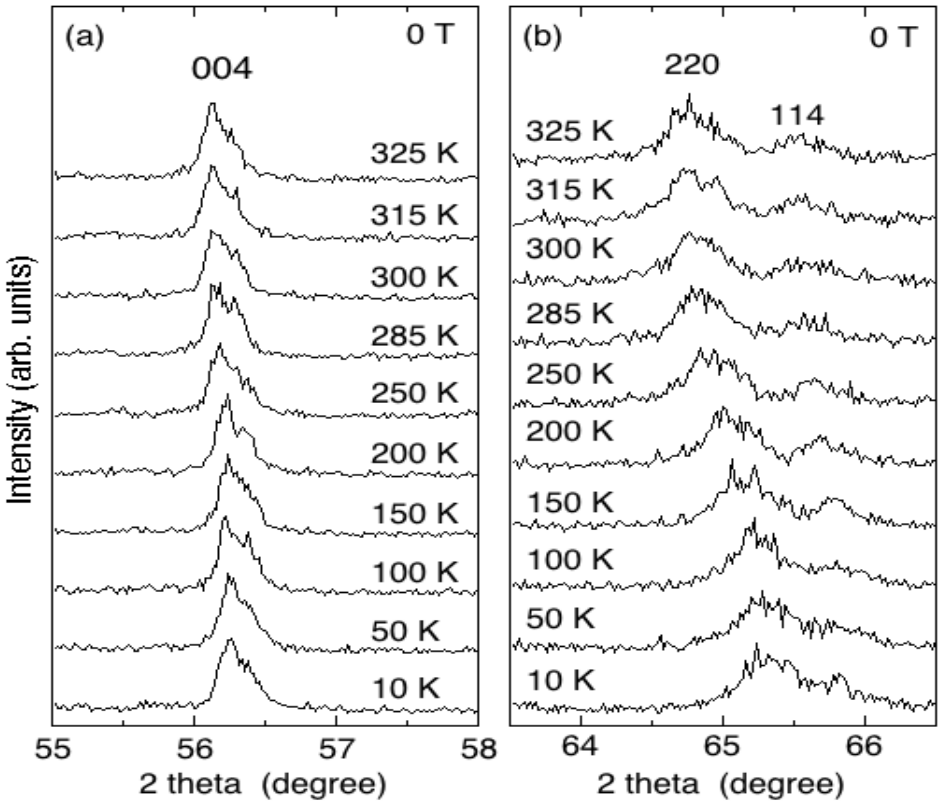

Fig. 3.1.3.1. *X-ray powder diffraction profiles of the 004 reflection (a) and the 220 reflection (b) in* $\mu_0 H = 0$ *T at various temperatures for cooling process [Nwodo et al., 2018].*

Figure 3.1.3.2 shows the temperature dependence of *a*, *c* and the cell volume *V*. Here, *a* and *c* were deduced from the 2θ position of the 220 and 004 peaks, respectively. In this figure, the open circles indicate the data for

cooling and heating process under $\mu_0 H = 0$ T. The parameters a, c and V of 285 K were estimated to be 0.4068 nm, 0.6550 nm and 0.1084 nm^3, respectively. Any anomaly of the a-T and c-T curves was not observed in the vicinity of T_t. Only normal thermal contractions (thermal expansion) of a, c and V were observed. The linear thermal expansion coefficient of a and c were estimated to be $\alpha(a) = 13 \times 10^{-6}$ K^{-1} and $\alpha(c) = 13 \times 10^{-6}$ K^{-1} for $275 \leq T \leq 325$ K, respectively. These values are consistent with $\alpha(c)$ of $Mn_{1.8}Co_{0.2}Sb$ [Orihashi et al., 2013].

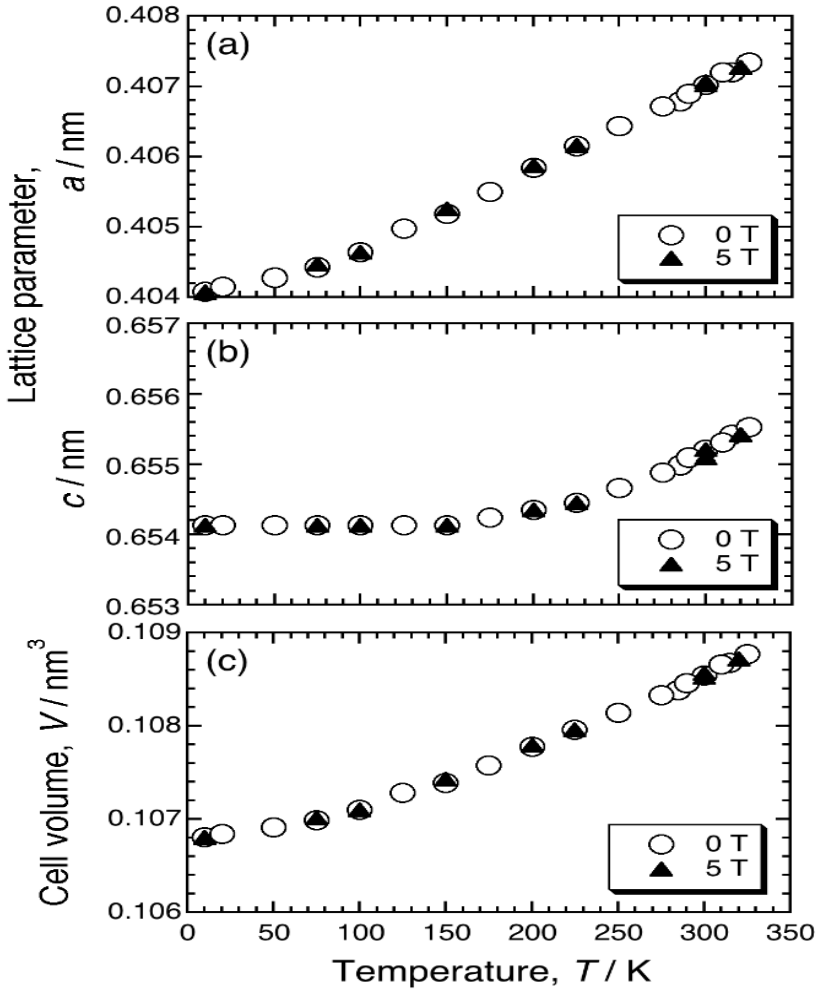

Fig. 3.1.3.2. *Temperature dependence of the lattice parameters a, c and the cell volume V of* $Mn_{1.9}Fe_{0.1}Sb_{0.9}Sn_{0.1}$. *The open circles and closed triangles indicate the data for 0 T and 5 T [Nwodo et al., 2018].*

Figure 3.1.3.3 indicates the XRD profiles of $Mn_{1.9}Fe_{0.1}Sb_{0.9}Sn_{0.1}$ for the 004 (a) and 220 (b) peaks in a field cooling process under $\mu_0 H = 5$ T at several temperatures. Here, the diffractions by $K\alpha_1$ and $K\alpha_2$ radiations were

observed. The temperature dependence of a, c and V under a magnetic field of 5 T are also shown by the solid triangles in Fig. 3.1.3.2. Any magnetic field effect on the lattice parameters was not observed.

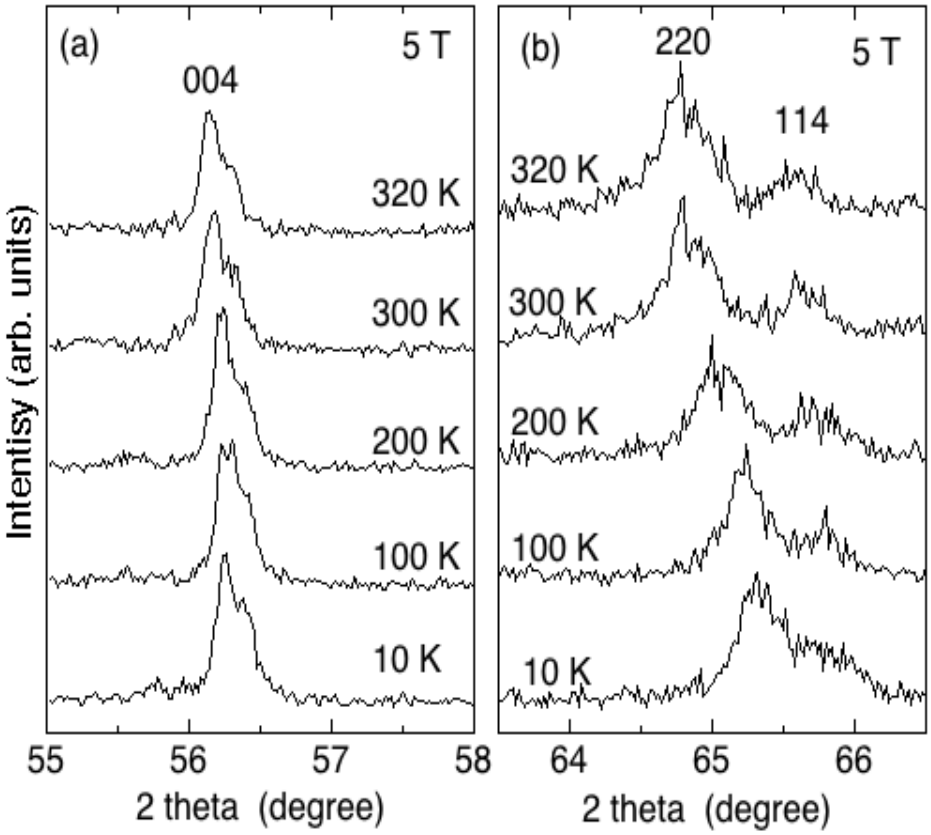

Fig. 3.1.3.3 X-ray powder diffraction profiles of the 004 reflection (a) and the 220 reflection (b) in 5 T at various temperatures for cooling process [Nwodo et al., 2018].

3.2 Magnetic Properties of $Mn_{1.95}Fe_{0.05}Sb_{0.95}Sn_{0.05}$ under Magnetic Fields

3.2.1 Magnetic Properties

The temperature dependence of the magnetization was measured for the sample in $10 \leq T \leq 360$ K for $\mu_0 H = 0.1$ T and presented in Figure 3.2.1.1 as typical *M*-*T* data. Here, the measurements were made in field cooling (FC) and field-cooled warming (FCW). As shown in Fig. 3.2.1.1, the data of $Mn_{1.95}Fe_{0.05}Sb_{0.95}Sn_{0.05}$ for $\mu_0 H = 0.1$ T indicate that a first-order phase transition from a FRI to an PM-like (IM) phase occurs in the vicinity of 320 K (= *T*t) with a thermal hysteresis of approximately 5 K. This result is consistent with that of $Mn_{1.9}Fe_{0.1}Sb_{0.9}Sn_{0.1}$ [Nwodo, et al., 2018].

Studies of the magnetic and the electrical properties of $Mn_2Sb_{1-x}Ge_x$ ($0.05 \leq x \leq 0.2$) and $Mn_2Sb_{1-x}Sn_x$ ($0.08 \leq x \leq 0.15$) in magnetic fields up to 16 T in the 4.2–600 K have been reported by Koyama et al. (2013). $Mn_2Sb_{0.95}Ge_{0.05}$ and $Mn_2Sb_{0.9}Sn_{0.1}$ showed a first-order magnetic transition from a ferrimagnetic (FRI) to an antiferromagnetic (AFM) phase in the

vicinity of T_t = 172 K and 190 K, respectively, with decreasing temperature in a zero-magnetic field. However, in the $Mn_{1.95}Fe_{0.05}Sb_{0.95}Sn_{0.05}$, any first order magnetic transition from the FRI-PM phase was not observed, such as Fig 3.2.1.1.

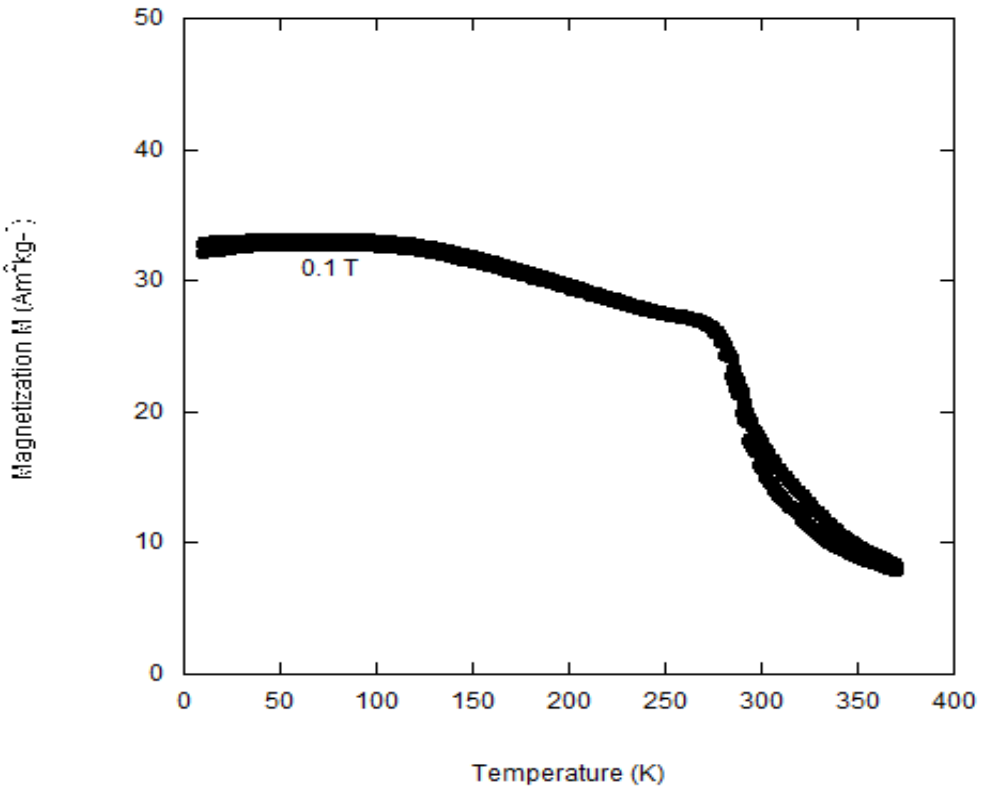

Fig. 3.2.1.1 Temperature dependence of the magnetic moment of $Mn_{1.95}Fe_{0.05}Sb_{0.95}Sn_{0.05}$ in $10 \leq T \leq 360$ K under $\mu_0 H$ =0. 1 T and the measurements were made in field cooling (FC) and field cooled warming (FCW). The arrows indicate the measurement process.

The difference with the magnetic property of Fe substituted compound $Mn_{1.95}Fe_{0.05}Sb_{0.95}Sn_{0.05}$ and that of the reported $Mn_2Sb_{0.9}Sn_{0.1}$ can be attributed to the substitution of Fe for Mn in $Mn_2Sb_{0.9}Sn_{0.1}$, resulting in suppression of the AFM state and induced the FRI interaction. Here I report on $Mn_{1.95}Fe_{0.05}Sb_{0.95}Sn_{0.05}$ compound undergoing a first order magnetic transition from FRI-PM-like (IM) with thermal hysteresis in the vicinity of 320 K but did not show a FOMT from FRI to AFM at low temperature for the first time. The magnetic moment under a low magnetic field of 0.1 T decreases with decreasing temperature and exhibits a sharp maximum just below the Curie-like temperature (transition temperature (T_t)) with a thermal hysteresis. This phenomenon is called the Hopkinson effect. This result indicates that the observed transition is a FRI-PM-like. In addition, the magnetic moment slightly decreases with decreasing temperature for $T \leq 100$ K. The report of $Mn_2Sb_{0.9}Sn_{0.1}$ shows an AFM state at lower temperature. Considering this report, the present result indicates that there was a small fraction of the AFM state in the FRI phase for $T \leq 100$ K

Magnetization measurements for $Mn_{1.95}Fe_{0.05}Sb_{0.95}Sn_{0.05}$ in $220 \leq T \leq 390$ K for $\mu_0 H = 0.05$, 0.1, 0.5 and 5 T (see Figure 3.2.1.2) reveals first-order phase transitions FRI-PM-like transition with very low thermal hysteresis (less than 1 K in vicinity of 320 K (T_t) for this compositions). For 0.05 T, the transition temperature (T_t) was observed at 290 K. With increasing magnetic field, the T_t also increases. However, over the magnetic field of 0.05 T, the T_t was not clearly observed because the magnetic field induced magnetic moment in the PM phase. It was noted that thermal hysteresis was observed over 0.5 T.

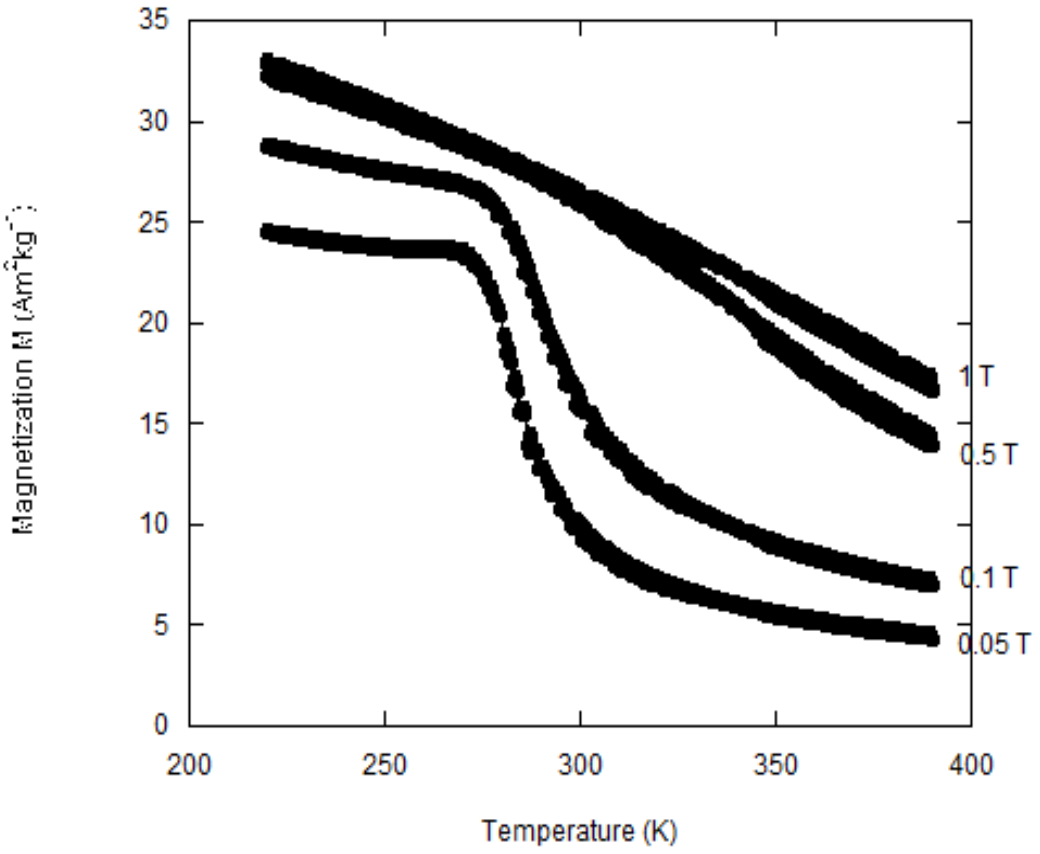

Fig. 3.2.1.2. Temperature dependence of the magnetic moment of $Mn_{1.95}Fe_{0.05}Sb_{0.95}Sn_{0.05}$ *in* $260 \leq T \leq 360$ *K for 1, 0.5, 5, and 0.1 and 0.05 T.*

Fig. 3.2.1.3 shows the magnetic moment of $Mn_{1.95}Fe_{0.05}Sb_{0.95}Sn_{0.05}$ in fields up to 5 T at T = 10-360 K measured with increasing and decreasing field strength. The magnetic moment shows a clear temperature dependence, below 360 K the magnetic moment increases with decreasing temperature.

This is mainly due to the Mn moment that increases as the temperature is lowered. The magnetization increases with increasing field and finally reaches the saturation magnetic moment in $T \leq 360$ K. For $T = 10$ K, the magnetization was almost constant in $\mu_0 H \geq 0.5$ T, the saturation magnetization was determined to be 40.2 Am^2/kg (1.52 μ_B /f.u.). In particular, *M* of the 10 K was larger than that of the 360 K due to the effect of the thermal agitation. Fig. 3.2.1.2 exhibits FRI-PM-like FOMT about 280 K in $\mu_0 H \geq 0.1$ T but applying $\mu_0 H \geq 0.5$ T in Fig 3.2.1.3, the magnetization is almost saturated, suggesting that the main phase in the magnetic field over 0.5 T was the FRI for this temperature range. The magnetic saturation effect shows the significant influence of *H*. ($\mu_0 H$), magnetic field on the thermally induced orientation. Nonlinear increment is in Fig.3.2.1.3 due to thermal agitation and the thermal effect generates fluctuation in the magnetic interaction. The spontaneous moment is obtained by extrapolating the magnetization to zero field strength. The data at 10 K, 310 K, 320 K, 360 K are 1.52, 0.96, 0.92, and 0.76 μ_B/f.u respectively.

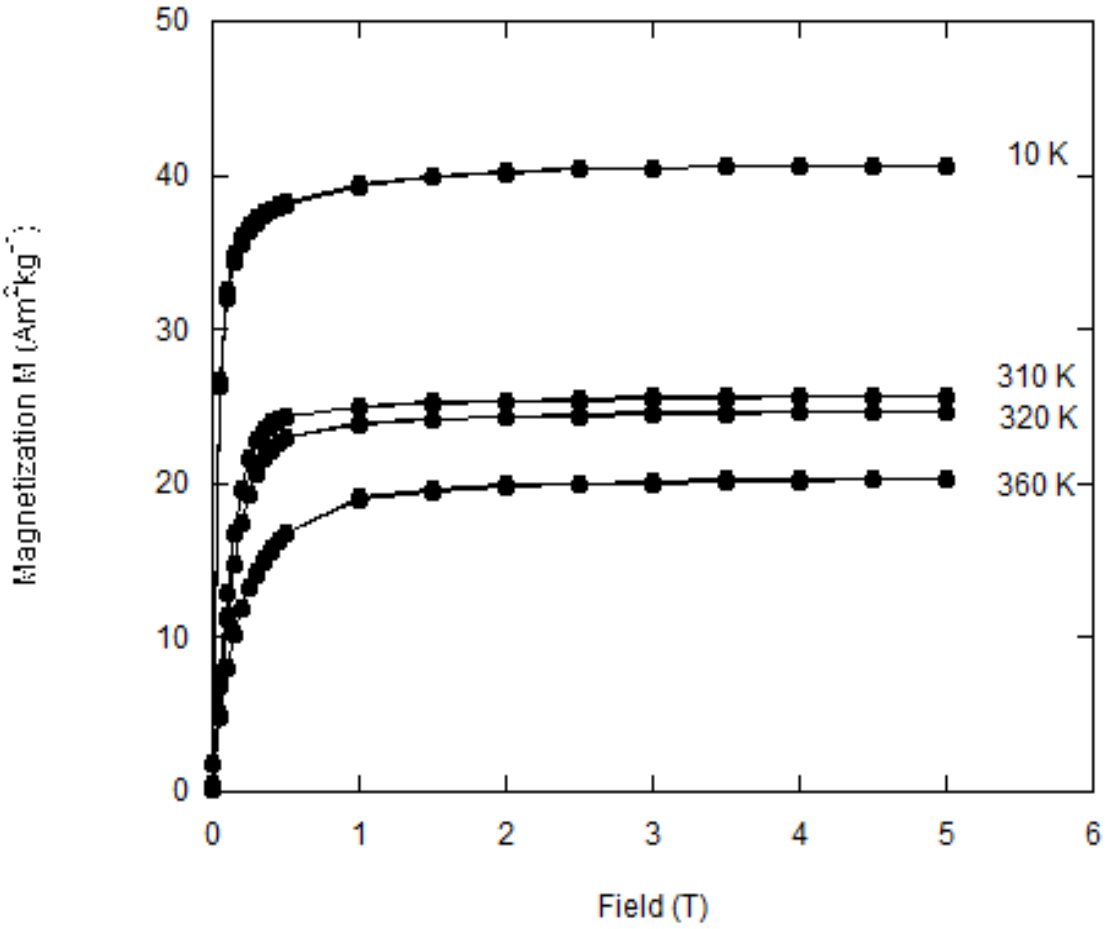

Fig. 3.2.1.3. Magnetization curves of $Mn_{1.95}Fe_{0.05}Sb_{0.95}Sn_{0.05}$ at 10, 310, 320, and 360 K.

Fig. 3.2.1.4 shows the magnetization curves of $Mn_{1.95}Fe_{0.05}Sb_{0.95}Sn_{0.05}$ for $\mu_0 H \leq 0.5$ T at 220, 250, and 280 K. show a metamagnetic behaviour. The magnetization is saturated over 0.3 T. Increasing T the saturation magnetization decreases, due to the thermal agitation. This is because

thermal agitation causes change in the orientation of the magnetization [Aharoni, 1969]. In order words, magnetic field align the magnetic moments at finite temperatures, the spin configuration is disordered by thermal agitation. In the ground state of a ferromagnet, there is no thermal or fluctuation. The magnetic moment tends to align parallel to the magnetic field under the action of thermal agitation energy, kT and the magnetization in the sample is excited thermally in unison by thermal energy kT [Chikazumi et al, 2009]. These results are in accordance with the magnetization behaviour shown in Fig. 3.2.1.2. This magnetic behaviour is very similar to that in the $Mn_{1.9}Fe_{0.1}Sb_{0.9}Sn_{0.1}$ [Nwodo, et al., 2018].

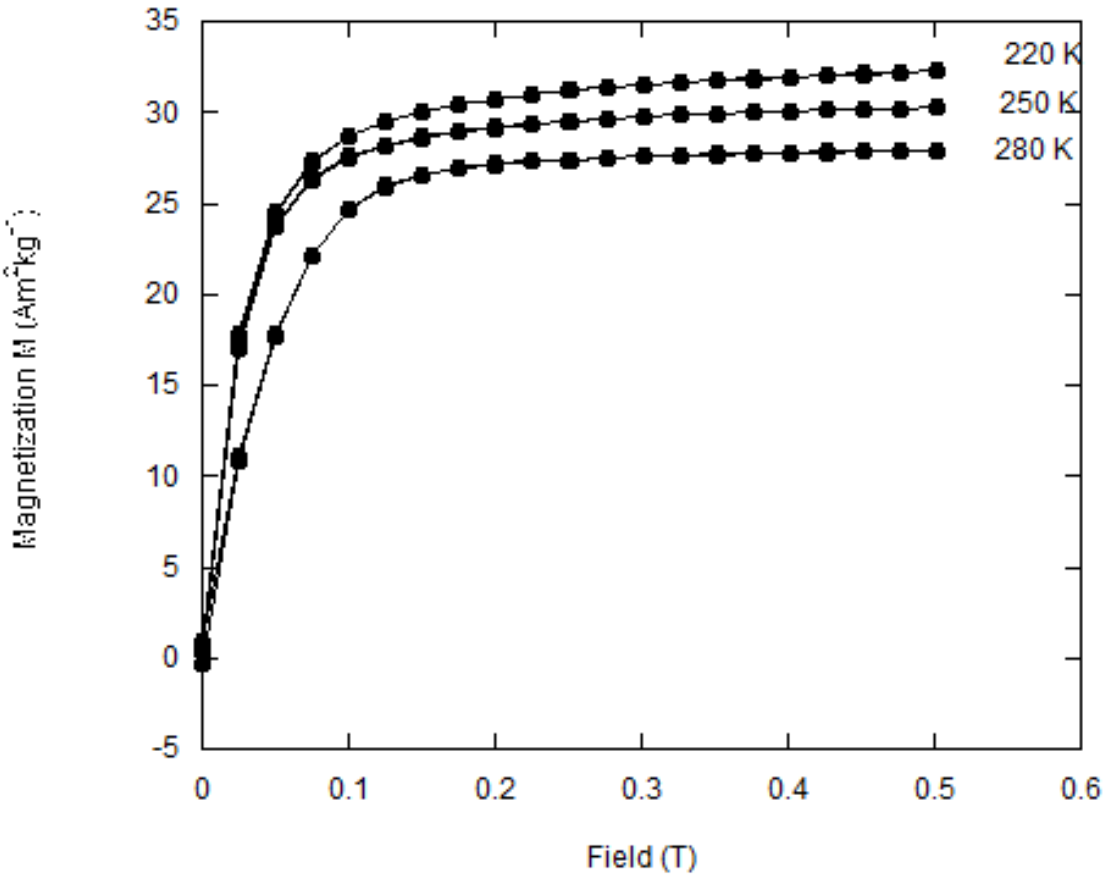

Fig. 3.2.1.4. Magnetization curves of $Mn_{1.95}Fe_{0.05}Sb_{0.95}Sn_{0.05}$ for $0 \leq \mu_0 H \leq 5$ T at 220, 250 and 280 K

In summary of this section, as seen from the *M-T* curve in Fig. 3.2.1.1, the transition from FRI to PM-like can be induced by DC fields at the 320 K. a first order transition. Moreover, the saturation magnetization of $Mn_{1.9}Fe_{0.1}Sb_{0.9}Sn_{0.1}$ is smaller than that of $Mn_{1.95}Fe_{0.05}Sb_{0.95}Sn_{0.05}$.

3.3 Magnetic Properties of $Mn_{1.85}Fe_{0.15}Sb_{0.9}Sn_{0.1}$ under Magnetic Fields

3.3.1 Magnetic Properties

Fig. 3.3.1.1. is the temperature dependence of the magnetization of $Mn_{1.85}Fe_{0.15}Sb_{0.9}Sn_{0.1}$ in $280 \leq T \leq 390$ K for $\mu_0 H = 0.05$, 0.1, 0.3, and 0.5 T. $Mn_{1.85}Fe_{0.15}Sb_{0.9}Sn_{0.1}$ exhibits a first order phase transition from a FRI to a PM-like state with a hysteresis of about 15 K in the vicinity of 380 K (= T_t) for $\mu_0 H = 0.05$ T, as shown in Fig. 3.3.1.1. For $\mu_0 H = 0.5$ T, the FOMT almost disappeared, and the compound was FRI state for $T \leq 380$ K. This result is similar to $Mn_{1.9}Fe_{0.1}Sb_{0.9}Sn_{0.1}$ but the transition temperature (T_t) of $Mn_{1.9}Fe_{0.1}Sb_{0.9}Sn_{0.1}$ is 310 K. With increasing Fe contents, the first order magnetic transition temperature increases that is, transition temperature (T_t) increases with increasing Fe content. This result indicates that Fe induces the FRI interaction.

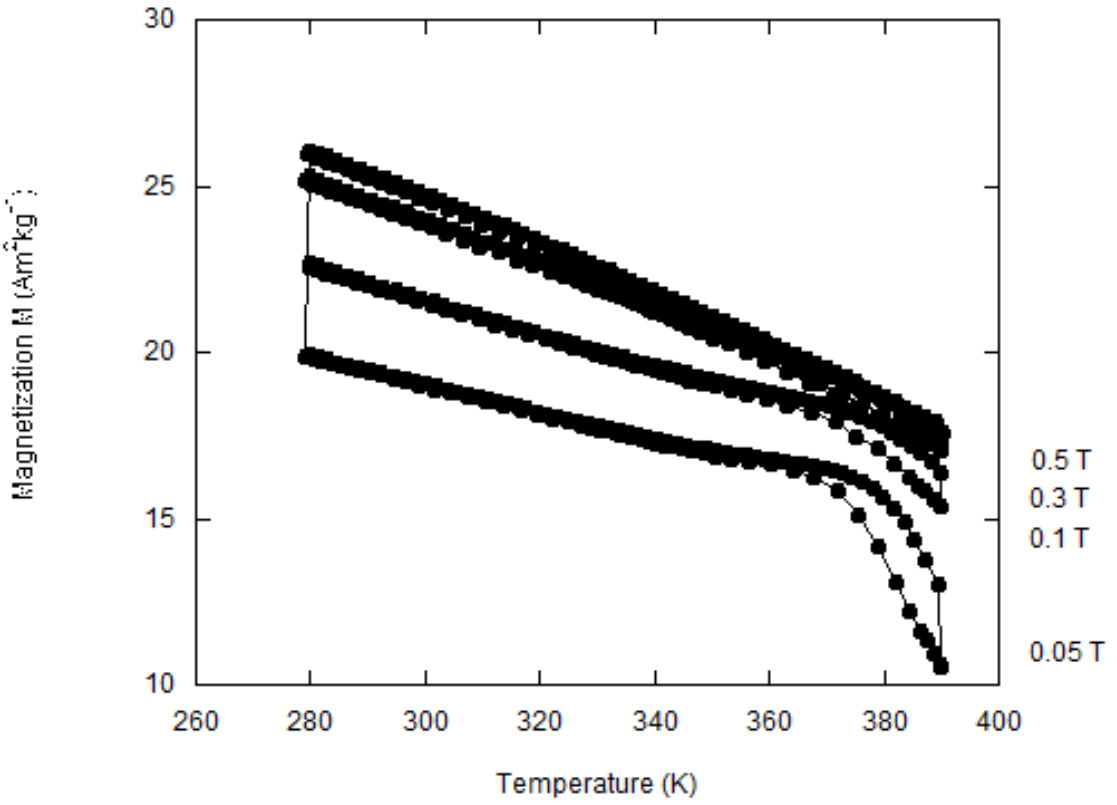

Fig. 3.3.1.1. Temperature dependence of the magnetization of $Mn_{1.85}Fe_{0.15}Sb_{0.9}Sn_{0.1}$ *in* $260 \leq T \leq 380$ *K for 0.05, 0.1, 0.3, and 0.5 T.*

Fig. 3.3.1.2. shows the temperature dependence of the magnetization of $Mn_{1.85}Fe_{0.15}Sb_{0.9}Sn_{0.1}$ in $10 \leq T \leq 380$ K for $\mu_0 H = 0.1$, and 1 T. As seen in Fig. 3.3.1.2, there is no magnetic phase interaction for $\mu_0 H = 0.1$ and 1T. Any other anomaly below 380 K was not detected. Fig. 3.3.1.2. shows

normal ferromagnetic behaviour. The magnetization of 1 T at 10 K was 38.7 Am_2/kg.

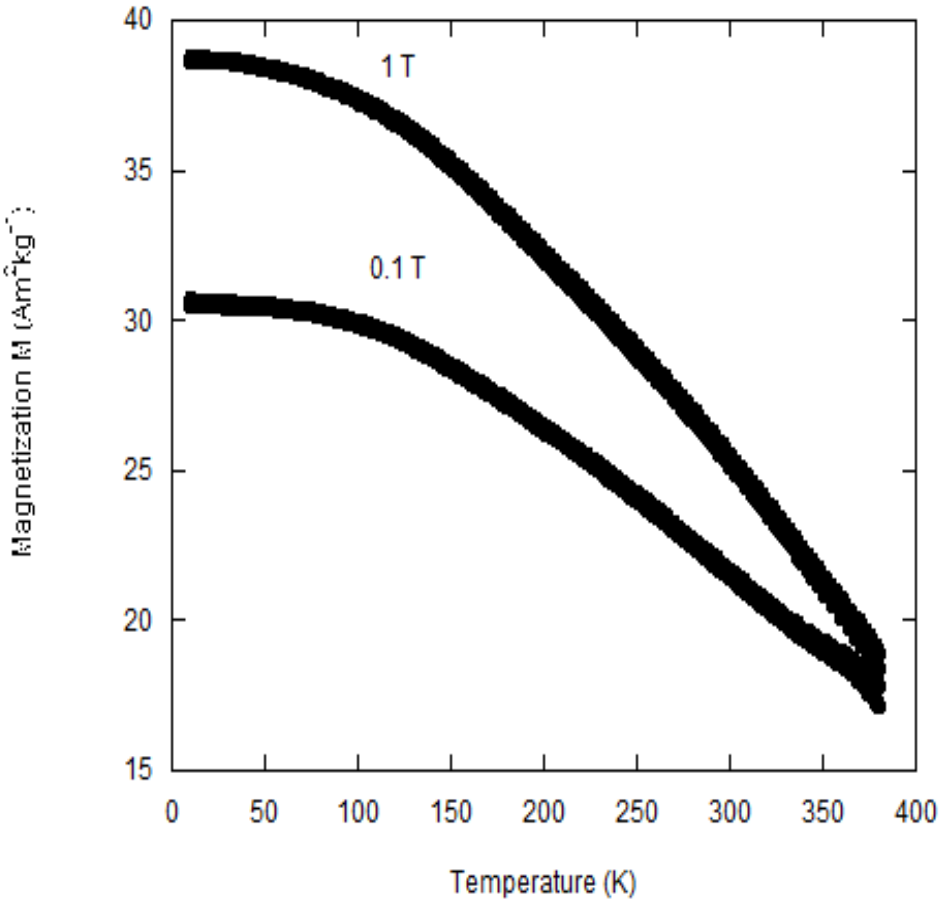

Fig. 3.3.1.2. Temperature dependence of the magnetization of $Mn_{1.85}Fe_{0.15}Sb_{0.9}Sn_{0.1}$ in $10 \leq T \leq 380$ K for 0.1, and 1 T.

Fig. 3.3.1.3 shows the magnetization curves of $Mn_{1.85}Fe_{0.15}Sb_{0.9}Sn_{0.1}$

for $\mu_0 H \leq 5$ T at 280, 300, 320, 340, 360 and 380 K. As shown in Fig. 3.3.1.3, the magnetization curves did not show magnetic hysteresis. With increasing T, the magnetization decreases. First order phase transition was not observed.

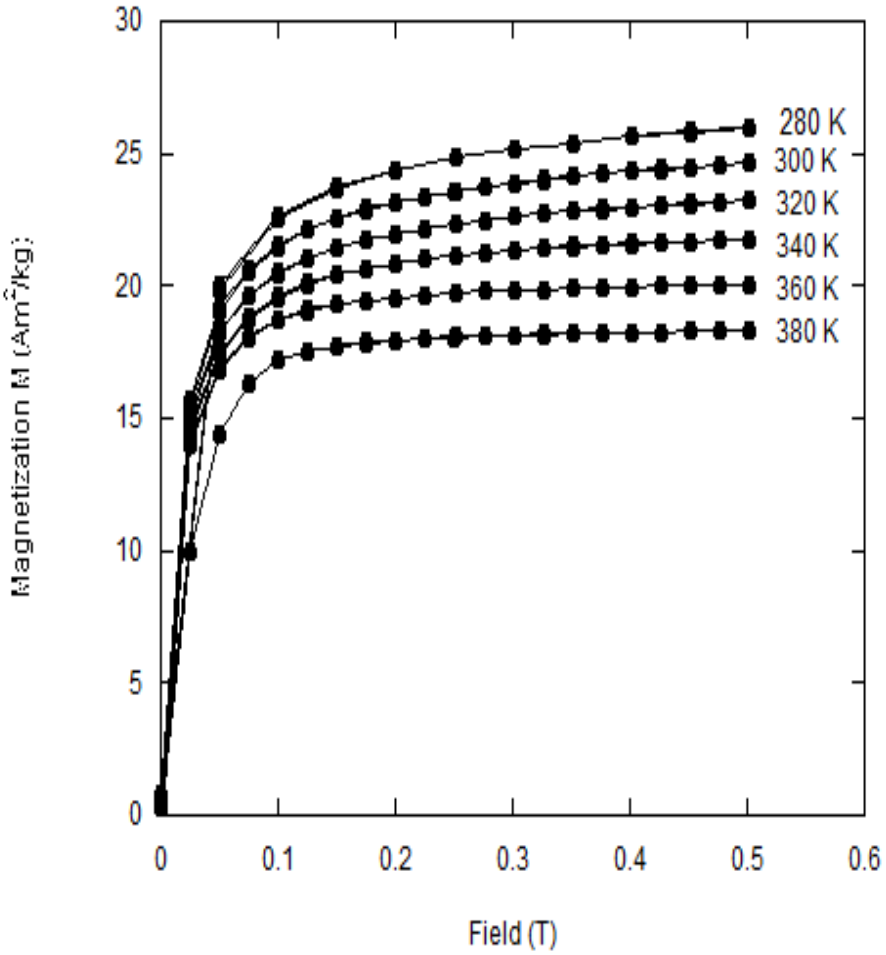

Fig. 3.3.1.3. Magnetization curves of $Mn_{1.85}Fe_{0.15}Sb_{0.9}Sn_{0.1}$ at 280, 300, 320, 340, 360 and 380 K for $\mu_0 H \leq 5$ T.

Chapter 4

Discussion

The *M-T* curves of $Mn_{1.9}Fe_{0.1}Sb_{0.9}Sn_{0.1}$ exhibited the FOMT between the FRI and PM-like IM states with the thermal hysteresis under low magnetic fields in the vicinity of T_t, as shown in Figs. 3.1.2.2 and 3.1.2.3. However, metamagnetic transition on the *M-H* curves or anomaly for the XRD results in the vicinity of T_t were not observed, as shown in Figs. 3.1.2.4 and 3.1.3.2. In order to clarify this inconsistency, the DSC measurement was performed for $Mn_{1.9}Fe_{0.1}Sb_{0.9}Sn_{0.1}$.

Figure 4.0.1 shows the DSC curves of $Mn_{1.9}Fe_{0.1}Sb_{0.9}Sn_{0.1}$. As indicated by the arrows in Fig. 4.0.1, the exothermic cusp and endothermic dip were observed at 509 K without the hysteresis, suggesting that the second-order phase transition occurred at this temperature. However, other peaks were not observed. The T_C (second order transition) of the ferromagnetic impurity phase of the MnSb alloys is reported to be 550-586 K [Caron, 2013, Chikazumi, 2009, Ilyn, 2015]. Our DSC experiment could not detect any signal in the temperature range of 550-586 K, indicating the

ineffectiveness of the impurity phase on properties of $Mn_{1.9}Fe_{0.1}Sb_{0.9}Sn_{0.1}$. The T_C of $Mn_2Sb_{0.9}Sn_{0.1}$ Koyama, 2013] and $Mn_{1.8}Fe_{0.2}Sb$ [Kanomata, 1984] were reported to be 530 K and 500 K. Considering these reports and the tendency of the M-T curve for $\mu_0 H$ = 5 T (Fig. 3(a)), it is supposed that the peaks of the DSC curves is due to the second order magnetic transition of $Mn_{1.9}Fe_{0.1}Sb_{0.9}Sn_{0.1}$. That is, T_C of $Mn_{1.9}Fe_{0.1}Sb_{0.9}Sn_{0.1}$ is 509 K, which exists between the T_C of $Mn_{1.8}Fe_{0.2}Sb$ and $Mn_2Sb_{0.9}Sn_{0.1}$.

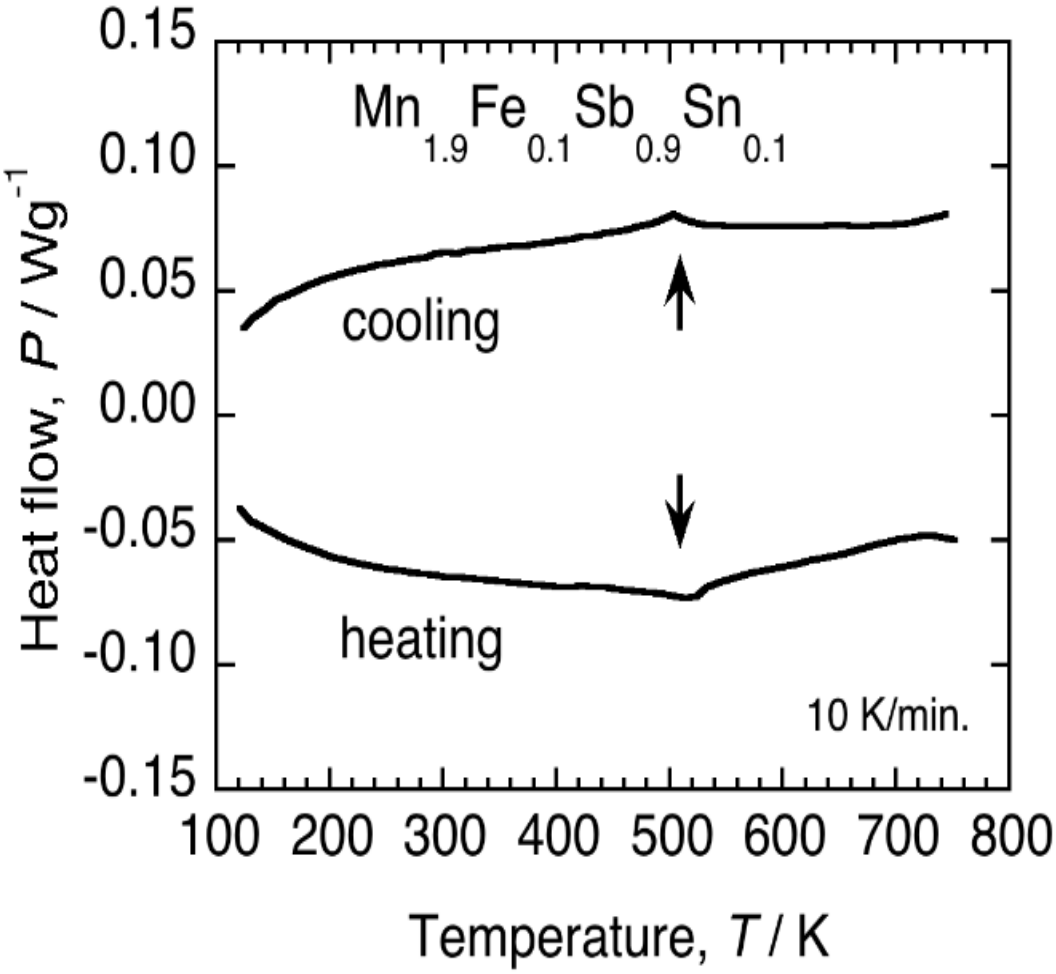

Fig. 4.0.1. DSC curves for $Mn_{1.9}Fe_{0.1}Sb_{0.9}Sn_{0.1}$. The vertical arrows indicate the defined temperature for phase transition [Nwodo et al., 2018].

In general, when the first-order transition occurs, the large exothermic and endothermic peaks with the hysteresis are observed, which is larger than those of the second-order magnetic transition, because of the latent heat. Therefore, it is supposed that the FOMT observed at T_t is not thermodynamic

phase transition. Mn_2Sb [Wilkinson, 1957, Beckman, 1991] and $Mn_2Sb_{0.9}Sn_{0.1}$ exhibits the SR in the FRI state. According to ^{57}Fe Mössbauer spectroscopy by Blaauw *et al*., $Mn_{1.98}Fe_{0.02}Sb$ also indicates the SR at T_{SR} ($80 < T_{SR} < 300$ K), and the transition of the moments from being parallel to the *c*-axis at $T > T_{SR}$ to being parallel to the *c*-plane at $T < T_{SR}$ occurs in the FRI state, which is consistent with that of Mn_2Sb [Bartashevich 2002, Val'kov, 2007].

In the SR phenomenon, not only the exchange interaction but also the magnetic anisotropy plays an important role [Ilyn and Zubkov, 2015]. The first-order and second-order transitions due to the SR have been reported [Ilyn and Zubkov, 2015, Andreev and Ilyn, 2017, Andreev et al., 2008]. Ilyan *et al*., and Andreev *et al*., reported that the SR from a cone-spin structure to an easy-axis spin structure (cone-axis type) was the second-order transition, and the SR from the easy-axis to an easy-plane spin structure (axis-plane type) also occurred as the first-order transition. Iyan *et al*. also pointed out that the magnetic field-induced SR changes the second-order transition [Ilyn and Zubkov, 2015]. That is, the SR occurs due to the competition between two different magnetic anisotropy energies, and the first-order SR changes

to the second-order SR by application of magnetic fields, because the magnetic field induces the cone-spin structure.

As mentioned above, the Mn_2Sb system shows the SR of the axis-plane type [Wilkinson 1957, Beckman, 1991, Blaauw, 1978, Caron, 2013]. Therefore, the SR observed in Mn_2Sb system is the first-order transition with the hysteresis, as seen in Figs. 3.1.2.2 and 3.1.2.3. The substitution of Fe for Mn in $Mn_2Sb_{0.9}Sn_{0.1}$ suppressed the AFM interaction and enhanced the FRI interaction in $Mn_{1.9}Sb_{0.9}Sn_{0.1,}$ resulting that AFM state almost disappeared and the SR temperature with the first-order transition increased to T_t in $Mn_{1.9}Fe_{0.1}Sb_{0.9}Sn_{0.1}$, as seen in Fig. 3.1.2.2. When the magnetic field was applied, the first-order SR changed the second-order SR, so that the thermal hysteresis on the *M*-*T* curves (Fig. 3.1.2.3) disappeared easily for $\mu_0 H \geq 1$ T, and the metamagnetic transition on the *M*-*H* curve (Fig. 3.1.2.4) was not observed in the vicinity of T_t. The *M*-*H* curves at $T \geq T_t$ became saturated for $\mu_0 H \geq 1$ T, which is consistent with the *M*-*T* data but different from the usual PM *M*-*H* curve over second-order magnetic transition temperature. This is probably due to the magnetic field-induced SR changes from the first- to second-order, as pointed out by Iyan *et al*.. 2015.

The magnetic entropy change in the vicinity of T_t expects to be very small, because the SR is one of the order-order transition. As seen in Fig. 3.1.3.2, $Mn_{1.9}Fe_{0.1}Sb_{0.9}Sn_{0.1}$ exhibited the normal thermal expansion for $10 \leq T \leq 325$ K, indicating that the first-order structural transformation did not occur at T_t. Therefore, it is supposed that the exothermic and endothermic peaks with the hysteresis on the DSC curves were not observed at T_t, as seen in Fig. 4.0.1. These results suggest that the elastic energy-change due to the observed FOMT is negligibly small at T_t.

The cusps on the *M*-*T* curves of $Mn_{1.9}Fe_{0.1}Sb_{0.9}Sn_{0.1}$ under $\mu_0 H = 5$ mT were observed just below the thermal hysteresis, which is the Hopkinson effect-like phenomenon [Ilyn, et al., 2015], as shown in Fig. 3.1.2.2. In general, the Hopkinson effect is caused by movement of magnetic domain wall [Ilyn and Zubkov, 2015]. The domain wall energy is related to the spontaneous magnetization (I_S) and the magnetic anisotropy constant (K) [Ilyn and Zubkov, 2015]. When the temperature is just below the critical point, K decreases rapidly compared to the decrease of I_S, so that the domain wall can displace easily [Ilyn and Zubkov, 2015]. This leads to the observation of the cusp on the *M*-*T* curve under low magnetic field just below

the critical temperature. The wall displaced irreversibly and does not return to its original position even after the magnetic field was removed [Ilyn and Zubkov, 2015]. In this work, the observed SR is probably related to the competition between two magnetic anisotropy energies (*c*-axis-type and *c*-plane-type), and the displacement of the magnetic domain wall. Therefore, the thermal hysteresis on the *M*-*T* curves of $Mn_{1.9}Fe_{0.1}Sb_{0.9}Sn_{0.1}$ was probably observed, as seen in Fig. 3.1.2.3. Though the magnetic and domain structures are not clear in the FRI and PM-like (IM) states in $Mn_{1.9}Fe_{0.1}Sb_{0.9}Sn_{0.1}$, it is supposed that FRI phase has the *c*-plane type anisotropy and the IM phase has the *c*-axis anisotropy in a zero-magnetic field. The magnetization for $T > T_t$ was very small (M = 3 Am^2/kg at 360 K) in for $\mu_0 H$ = 0.05 T, which may be due to the influence of the compensation of the domains. That is, the observed magnetic transition in the vicinity of T_t was not thermodynamic but quasi-FOMT, and the magnetic field induced a crossover-like SR-change from the first- to second-order.

As seen in Figs. 3.1.2.2 (a) and 3.1.2.4, the values of the magnetization for $\mu_0 H$ = 0.1 and 5 T at 10 K were slightly smaller than those around 100 K, indicating that a small fraction of the FRI phase changed to the AFM phase

in $Mn_{1.9}Fe_{0.1}Sb_{0.9}Sn_{0.1}$, and the partial AFM phase existed in the FRI phase at low temperature. When the magnetic field was applied, the gain of the Zeeman energy (magnetic energy) of the FRI phase is larger than that of the AFM phase, leading to the change of the part of the AFM phase to the field-induced FRI phase. Therefore, the hysteresis on the *M-H* curves for $10 \leq T \leq 160$ K was observed, as seen in Fig. 3.1.2.5. In this temperature range, the thermal hysteresis on the *M-T* data was also observed. At 250 K, the hysteresis on the *M-H* and *M-T* curves was not confirmed. These results suggest that the observed thermal hysteresis on the *M-T* curves was due to the first-order phase transition between the FRI and partial AFM phase.

In this study, we found the magnetic field-induced transition from the partial AFM to FRI phase at $T < 250$ K and the quasi-FOMT that showed field-induced crossover from the first- to second-order magnetic transition in $T > T_t$ for $Mn_{1.9}Fe_{0.1}Sb_{0.9}Sn_{0.1}$. In this paper, we do not report magnetic relaxation behaviors or the thermal transformation arrest (TTA) effect of $Mn_{1.9}Fe_{0.1}Sb_{0.9}Sn_{0.1}$. However, the two types of the field-induced state exist for different temperatures, so that there is a possibility that the interesting TTA effect is observed in $Mn_{2-x}Fe_xSb_{1-y}Sn_y$ ($0.05 \leq x \leq 0.15$, $0.05 \leq y \leq 0.1$)

Chapter 5

CONCLUSION AND SUGGESTION FOR FUTURE WORK

5.1 Conclusion

Magnetization and X-ray diffraction measurements were carried out for polycrystalline $Mn_{2-x}Fe_xSb_{1-y}Sn_y$ ($0.05 \leq x \leq 0.15$, $0.05 \leq y \leq 0.1$) in $10 \leq T \leq 360$ K and $0 \leq \mu_0 H \leq 5$ T. $Mn_{2-x}Fe_xSb_{1-y}Sn_y$ ($0.05 \leq x \leq 0.15$, $0.05 \leq y \leq 0.1$) had the Cu_2Sb-type tetragonal structure.

The temperature dependence of the lattice parameters and cell volume of $Mn_{1.9}Fe_{0.1}Sb_{0.9}Sn_{0.1}$ under a zero field and 5 T showed the normal thermal contraction without discontinuous change due to the structural transformation in $10 \leq T \leq 325$ K. The thermal expansion coefficients of a and c were estimated to be $\alpha(a) = 13 \times 10^{-6}$ K^{-1} and $\alpha(c) = 13 \times 10^{-6}$ K^{-1} in $275 \leq T \leq 325$ K, respectively. The compound showed the quasi-FOMT from the FRI to PM-like state with the thermal hysteresis at T_t = 310 K. By applying magnetic fields over 1 T, the FOMT almost disappeared. The saturation magnetization of $Mn_{1.9}Fe_{0.1}Sb_{0.9}Sn_{0.1}$ at 10 K was determined to be

39.1 Am^2/kg (39.1 emu/g), which was slightly smaller than the value (39.2 Am^2/kg) at 70 K for $Mn_{1.9}Fe_{0.1}Sb_{0.9}Sn_{0.1}$. The compound also showed the thermal hysteresis in $70 \leq T \leq 230$ K for 0.1 T and 5 T, which is due to the phase transition between the FRI and partial AFM. The magnetic hysteresis of the magnetization curves in $10 \leq T \leq 160$ K was clearly observed, which originates from the magnetic field-induced phase transition from the partial AFM to FRI.

$Mn_{1.95}Fe_{0.05}Sb_{0.95}Sn_{0.05}$ did not show the AFM-FRI first ordered transition but the first-order phase transition from a FRI to an PM-like phase occurs in the vicinity of 320 K (= T_t) with a thermal hysteresis of approximately 5 K. By applying magnetic fields over 1 T, the FOMT almost disappeared. The saturation magnetization of $Mn_{1.95}Fe_{0.05}Sb_{0.95}Sn_{0.05}$ at 10 K was determined to be 40.2 Am^2/kg.

$Mn_{1.85}Fe_{0.15}Sb_{0.9}Sn_{0.1}$ exhibits a first order phase transition from a FRI to a PM-like state with a hysteresis of about 15 K in the vicinity of 380 K (= T_t) for $\mu_0 H = 0.05$ T. By applying magnetic fields over 1 T, the FOMT around T_t almost disappeared. Any other anomaly such as FOMT below 380 K was not detected. The magnetization of 1 T at 10 K was 38.7 Am_2/kg. With

increasing Fe contents, the magnetic moment of 10 K decreases but the first order magnetic transition temperature T_t increase.

In this study, the FRI-PM (PM-like) FOMT (quasi-FOMT) was observed in the Mn_2Sb system for the first time. The obtained results show that the quasi-FOMT can be easily controlled by magnetic fields below 0.5 T.

5.2 Suggestion for Future Work

The following future work is suggested to build and expand upon the results of this thesis in order to obtain better understanding of the magnetic, structural, thermal and properties of $Mn_{2-x}Fe_xSb_{1-y}Sn_y$ (x = 0.1, 0.05 and 0.15) and its suitability for magnetic field controlled materials

1. Test additional materials with promising magnetic, structural, thermal properties and magnetocaloric effect (MCE) performance using the MFCM, such as Mn_2Sb type, and others.

2. Further theoretical analysis for the phenomena observed in this study, including the difference between the cooling and heating modes. In either case, magnetocaloric performance of every material should be correlated with the phase diagram of the corresponding system in temperature-magnetic field coordinates.

3. Test a real active Mn_2Sb with magnetic field controlled materials **(MFCM)** measured in this study, to confirm their performance for a wide range of operating parameters including magnetic field sweeping speed. This work is in progress.

4. Explore optimized AMR cycle design to make full use of the characteristics of the first order materials studied in this project, with the goal to increase the unit cooling capacity and energy efficiency. For example, explore ways to make use of the MCE difference between cooling and heating process.

REFERENCES

Aharoni **A**, **1969**, Physical review, APS, 177, 177-796

Andreev A V and Ilyn M I, **2017**, J. Magn. Magn. Mater. **310** 1735-1737

Andreev A V, Tereshina E A, Santava E, Koyama K, Homma Y, Satoh I, Yamamura T, Shiokawa Y. and Watanabe K, **2008**, J. Alloy Comp. **450** 51-57

Baranov N V, Khrulev Y A and Bartashevich M I, **1994**, J. Alloy and compound **210** 197

Bartashevich M I, Goto T, Tomita T, Baranov N V, Zemlyanski SV, Hilscher G and Michor H, **2002**, Physica B **318** 198

Beckman O and Lundgren L, **1991**, in "Handbook of Magnetic Materials", Vol. 6, ed. K H J. Buschow (Elsevier, Amsterdam) p. 181

Berry M V and Geim A K, **1997**, Eur. J. Phys. **18** 307

Bither T A, Walter P H L, Cloud W H, Swoboda T J, Bierstedt P E, **1962**, J. Appl. Phys. Suppl. **33** 1346

Bither T A, Walter P H, Cloud W H and Swoboda T J, **1962b**, J. Appl. Phys. **33** 1346S

Blaauw C, Mackay G R and Leipe W, **1978**, J. Magn. Magn. Mater. **8**, 240

Blaauw C, Mackay G R and Leipe W, **1977**, Physica **86-88B** 885

Bozorth R M, Ferromagnetism, first published 1951, reprinted 1993 by IEEE Press, New York as a "Classic Reissue." ISBN 0-7803-1032-2.

Brandt E H, 1980, Am J. Physics **58** 43-9.

Buschow K H J, *Ferromagnetic Materials*, **1988**, vol. 4, ed. E.P. Wohlfarth and K H J Bushow (Amsterdan: North-Holland), p.1

Caron L, Mial X F, Klaasse J C P, Gama S and Brück E, **2013**, Appl. Phys. Lett. **103** 112404

Chikazumi S, 1997 & 2009, *Physics of ferromagnetism,* English edition, ed. C.D. Graham, Jr (2nd ed.). Oxford: Oxford University Press. p. 118 - 145

Cloud W H, Bither T A, Swoboda T J, 1961, J. Appl. Phys. **32**, 55S.

Clould W H, Jarret H S, Austin A E, and Adelson E, 1960, Phys. Rev. **120** 1969

Croat J J, Herbst J F, Lee W E and Pinkerton F E, **1984**, J. Appl. Phys. **55** 2078.

Darnell F J, Cloud W H and Jarret H S, **1963**, Phys. Rev. **130** 647

Differential scanning calorimetry (NETZSCH DSC 200 F3 Maia) NETZSCH catalog 1108, **2000**, Available via https://www.netzsch.com/en/

Ed. National Astronomical Observatory: Rikainenpyo **1990**, Maruzen Co. Ltd. Pp. 539 in Japanese.

Enz U, **1982**, in "Feromagnetic Materials", Vol.3, ed. E P Wohlfarth (North-Holland, Amsterdam) p.1

Fagaly R L, **2006**, Review of Scientific Instruments **77** 101101

Foner S, **1959**, Rev. Sci. Inst. **30** 548

Guillaud C, Bertrand R and Vautier R, **1949**, C. R. acad. Sci. **228** 1403

Hatch, G P, Stelter, R E, 2001, Journal of Magnetism and Magnetic materials, **225** 262-276

Horowitz A L, **1989**, *MRI Physics for Physicians*, Springer Science & Business Media

Ilyn, M, Zubkov, I N, **2015**, Proc. 3rd Moscow Int. Symposium on Magnetism 232-235.

Jackson M, **2000**,*"Wherefore Gadolinium? Magnetism of the Rare Earths"* (PDF). IRM Quarterly. Institute for Rock Magnetism. **10** (3): 6.

Jackson R, **2015**, *John Tyndall and the Early History of Diamagnetism*, Annals of Science, **72(4)** 435-489

Jensen J & MacKintosh, A R, **1991**, *Rare Earth Magnetism,* Oxford: Clarendon Press.

Kanomata K and Ido H, **1984**, J. Appl. Phys. **55** 2039

Kanomata T, Hasebe Y, Ito T, Yoshida H and Kaneko T, **1991**, J. Appl. Phys. **69** 4642

Katter M, Wecker J and Schultz L, **1991**, J. Appl. Phys. **70** 3188

Kirenskii L V, 1967, Magnetizm, 2nd ed. Moscow, p.67

Kittle C, **1986 &1996**, *Introduction to Solid State Physics* (6th ed.). John Wiley & Sons. *299–302*

Kleiner K, **2007**, *Magnetic gravity trick grows perfect crystals*. New Scientist, Retrieved September 2011. *Available via*

https://www.newscientist.com/article/dn12467-magnetic-gravity-trick-grows-perfect-crystals/

Koyama K, 1997, Ph.D thesis, Hiroshima University

Koyama K, Ishikawa1 F and Watanabe K, 2006, Intl. J. Applied Electromagnetics and Mechanics **23**, 153–163.

Koyama K, Mitsui Y and Watanabe K, **2008**, IOP publishing Science and Technology of Advanced materials Sci. Technol. Adv. Mater. **9** 024204

Koyama K, Shimada D, Adachi Y, Orihashi H, Mitsunaga D, Hiroi M, Mitsui Y, Kimura S, Matsubayashi K and Uwatoko Y, **2015**, Rep. Fac. Sci. Kagoshima Univ. **48** 15

Koyama K, Shimada D, Orihashi H, Mitsunaga D, Hiroi M, Matsubayashi K, Uwatoko Y, Onodera R, Kimura S and Takahashi K, **2013**, Rep. Fac. Sci. Kagoshima Univ. **46** 37

Kushwaha P, Rawat R, Chaddah P, **2008**, J. Phys. Condens Matter **20**, 022204

Landau L D, 1930, ZeitschriftfürPhysik A Hadrons and Nuclei 64.9 629

Livingston J D, **1987**, in *Physics of Magnetic Materials*, ed M Takahashi, S Maekawa, Y Gondo and H Nose (Singapore: Word Scientific), p.3

Livingston J D. 1990, J. Mat., **42** 30-34

Magnetic properties measurement system, MPMS, 2004, multiVu user's manual, Quantum Design, part no 1014-110C

Matsumoto Y, Matsubayashi K, Uwatoko Y, Hiroi M, Mitsui Y and Koyama K, **2016**, AIP Conf. Proc. **1763** 020005

Matsumoto Y, Orihashi H, Matsubayashi K, Uwatoko Y, Hiroi M and Koyama K, **2014**, IEEE Trans. Mag. **50** 1000704

Miessler G L and Tarr D A, 2010, *Inorganic Chemistry* 3rd ed., Pearson/Prentice Hall publisher, Available via https://en.wikipedia.org/wiki/International_Standard_Book_Number

Miller L L, **1996**, Rev. Sci. Instrum. **67**, 3201

Myers W R, **1952**, Rev. Mod. Phys. **24** 15

Nakamura Y and Tahra R, **1976**, J. Phys. Soc. Japan **41** 459

Nave C L, *Magnetic Properties of solid. HyperPhysics. Retrieved* ***2008-11-09.*** Available via http://hyperphysics.phy-astr.gsu.edu/hbase/Tables/magprop.html

Néel L, **1948**, Ann. de physiq. **3** 137

Nwodo A N, Kobayashi R, Wakamori T, Matsumoto Y, Mitsui Y, Umetsu R Y, Hiroi M, Takahashi K, Uwatoko Y, Koyama K, **2018,** IEEE Magn. Lett. 9, 1400204

Ohashi M, Yamaguchi Y and Kanomata T, 1992, J. Magn and Magn. Mater. **104** 925

Orihashi H, Hiroi M, Mitsui Y, Takahashi K, Watanabe K, Matsubayashi K, Uwatoko Y and Koyama K, **2013**, Mater. Trans. **54** 969

Pallavi K, Rawat R, and Chaddah P, **2008**, J. Phys: Condens Matter 20, 022204 (7pp)

Pauling L, **1936**, J. Chem. Phys. **4** 673

Quantum Design MPMS Application Note 1014-202, **2000**, Transverse detection system .available via http://www.qdusa.com

Sagawa M, Fujimura S, Togawa N, Yamamoto H and Matsuura Y, **1984**, J. Appl. Phys. **55** 2083

Sessoli R, Tsai H L, Schake A R, Wang S, Vincent J B, Folting K, Gatteschi D, Christou G, Hendrickson D N, **1993**, J. Am. Chem. Soc. **115** 1804

Shimada D, Orihashi H, Mitsunaga D, Ito M, Hiroi M, Koyama K, Onodera R, Takahashi K, Matsubayashi K, Uwatoko Y, **2013**, J. Korean Physical Society **63** 747

Shirakawa K and Ido H, **1976**, J. Phys. Soc. Jpn. **40** 666

Sirota N N and Ryzhkovskii V M, **1975**, Sov. Phys.-Solid State **16** 1714

Sozinov A, Likhachev A A and Lanska N, **2002**, Applied Phys. Lett. **80** 1746.

Stanciu C D, Kimel A V, Hansteen F, Tsukamoto A, Itoh A, Kirilyuk A and Rasing T, 2006, Phys. Rev. B 73 220402

Strnat K H, Hoffer G J, Ostertag W and Olson I C, 1966, J. Appl. Phys. **37** 1252

Tsujimura A, Hihara T and Koi Y, **1962**, J. Phys. Soc. Jpn. **17** 1078

Ullakko K, Huang J K and Kantner C, **1996**, Applied Phys. Lett. **69** 1966

Val'kov V I, Golovchan A V, Bribanov I F, Kamenev V I, Iesenchuk O O, Sivachenko A P and Kabdin N N, **2007**, Low Temp. Phys. **33** 70

Wakamori T, Mitsui Y, Takahashi K, Umetsu R Y, Hiroi M and Koyama K, **2016**, AIP Conf. Proc. **1763** 020006

Wakamori T, Mitsui Y, Takahashi K, Umetsu R Y,Uwatoko Y, Hiroi M and Koyama K, **2017**, IEEE Magn. Lett. **8** 1402404

Watanabe K, Watanabe Y, Awaji S, Fujiwara M, Kobayashi N and Hasebe T, **1998**, Adv. Cryg. Engin. **44** 747

Wilkinson M K, Gingrich N S, Shull C G, **1957**, J. Phys. Chem. Solids **2** 289

Jansen Y, 2003, Interplay between anisotropy and exchange interactions in rare earth-transition-metal ferrimagnets, Ph.D Thesis, Univ. Amsterdem, p.26-27

Zhong X P, Radwanski R J, de Boer F, Jacobs T H and Buschow K H J, **1990**, J. Magn. Magn. Mater. **86** 333

Izumi F, *Retveld analysis programs RIETAN and PREMOS and special applications*, in: The Rietveld Method, Young R A, ed., Oxford University, 1995, pp. 236-253

LIST OF PUBlCATIONS

1. **A.N. Nwodo**, R. Kobayashi, T. Wakamori, Y. Matsumoto, Y. Mitsui, R.Y. Umetsu, M. Hiroi, K. Takahashi, Y. Uwatoko, K. Koyama, Magnetic Phase Transition of $Mn_{1.9}Fe_{0.1}Sb_{0.9}Sn_{0.1}$, IEEE Magn. Lett. 9 (2018) 1400204.
2. **Adline N. Nwodo,** Ryota Kobayashi, Taoto Wakamori, Yoshihiro Matsumoto,

   Yoshifuru Mitsui, Masahiko Hiroi, Kohki Takahashi, Rie Y. Umetsu, Yoshiya Uwatoko, and Keiichi Koyama, Quasi-First Order Magnetic Transition in $Mn_{1.9}Fe_{0.1}Sb_{0.9}Sn_{0.1}$, Materials Transaction 59 (2018) in press.